A billiard model for wet granular matter

Franziska Glaßmeier

A billiard model for wet granular matter

Diplomarbeit

vorgelegt von

Franziska Glaßmeier

aus

Münster

angefertigt am
Max-Planck-Institut für Dynamik und Selbstorganisation
und der Georg-August-Universität Göttingen

September 2010

Referentin: Prof. Dr. Annette Zippelius
Korreferent: apl. Prof. Dr. Jürgen Vollmer

Acknowledgements

This diploma thesis was written at the Max-Planck-Institute for Dynamics and Self-Organization and at the Georg-August University, Göttingen. I would like to thank Prof. Jürgen Vollmer for his dedicated supervision, his steady enthusiasm and for many valuable discussions and Prof. Annette Zippelius for her commitment as a referee. I furthermore want to acknowledge my colleagues for the pleasant and scientifically lively atmosphere at the Department of Complex Fluids.

Contents

Chapter 1

Introduction

Granular matter consists of macroscopic particles that occur in many outside-the-lab situations, ranging from breakfast cereals [US07, SUK+06] and industrial grain processing over quick sand [LRBvdM04] and sand castles as well as landslides [Her05] up to hail stones and interstellar dust clouds [PB04, Sec. 1.7.1]. The interaction between granular particles is governed by dissipative contact forces so that the dynamics of granular materials is out of equilibrium. If no energy is injected, e.g. by tapping or shearing, the system is studied in free cooling (e.g. [UAR+09]), otherwise steady states (e.g. [RVH09]) where dissipation and energy input balance might occur. A common type of dissipative interaction are inelastic collisions [PB04]. There are, however, many granular phenomena like sandcastles and the accretion of interstellar dust resulting in the formation of stars that require an attractive interaction.

This thesis will be concerned with a type of interaction that naturally combines attraction and dissipation by means of a hysteretic, i.e. history-dependent, pseudo-potential. This thesis is concerned with a simple schematic version of such an interaction namely the thin-thread model [FRHH08] described in Fig. 1.1 (left). Due to absence of the attractive potential no energy is gained in approaching. Upon removal, however, energy is dissipated to overcome the potential emerging after contact. If the kinetic energy is too low to overcome the potential, particles will cluster together. The typical example for this kind of interaction is given by wetted granular particles [WAJS00, Her05]: Here, two particles are only connected by a liquid bridge as shown in Fig. 1.1 (right) after a collision. Another example emerges due to contact deformation in interstellar dust [CTH93, DT97].

As a non-equilibrium system any approach to (wet) granular matter from statistical mechanics, especially kinetic theory and hydrodynamics, requires strong chaoticity properties of the underlying dynamics. These properties become manifest in the phase space distribution, which can conveniently be obtained numerically. The subject of this thesis is a detailed study of the phase space structure resulting from the hysteretic interaction and its dissipation. Due to its low dimensionality a Sinai billiard (or, equivalently, a quadratic Lorentz gas; [Szá00]) with accordingly modified collision rules is chosen as an exemplary system. As a consequence of dissipation the free motion in the modified Sinai billiard only persists until the system eventually ends up in the clustered state, i.e. the dynamics is transiently chaotic (e.g. [TG06, Chapter 6]). Before discussing the wet interaction and the Sinai billiard in detail, we give a outline of this thesis including a brief preview of the results.

In Chapter 2, the effects of dissipation leading to a steady energy reduction ("free cooling") on phase space structure and clustering are investigated. In this situation the phase space can be reduced to a space with two spatial dimensions, which allows easy visualization: A Poincaré section placed at the billiard boundary features the number of collisions as time variable. Consequently, the dissipation occurring after each collision is well-defined and the energy variable becomes trivial. As the wet billiard combines features of Hamiltonian and dissipative systems it is not immediately clear in what sense a compression of phase space volume will occur and how this might result in a structured, i.e. non-uniform, phase space distribution. It turns out that the hysteretic feature of the interaction may cause non-injectivity of the billiard map. The resulting double-folding of phase space eventually gives rise to a fractal distribution that is supported on the entire phase space. In a sense the wet billiard thus keeps the Hamiltonian feature of local volume conservation while dissipation nevertheless manifests itself in generating a fractal structure. In spite of the structure the phase space distribution is still well approximated by a uniform distribution. As a demonstrative application the clustering frequency is calculated.

In Chapter 3, the dissipation caused by the liquid bridges is augmented by an energy input to the billiard system. Shearing is chosen as an interesting driving mechanism for various reasons: Shearing is a situation very common in nature (earthquakes, landslides, accretion disks of stars) and in industrial applications (material transport through pipes due to gravity or air flow). Furthermore, shearing can be realized experimentally as well as in computer simulations and allows for homogenous densities. In the latter case so-called Lees-Edwards boundary conditions [AT87] are a conceptually simple tool. Even so, steady-states resulting from the application of Lees-Edwards boundary condi-

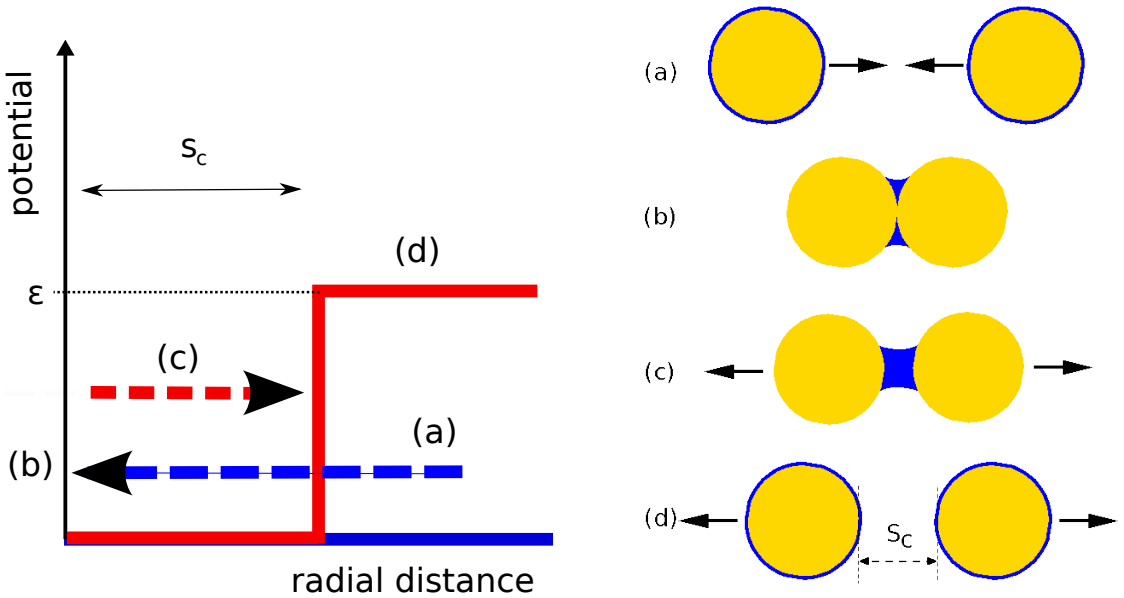

Figure 1.1: **Thin-thread model** [FRHH08]**:** The particles move freely (a) until they collide and form a liquid bridge (b). The bridge is modeled as the emerging of a potential well with velocity-independent depth ϵ (c). When leaving this potential well upon rupture of the liquid bridge (d) the particle's kinetic energy is reduced by the constant energy ϵ (right image courtesy by S. H. Ebrahimnazhad Rahbari).

tions to wet granular matter have not thoroughly been studied so far (for preliminary, unexpected results see [Bri09], [Rah09]). Also, to the author's knowledge, (dissipative) billiards with Lees-Edwards boundary conditions have not been discussed in this context. Instead, steady-states are commonly ensured by sophisticated variants of Lees-Edwards boundary conditions that have different properties [PIM94]. Finally, shearing seems especially interesting in the context of this work as it does not prevent clustering and is even connected to phenomena like spontaneous plugging, e.g. of industrial grains in hoppers.

The interplay of energy input and dissipation in the wet sheared billiard is found not to result in stables steady-states. Instead, continuous heating of the system even for low shear speeds is observed. As a result, the kinetic energy or the speed, respectively, becomes the essential phase space coordinate. The speed dynamics are shown to resemble a generalized random walk so that the speed distribution is broadened by diffusion. This leads to a linear growth of the mean-square speed displacement, which corresponds to the average kinetic energy. Eventually, this diffusive increase of the average energy dominates over the liquid bridge dissipation.

The sheared billiard is a billiard system with moving boundaries. In such systems the phenomenon of increasing average energy is known as Fermi acceleration after an idea of Enrico Fermi to explain the acceleration of charged particles that collide with chaotically moving magnetic clouds (e.g. [Los07]).

Due to the speed distribution broadening by diffusion the clustering region remains accessible in spite of the increasing average energies. The sheared wet billiard thus combines two effects of considerable interest in dynamical systems research: It is a transiently chaotic dissipative system that also exhibits Fermi acceleration. A remarkable feature resulting from this combination is that the sheared wet billiard possesses a power-law lifetime distribution instead of an exponential one. This feature is caused by the unboundedness of phase space that follows from Fermi acceleration and leads to an effectively shrinking clustering region.

Chapter 4 concludes with a summary of the results and points out some perspectives for future research.

1.1 Wet granular matter

1.1.1 Granular matter and types of interaction

Granular matter is characterized by two features: Particles are macroscopic and collisions dissipate kinetic energy into internal degrees of freedom of the particles. While the size of granular particles on the one hand excludes all kinds of microscopic effects including Brownian motion it gives rise to new questions like the effects of shape[1] and size distributions (e.g. [UKAZ09]). From a dynamical viewpoint, however, the dissipative nature of the interaction is crucial as it makes granular matter a system far from equilibrium.

So far, research in granular matter has mainly focused on repulsive interparticle interactions with viscoelastic dissipation. In the simplest approximation the latter is characterized by a *normal coefficient of restitution* ([PB04, Sec. 2.2])

$$\sqrt{\alpha} := \frac{v_\mathrm{n}^\mathrm{f}}{v_\mathrm{n}^\mathrm{i}},$$

given by the fraction of the pre-collision normal velocity v_n^i remaining as post-collision speed v_n^f. The energy dissipated thus decreases with the relative normal kinetic energy $E_\mathrm{n} = v_\mathrm{n}^2/2$ of the colliding particles:

$$E^\mathrm{f} - E^\mathrm{i} = -\left(1-\alpha\right) E_\mathrm{n}^\mathrm{i}. \tag{1.1}$$

Here, superscripts i and f denote the energy before and after the collision, respectively. Note that the dissipation therefore does not introduce a specific energy scale. For realistic modeling velocity-dependent coefficient of restitution are necessary [PB04], which in general does not affect the speed-dependence of the dissipated energy.

The study of inelastically colliding granulates has reached some textbook level (e.g. [PB04]) and many interesting results have been found. We mention correlations of the particle velocities caused by the inelasticity of the collisions [PBS03]. These correlations are an example of an effect that has macroscopically observable consequences but can largely be understood on the level of two-particle collisions. It thus stresses that it is worthwhile to study the interaction of individual pairs of granular particles in detail.

Many phenomena emerging in granular matter, such as sandcastles [Her05] and star formation out of interstellar dust [CTH93, DT97], however, require an attractive interaction. Starting from an attractive potential, interaction naturally becomes dissipative if it is *hysteretic*, i.e. not symmetric or direction-dependent, such that the potential energy gained in approaching of particles does not make up for the energy needed to escape (see Fig. 1.1 for an example). When the emerging *pseudo-potential* is independent of the impact speed also the dissipated energy is speed-independent so that it introduces an energy scale. Relative to this scale there are "slow" particles that will not have enough kinetic energy to overcome the potential barrier so that two collision partners stick together. In the limit of an infinitely deep pseudo-potential, the interaction is thus a "sticky" one, which never allows escape [CPY90].

This thesis is a detailed study of a hysteretic interaction with velocity-independent dissipation. The example of such an interaction that triggered this thesis is wet sand as

[1] There is, for example, ongoing research on packings of tetrahedra by Max Neudecker and Matthias Schröter, Max-Planck-Institute for Dynamics and Self-Organization, Dept. of Complex Fluids.

opposed to dry sand, which lacks attractive interaction. The terms *wet* and *dry* will therefore be used to refer to granulates with hysteretic interaction or granulates characterized by a constant coefficient of normal restitution, respectively.

1.1.2 Liquid bridges and contact deformation

Capillary bridge between two wetted spheres. To illustrate the basic physics involved in wetted granulates (Fig. 1.2, left) we follow [Her05] and refer to [WAJS00] for details. When bringing two wetted spheres, each of radius R, into contact, the covering liquid films will merge and form a *liquid bridge* as depicted in Fig. 1.3. The surface tension of the liquid γ and the two principal radii of curvature r_{i} (see Fig. 1.3) determine the Laplace pressure p_L in the contact region,

$$p_L = \gamma \left(\frac{1}{r_1} + \frac{1}{r_2} \right) \approx \frac{\gamma}{r_1},$$

where $r_1 \ll r_2$ is an assumption justified for small liquid contents resulting in non-overlapping bridges. The strong negative (inward) curvature corresponding to r_1 thus results in an underpressure that causes a liquid flow into the contact region until the contact angle reaches its equilibrium value θ. We restrict the present discussion to the case of complete wetting, i. e. $\theta = 0$, so that the liquid bridge connects tangentially to the spheres as in Fig. 1.3. In this geometry (and still assuming $r_1 \ll r_2$, or alternatively $r_2 \ll R$) one finds $r_2^2 = 2Rr_1$. The *capillary force* acting between the two spheres at the contact area $A = \pi r_2^2$ is then given by

$$F_0 = p_L A = 2\pi R\gamma.$$

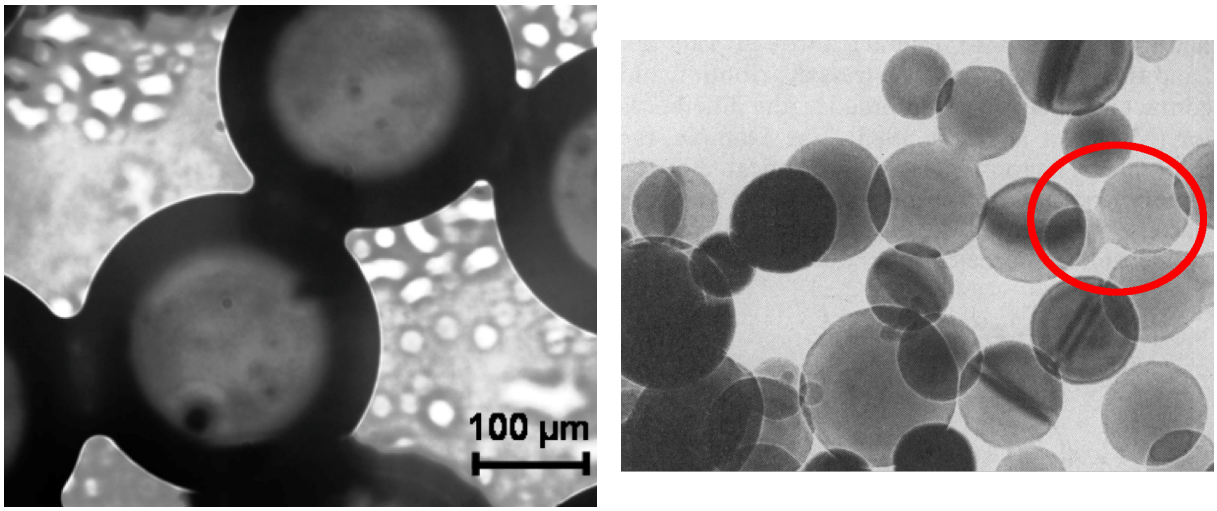

Figure 1.2: **Two examples for interactions that are dissipative due to hysteresis:** The optical micrograph on the left shows water bridges that have formed between wetted glass beads. The electron micrograph on the right shows material necks (best visible within the red circle) forming between colliding silicon grains (average grain diameter $\approx 70\,\mathrm{nm}$). The necks form as a consequence of increased van-der-Waals forces caused by contact deformation. This effect is negligible for the glass beads because of larger grain sizes. (left courtesy by Mario Scheel [Sch09], right image after [Iij87] in [CTH93]).

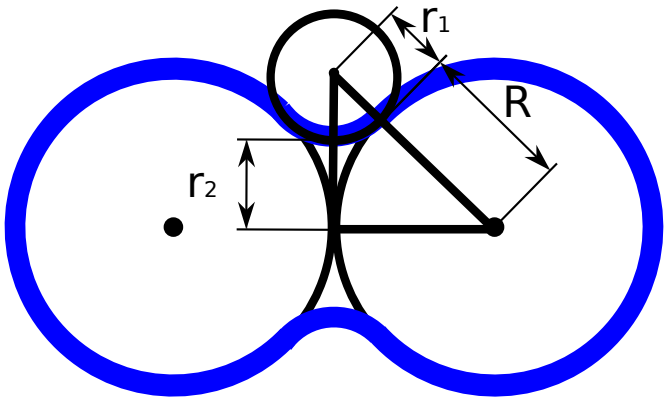

Figure 1.3: **Cross section of two wetted spheres connected by a liquid bridge** for a contact angle $\theta = 0$. Note that R_2 denotes the radius of the liquid-bridge section perpendicular to the plane shown. Also R_1 is depicted larger than realistic (cf. Fig. 1.2).

On separation, the liquid bridge connecting both spheres elongates. The change of the bridge force as a function of distance s can be approximated as [WAJS00]

$$F(s) = \frac{F_0}{1 + 1.05\sqrt{\frac{R}{V}}s + 2.5\left(\sqrt{\frac{R}{V}}s\right)^2}, \tag{1.2}$$

where the liquid bridge volume V appears as scaling factor. At a critical distance s_c, the liquid bridge ruptures. In [WAJS00] the authors find this *bridge-rupture distance* for $\theta = 0$ to be described by

$$s_c = V^{\frac{1}{3}} + 0.1 \cdot V^{\frac{2}{3}}. \tag{1.3}$$

At this point, the direction-dependent, hysteretic feature of the liquid bridge interaction is apparent: The bridge force is only present after the two spheres have touched not while they are approaching. Due to the missing force before the collision the total energy ϵ needed to elongate and rupture the liquid bridge is lost as kinetic energy. The dissipated *bridge-rupture energy* is given by [HF07, Sec. 3.2]:

$$\epsilon = \int_0^{s_c} F(s)\, \mathrm{d}s \approx \frac{2\pi\gamma}{R}\sqrt{V}. \tag{1.4}$$

As neither F_B nor s_c depend on the velocity of the spheres, ϵ is velocity-independent, too. This has important consequences: If the relative velocity of the collision partners is too small to rupture the liquid bridge they will stick together and form a cluster (Fig. 1.2, left). For dry granular matter, in contrast, the dissipated energy decreases via α with the relative kinetic energy of the colliding particles (Eq. 1.1). Thus, the formation of aggregates is not caused by pairwise sticking of particles but by decreasing granular pressure in strongly cooling regions (see e.g. [PB04, Part V]).

The coefficient of restitution corresponding to the dissipation by bridge rupture reads

$$\alpha_{\mathrm{wet}} = \sqrt{1 - \frac{\epsilon}{E_{\mathrm{i}}}} \tag{1.5}$$

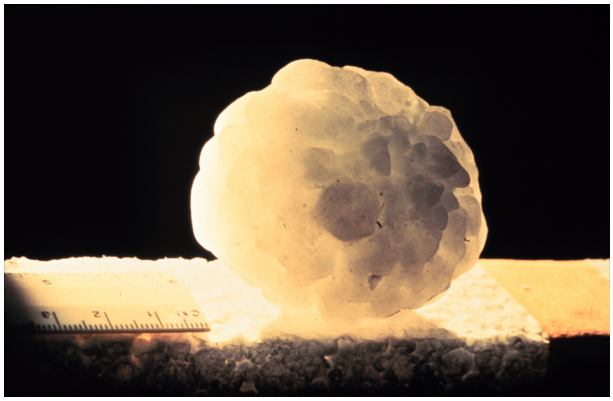

Figure 1.4: **Aggregated giant hail stone.** This giant hail stone [OA05] seems to be an aggregate of several smaller ones. As hail stones may be covered with a liquid layer in the so called "wet growth regime" liquid bridge interaction might, among other interactions, offer an explanation for the formation.

and decreases with E_i as required to obtain a constant dissipation.

It should be noted that in collisions between real wetted particles both dissipative effects, inelasticity and bridge rupture, are present. At low speeds the liquid-bridge interaction dominates while at high speeds inelasticity cannot be neglected anymore (cf. [Röl10, Sec. 3.3]). This thesis studies the wet-type interaction in detail and will compare it to the dry interaction. The mixed case lies outside its scope.

The liquid bridge interaction described so far is applicable to objects with a size of several microns up to millimeters in various every-day situations where cohesive forces between the particle bodies are small compared to the capillary force just described [Her05]. A prominent example is wet sand or soil, found from landslides to sandcastles, usually in a dense state. The model system of this thesis is a billiard system with low densities. A possible example, which is however unstudied from this viewpoint so far, might be hail stones in the so called *wet-growth regime* [PK97, Sec. 16.1.1]: While a hail stone passes through supercooled air it collects condensing water droplets. When freezing this water releases latent heat. If the conditions do not allow for sufficient heat transport more water is collected than freezes and the hail stone will under certain conditions be surrounded by a water layer. On a speculative basis liquid bridges might, among other interactions, offer an explanation to the formation of aggregated giant hail stones as shown in Fig. 1.4.

Contact deformation of spherical dust grains. Another mechanism for velocity-independent dissipation caused by a hysteretic potential can be found in astrophysics ([CTH93],[DT97]): Typical grain sizes in interstellar medium range from angstrom to several nanometers. The particles considered here are thus much smaller than those in typical every-day granulates, and van-der-Waals/adhesion effects of the grain material itself are no longer negligible as attractive interactions. In fact their strength in dust-particle collisions may be direction-dependent and may cause an interaction potential very similar to the one caused by liquid bridges: When two particles initially collide the contact region is small and with it the adhesion forces. The impact, however, leads to a small deformation of the contact zone, which enlarges as consequence. A larger contact zone means larger contact forces that have to be overcome to separate the particles again.

Before separation (given high enough relative speeds to prevent clustering) the two grains will even form a small "neck" out of grain material similar to a liquid bridge (Fig. 1.2). It should be noted that viscoelastic dissipation is inherent in contact deformation. A clear separation of dissipation due to inelasticity of collisions and rupture of the material is thus more difficult than in the case of wet granular matter. Although we stress the broader applicability of the interaction, wet granular matter will serve as exemplary system.

1.1.3 The thin-thread model

The scope of this thesis is to closely investigate the peculiarities of the wet interaction described in the last section. To concentrate on the substantial properties we introduce a simplified model of liquid bridges, the *thin-thread model*[2] [FRHH08] depicted in Fig. 1.1. It reduces the wet interaction to its two core features: Hysteresis is obtained by switching on and off of the potential well and velocity-independent dissipation results from the constant depth of the potential well. The potential is characterized by the bridge-rupture distance s_c and the bridge-rupture energy ϵ. Both features are quantitatively determined by the liquid volume (Eqs. 1.3 and 1.4).

The success of the thin-thread model in simulations demonstrates that it indeed captures all important features of liquid-bridge interaction. The thin-thread model was introduced in [FRHH08] because the piecewise force-free motion is especially suitable for fast, event-driven computer simulations where collision and bridge rupture interrupt the ballistic flight of particles as instantaneous events. In [FRHH08] the authors find that the phase diagram of vertically shaken wetted granulates obtained from simulations based on the thin-thread model compares well to experimental data. Moreover, simulations using the thin-thread model are found to largely coincide with molecular dynamics simulations with the microscopically more realistic *minimal-capillary model*. The latter approximates the bridge force by a constant rather than by Eq. 1.2 and thus corresponds to a linearly increasing potential. In conclusion, the thin-thread model is not only a conceptual model of wet granular matter but has practical relevance as well.

The thin-thread model describes a dissipative interaction in a "potential-framework": At every point the particle dynamics takes part within a potential landscape. Nevertheless the difference in potential when separating as compared to approaching changes the potential energy of a particle without accordingly changing the kinetic energy such that the total energy is reduced. The motivation of this thesis it to find out how this uncommon interaction, which combines features of dissipative and Hamiltonian system affects particle dynamics.

Thick-film vs. thin-film thin-thread model. So far the thickness of the uniform liquid film has been neglected as compared to the bridge-rupture distance s_c. This is physically justified and means that liquid bridges are only formed during a collision. This variant is named *thin-film* model as opposed to the *thick-film* model in which the thickness of the uniformly spread liquid film and the bridge-rupture distance are taken to be the same. In the thick-film case liquid bridges can also form if only the films but

[2]The thin-thread model got its name because the interaction it describes resembles a piece of thread connection two beads: As long as it is not maximally elongated it exerts no force. When stretch up to the rupture distance, however, the thread suddenly exerts a radial force.

not the grains are in contact. In Fig. 1.1, the potential well would thus appear as soon as the radial distance between particles becomes smaller than the bridge-rupture distance s_c. Macroscopic results like temperature development in free cooling have been found to be independent of the exact implementation of the thin-thread model [UAZ+09]. In the present context we will mainly focus on the thin-film but sometimes compare to the thick-film variant of the thin-thread model to detect microscopic differences.

1.1.4 Free cooling and shearing

As a dissipative system (wet) granular matter is necessarily studied as an open system coupled to a certain environment. The specific environment reflects back on the statistical properties of the system. Thus, the billiard model for wet granular matter is studied in at least two different environments to get an impression about their influence.

Chapter 2 deals with a *freely cooling* granular billiard. A freely cooling granulate is free of external forces (especially of gravity) so that the "environment" only consist of the internal particle degrees of freedom that are excluded from consideration and into which the liquid bridge energy is dissipated. Without energy input, the *granular temperature* T, which is defined via the average kinetic energy $\langle E\rangle$ of the granular particles, $T \propto \langle E\rangle$, steadily decreases, i.e. the system "cools" down. Experimentally, free cooling is hard to realize as gravitation has to be compensated. For dry granulates, the authors of [MIMA08] managed to do so in the laboratory using diamagnetic levitation. For wet granulates, however, such a study is still missing. Due to these difficulties free cooling is mainly studied in computer simulations [UAR+09, UAZ+09]: The temperature decrease with time is found to be adequately described by

$$\partial_t T \propto f_{\text{coll}} \cdot \epsilon \cdot P_{\text{bridge}},$$

where f_{coll} is the collision frequency, ϵ the bridge rupture energy and P_{bridge} the probability that a collision is followed by a bridge rupture, i.e. $1 - P_{\text{bridge}}$ is the probability to cluster in a collision. Naturally the interesting part of this ansatz is to estimate f_{coll} and P_{bridge}.

In Chapter 3 *shearing* is added as driving mechanism to the billiard model. As shearing occurs in many natural situations it can be realized experimentally. In computer simulations, there are different ways to implement shearing. A cosine shear profile was applied to a wet granulate in [RVH09] and found to result in stable or oscillatory unstable steady states. A linear shear profile can be implemented by *Lees-Edwards boundary conditions* [AT87, Sec. 8.2], which will be used in Chapter 3. Lees-Edwards boundary conditions are a type of periodic boundary conditions where the periodic images at two opposite sides of the simulation box, e.g. the periodic images to the top and to the bottom, are moving with constant speed s (Fig. 1.5). Passing over into such a moving periodic image corresponds to a change of coordinates into a moving frame of reference. We discuss briefly how the kinetic energy of a particle is affected by crossing such a boundary. First, we observe that Lees-Edwards boundary crossings are symmetric with respect to rotations by π. It is thus sufficient to consider only the top boundary. Let v_x be the velocity component parallel to the Lees-Edwards boundary and $v_y > 0$ the perpendicular component. Then the energy

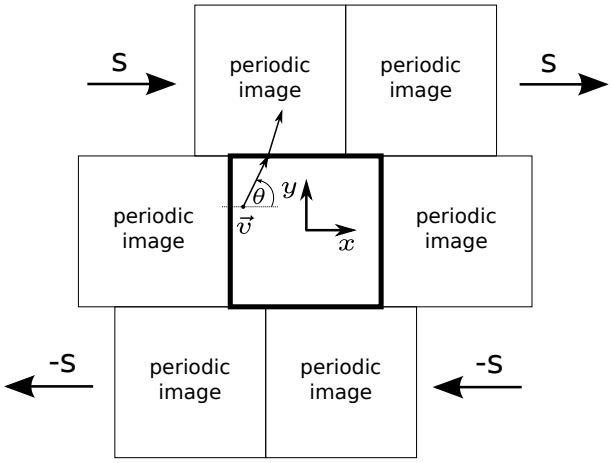

Figure 1.5: **Lees-Edwards boundary conditions** are characterized by periodic images at two sides that move with a constant velocity s. Transforming a velocity $\vec{v}$ into one of these moving images corresponds to a coordinate change into a moving frame of reference so that the component of $\vec{v}$ parallel to the moving boundary changes. On average, Lees-Edward boundary crossings increase the speed $|\vec{v}|$ (see main text for further details).

$E = v^2/2 = (v_x^2 + v_y^2)/2$ changes according to

$$\begin{aligned} 2E' &= (v_x - s)^2 + v_y^2 = v^2 + s^2 - 2sv\cos\theta \\ \Rightarrow \Delta E &= E' - E = \frac{s^2}{2} - s\sqrt{E}\cos\theta, \end{aligned}$$

where the angle $0 \leq \theta < \pi$ is the trajectory angle in the upper half as depicted in Fig. 1.5. Assuming a uniform distribution of directions θ the kinetic energy is on average found to increase:

$$\langle \Delta E \rangle = \frac{1}{\pi} \int_0^\pi \Delta E \, \mathrm{d}\theta = \frac{s^2}{2}. \tag{1.6}$$

Thus, Lees-Edwards boundary conditions drive a system. Lees-Edwards boundary conditions have been applied to a wet granulate in [Bri09, Rah09]. Surprisingly, a steady state temperature is only observed up to a critical shear rate. For higher shear rates the system is steadily heated. No explanation for this behavior exists so far, which further motivates us to study the combination of Lees-Edwards boundary conditions with wet granular matter in detail.

1.2 Sinai billiard

1.2.1 Chaoticity and the foundations of statistical physics

Statistical physics relies on the underlying dynamics to be sufficiently random or chaotic, respectively. Dynamical systems theory has developed a detailed hierarchy distinguishing different degrees of randomness (e.g. [Ott02, Sec. 7.6]). In the present context, however, it is sufficient to restrict the discussion to *ergodicity* and a general notion of *strong chaoticity*.

Ergodicity as well as chaoticity are properties of a dynamical system on a subset of the phase space. For a Hamiltonian system the relevant subset is usually the energy surface while for dissipative systems a chaotic attractor or saddle might be relevant [TG06, Box 7.4]. The respective domain will for the remainder of this section simply be referred to as the *phase space*.

A dynamical system is ergodic if almost every initial conditions comes arbitrarily close to any point of the phase space in the course of time (for a detailed discussion see e.g. [Dor99, Mac03]). Ergodicity thus justifies to replace the time-averages of macroscopic quantities by ensemble averages, i.e. a statistic handling of the microstates. Ergodicity for Hamiltonian systems furthermore implies the uniformity of the microcanonical ensemble upon which Gibbsian equilibrium statistical mechanics is based [LP73].

Ergodicity does not imply chaoticity in the sense of strong sensitivity on the initial conditions and fast separation of neighboring trajectories. As a counterexample, imagine two neighboring phase points ergodically exploring phase space without ever separating. The separation of neighboring trajectories is also termed *mixing* as an initially connected set will be spread out (see again [Dor99, Mac03]). When referring to "strong chaoticity", mixing over the phase space will be meant. Chaoticity in this sense implies ergodicity and is thus the stronger concept.

Strong chaoticity is required for any coarse-grained, i.e. stochastified, mesoscopic treatment of the full microscopic dynamics [vK61]. In particular, Boltzmann's equation is based on the assumptions of molecular chaos and with it kinetic theories and hydrodynamics (e.g. [Sch06, Chapter 9]). Moreover, only strong chaoticity ensures that an arbitrary initial distribution evolves towards a (local) equilibrium distribution. Consequently, strong chaoticity of the underlying dynamics is especially crucial for non-equilibrium statistical physics [Dor99, Sec. 1.6].

In the present context we will numerically access the properties of a dynamical system given by a map M via its *natural distribution* with measure μ_∞ and – if it exists[3] – density ρ_∞ on the phase space X. If M is chaotic, the natural distribution is obtained as the long-time limit towards which a smooth initial distribution $\rho_0(x)$ converges under the action of M [TG06, Sec. 5.4.4]:

$$\rho_0(x) \xrightarrow{M\circ M\cdots\circ M} \rho_\infty(x).$$

In practice, the distributions are sampled by an *assembly* of systems with different initial conditions whose distribution on X is observed as a function of time. Variation of the initial assembly and distribution rules out pathological cases. For a system that is ergodic but not mixing a localized initial condition does not eventually fill, i.e. sample, the total phase space at each time step. Therefore the assembly has to be traced out over time spans in this case, relying on the equivalence of time and ensemble averages.

We note that the asymptotically relevant part of phase space is given by the support of the natural distribution, which corresponds to the attractor of the system and that in the context of classical statistical mechanics the term "ensemble" is used to refer to the natural distribution.

[3]Note that from a probability density function $\rho(x)$ a measure $\mu(S)$ can be induced as $\mu(S) := \int_S \rho(x)\,\mathrm{d}x$ where S is some region. There might, however, be measures (in particular for fractal distributions) that do not correspond to a density function and are thus the more general concept.

So far we have elaborated that chaoticity (ergodicity) is the fundamental assumption of statistical physics. But can it be rigorously justified from the microscopic dynamics? In fact, so far a mathematical proof only exists for a few systems while also counterexamples have emerged [LP73].

In this context *dynamical billiards* are very important: Billiards are an efficient reduction of the dynamics of hard ball systems, i.e. of colliding smooth spheres modeling simple fluids, and allow to study their microdynamical properties [Szá00]. So far, however, chaoticity has been proven for two elastically colliding particles (corresponding to the *Sinai billiard*, which will be discussed in the next section) while the general proof for many elastically interacting particles [Sim10] and for systems of two particles with other types of interactions [Liv00] are challenging fields of active research in mathematics.

Before discussing billiard systems in detail, some relativizations concerning the seemingly weak basement of statistical physics are at place: So far only microscopic dynamics have been considered to provide chaoticity. There are, however, other sources of chaoticity. Those include external perturbations and randomness that is provided externally, e.g. by a random grid or amorphous material in which the dynamics takes place [Dor99, Sec. 1.3]. In real life the thermodynamic limits comes additionally to aid as sharp distributions effectively restrict the phase space so that chaoticity is only required on a small domain. Furthermore large numbers of particles help to decrease correlations [Dor99, Sec. 17.5].

From a physicist's point of view, therefore, the question of ergodicity and chaoticity is not whether it holds but in what sense and how exactly these properties may be interpreted and formulated as a basis of statistical physics. For (wet) granular materials these questions are still open. Even when no dramatic findings are expected for wet granular matter, it is of fundamental interest how dissipation and hysteresis as occurring for the wet interaction manifest themselves in the structure of the natural distribution.

1.2.2 Description and interpretation

In general a dynamical system describing the free motion of a point particle that is elastically reflected from piecewise-smooth boundaries is called a *(dynamical) billiard* (cf. [Bun07]). Elastically reflected means that – according to the law of reflection – incident and exit angle are the same and that energy is conserved. If the interaction is not modified, billiards are thus Hamiltonian systems. Depending on the shape of their boundary billiard systems can exhibit and represent all possible types of behavior found for Hamiltonian systems (cf. [Bun07]) and are therefore a valuable tool in this field of study.

Sinai billiards, named after Yakov Grigorevich Sinai who introduced them in 1960s, are a special type of billiards characterized by boundaries that are everywhere *dispersing*, i.e. have outward curvature. The 2-dimensional prototype of a Sinai billiard consisting of a circular scatterer centered in a square with periodic boundary conditions is depicted in Fig. 1.6. Note that the periodically connected square is equivalent to the 2-dimensional torus.

The dispersing boundary of the Sinai billiard ensures that neighboring trajectories separate very fast. In fact, the specialty of the dispersing billiards is that Sinai could mathematically prove that they have the strongest chaotic properties (cf. [Bun07]). In

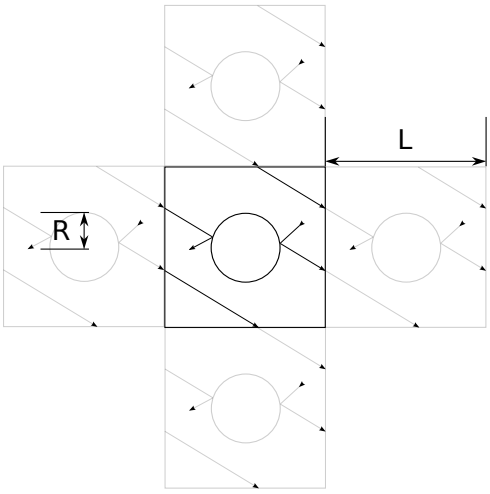

Figure 1.6: **The Sinai billiard** consists of a point particle that is elastically reflected from a circular scatterer and moves apart from that freely in a periodically continued square box. The *billiard geometry* is determined by the *scatterer radius* R and the *box size* L.

particular, they are mixing and ergodic on the energy surface.

As it describes the motion of a single 2-dimensional particle the full phase space of the Sinai billiard is 4-dimensional. In the elastic case, energy conservation restricts the motion to the 3-dimensional energy surface. The phase space can be reduced further to 2 dimensions by means of a *Poincaré section* where one only considers the discrete dynamics given by intersecting the full trajectory with the scatterer boundary. In other words, the discrete evolution of a phase point on the scatterer boundary is defined to be the point of first return to the boundary under the original continuous evolution. In particular, the discrete time is given by the number of collisions with the scatterer.

This *collision section* of the phase space is measure-preserving (cf. [Bun00]) so that a natural distribution observed on the Poincaré surface of section faithfully represents the one on the full phase space. Consequently, the Sinai billiard has an easy-to-visualize phase space and is thus also very suitable for numerical phase space studies.

Interpretation: Lorentz gas. There are two possible interpretations of the Sinai billiard. Interpreting the periodic boundary conditions as an infinite rectangular grid of scatterers leads to the quadratic *Lorentz gas*. Here, a light particle is moving in an array of scatterers that are so heavy that their momentum is not changed by the collisions with the light particle. The Lorentz gas was proposed as a model for the motion of an electron between atomic cores in a metal by Hendrik Antoon Lorentz. In a granulate, however, particles are of comparable size and moreover not regularly ordered so that this interpretation does not seem appropriate. The Lorentz gas picture is nevertheless useful to distinguish between general types of motion depending on the density and position of scatterers: If the length of a free path between two collisions is (un)bounded the Lorentz gas is said to have an *(in)finite horizon* (cf. [Bun00]). Clearly, a Lorentz gas on a quadratic lattice always has an infinite horizon due to collision-free flights parallel to the grid structure. This might be mathematically troublesome, for the numerical phase space studies intended in this thesis it is unproblematic, however, as the pre/post-collision Poincaré map prevents statistical dominance of seldom colliding trajectories. By choosing

a triangular lattice one can remove collision-free flights for sufficiently large scatterers (cf. [Los07, Sec. 9.1]). However, an open horizon is unavoidable for the sheared Sinai billiard in Chapter 3.

Interpretation: Relative motion of two disks in a box with periodic boundary conditions. The second interpretation of the Sinai billiard is the relative motion of two particles in the plane. As visualization is hard for the 8-dimensional phase space of the two particles in the plane the great advantage of the following reduction is the 2-dimensional billiard phase space that nevertheless keeps the important features.

Take two hard disks of equal mass without rotational degrees of freedom that interact via elastic collisions. To allow for more than one collision periodic boundary conditions are imposed. To prevent simultaneous interaction with two periodic images, which would contradict the two-particle interpretation, only dilute two-particle gases are taken into account. The two disks exert equal and opposite forces onto each other so that the center of mass moves rectilinear-uniformly. This movement remains unaffected by application of periodic boundary conditions if the two particles cross the boundary simultaneously. For disks with equal masses this is the case and allows for choosing the center-of-mass system as reference system.

The two disks with position vectors $\vec{r_i}$ cannot approach each other closer than the sum of their radii R_i,

$$|\vec{r}| = |\vec{r_2} - \vec{r_1}| \geq R_1 + R_2 =: R,$$

and collide for $|\vec{r}| = R$. Consequently, the relative motion corresponds to the motion of a point particle with position $\vec{r}$ that is scattered from a circle of radius R (cf. Fig. 1.6). As the hard core potential governing the elastic collisions gives rise to a radial force, the tangential part v_t of the relative velocity $\vec{v}$ remains unchanged by a collision while the radial component v_r is reversed:

$$\text{collision:} \qquad \vec{v} = v_t\vec{e_t} + v_r\vec{e_r} \quad \mapsto \quad \vec{v}' = v_t\vec{e_t} - v_r\vec{e_r}.$$

An elastic collision thus changes $\vec{v}$ according to the law of reflection. The description of the relative dynamics is completed by the update of $\vec{r}$ according to the periodic boundary conditions, which can be interpreted as moving the origin of the coordinate system to the adjacent periodic image:

$$\text{boundary:} \qquad \vec{r} \quad \mapsto \quad \vec{r} \mod L.$$

In between collision and boundary crossing the motion is ballistic and the relative dynamics described above is just the situation of a Sinai billiard (cf. [Tab05, Example 1.10]).

A similar reduction is possible for more than two particles in more than two dimensions [Dor99, Sec. 18.4]. The crucial difference occurring, however, is that the scattering boundaries, which determine the regions in configuration space prohibited to the relative motion become cylinders in contrast to the circular scatterer of the Sinai billiard. A cylinder is not dispersing along its sides, which complicates the treatment of higher dimensions. The present study therefore focuses on the properties of 2 disks in a periodic box where standard tools of dynamical systems theory are available.

We stress that collisions of two particles are also at the heart of the Boltzmann equation, which neglects many-particle correlations. Studying two particles interacting according to the thin-thread model (Sec. 1.1.3) might thus eventually give hints how a Boltzmann equation for wet granular matter should look like and how the inherent irreversibility caused by the hysteresis could be taken into account.

To study free collision of two wet particles the Sinai billiard will be amended by the wet interaction in the next chapter. In Chapter 3, the billiard is further generalized by adding shear so that the dissipative two-particle collisions can also be studied in a driven setting.

Chapter 2

Freely cooling wet billiard

This chapter is concerned with the question if and how the hysteretic interaction in the absence of any driving mechanism manifests itself in phase-space structure. Due to its low-dimensional and illustrative phase space the Sinai billiard (Sec. 1.2.2) with collision rules modified according to the hysteretic interaction serves as model system. As the hysteretic interaction combines features of Hamiltonian and dissipative systems it is not clear whether the natural distribution will remain uniform (on the energy surface) as for the classical Sinai billiard or whether the dissipation causes structure in the natural distribution. To further illustrate the question we shortly discuss how dissipation typically affects the natural distribution.

The classical Sinai billiard conserves energy during collisions and is thus a Hamiltonian system. Due to Liouville's theorem the volume of some subspace will not change when the system is evolving (at least if canonically conjugate variables are used). The shape of this subspace, however, may be heavily deformed. To ensure volume conservation, contraction (slenderizing along stable directions) and stretching (broadening along unstable directions) thus balance in Hamiltonian systems. On the other hand, the interaction between (wet) granular particles dissipates energy and is thus expected to contract phase volume along the decreasing momentum coordinates.

The effects of this phase space contraction are best illustrated by the *baker map*, which is a very simple but powerful model for the interplay of stretching and folding in phase space. The baker map (e.g. [TG06, Sec. 5.1]) acts on the unit square, which might correspond to a small region in the phase space of a more complicated dynamical system, as shown in Fig. 2.1. As illustrated, the baker map does nothing else than stretching (by a factor 2), compressing (by a factor c) and some kind of folding of the phase space[1]. If the compression factor is $c = 1/2$ the baker map is volume/area conserving so that its image is again the whole unit square. For $0 < c < 1/2$ phase volume is contracted as in a typical dissipative system. In this case the unit square evolved by the baker map approaches a fractal attractor (e.g. [TG06, Chapter 2]) whose projection onto the x-axis is the Cantor set.

For the minimal capillary model, which is conceptually equivalent to the thin-thread model studied here (cf. Sec. 1.1.3), symplecticity, which implies volume conservation [Ott02, Sec. 7.1.1], has been formally shown [HF07, Sec. 4.6]. On the other hand, dissipa-

[1]The folding can be motivated as necessary to appear in a bounded phase spaces, which prevents infinite stretching of an initial volume.

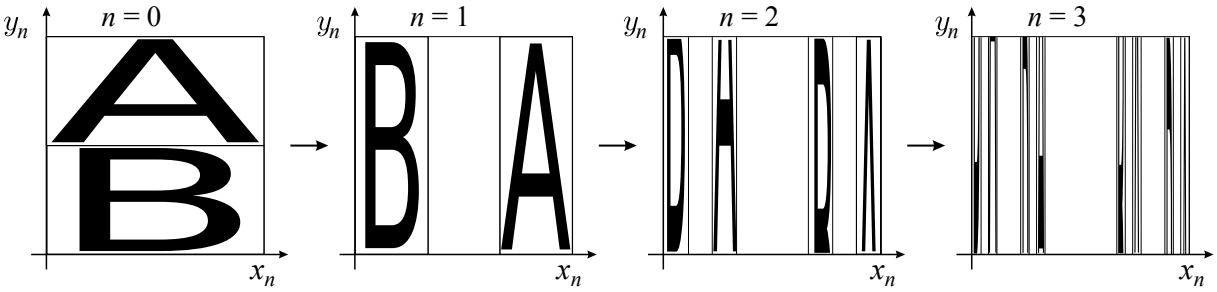

$$(x, y) \in [0, 1] \times [0, 1] \qquad B\,(x, y) = \begin{cases} (cx, 2y) & \text{for } y \leq \frac{1}{2} \\ [1 + c\,(x - 1)\,, 1 + 2\,(y - 1)] & \text{for } y > \frac{1}{2} \end{cases}$$

Figure 2.1: **The baker map** B acts similar to the way a baker treats the dow: The unit square as phase space is stretched by a factor 2 in the y-direction and compressed by a factor c in the x-direction. Finally, the stretched image is cut in the middle and put back onto the unit square. For $c = 1/2$ the volume of the unit square is conserved. For $c < 1/2$ (in the figure: $c = 1/3$) the volume decreases, which results in the fractal structure illustrated. The support of its projection onto the x-axis is the Cantor set. A compression factor of $c > 1/2$ would result in iterated double folding of the phase space (image after [TG06, Sec. 5.1.3]).

tion should manifest itself in some way and the sudden change of the potential landscape seems not to be included in the formal treatment. So far it has thus remained an open question in what sense the wet interaction is or is not volume-preserving.

From the statistical-physics point of view the main concern is not whether or not the natural distribution is uniform but how strong a possible structuring turns out to be. If the distribution or its projections are still sufficiently well approximated by a uniform distribution no extra care has to be taken, at least from this direction, in formulating the statistical physics of wet granular matter.

2.1 The system

For the sake of this discussion we employ dimensionless units if suitable: The energy E is measured in units of the bridge-rupture energy ϵ (cf. Fig. 1.1), and lengths, in particular the box size or periodicity of the billiard L (cf. Fig. 1.6) and the rupture distance (cf. Fig. 1.1) of the liquid bridge s_c, are given in units of the central-disks radius R (cf. Fig. 1.6). Furthermore, mass is set to unity so that speed is given by $v = \sqrt{2E}$.

The collision rules of the Sinai billiard are modified in order to include the wet interaction (see Fig. 2.2). The liquid bridge exerts a radial force and reduces the radial energy $E_r = v_r^2/2$ by an energy ϵ, thus causing the velocity to tilt:

$$\text{boundary:} \qquad \vec{v} = v_t\vec{e_t} + v_r\vec{e_r} \quad \mapsto \quad \vec{v'} = v_t\vec{e_t} + \sqrt{v_r^2 - 2\epsilon}\,\vec{e_r}. \tag{2.1}$$

If $E_r < \epsilon$ the liquid bridge cannot be ruptured and both particles stick together and form a *cluster*. As systems in this state do not explore the phase space anymore they will be excluded or separately analyzed in the following.

As bridge rupture punctually interrupts the ballistic motion in the same way as boundary crossing and collision do the relative dynamics is still given by a sequence of straight

line segments now connected by one of the three events:

- **collision** (totally elastic, following law of reflection)
- **bridge rupture** (dissipation, trajectory tilts)
- exit and entrance according to **periodic boundary conditions** (preserves energy and direction of the trajectory)

We note that the dynamics remains completely Hamiltonian (and therefore measure-preserving) in between the sudden switch-ons of the thin-thread potential. Consequently, the post/pre-collision Poincaré section still serves its purpose. Furthermore, the collision sections are sections of constant energy: On each collision, the system energy is reduced by the constant amount ϵ while it is preserved in between. Hence the initial energy E_{ini} and the number of collisions n the system has experienced so far completely determine the current energy:

$$E(n) = E_{\text{ini}} - \epsilon \cdot (n-1) \tag{2.2}$$

Here the factor $(n-1)$ appears since after the nth collision the nth bridge has formed but is not yet ruptured. As the collision Poincaré section features the number of collisions n as evolution variable, this equivalence of energy and "time" prevents the need of an extra energy coordinate. The phase space of Poincaré sections remains 2-dimensional.

Note that the tilting bridge rupture is dispersing so that the spatial dynamics of the wet Sinai billiard will remain strongly chaotic (cf. Sec. 1.2.2). Even if the energy coordinate would not have been eliminated by the Poincaré section, problems concerning chaoticity are not to be expected as the thin-film interaction was argued to even increase separation of trajectories ([Her05, Sec. III.A], [FHZ07]).

The unbalanced dissipation caused by the wet interaction continually decreases the system energy analogously to the free cooling of many-particle wet granulates (Sec. 1.1.4): The "granular temperature" (see Sec. 1.1.4) of the billiard system is directly given by Eq. 2.2 as there are no temperature fluctuation for a given initial energy. The situation is thus reminiscent of a microcanonical ensemble. In the many-particle case the temperature decrease is proportional to the collision frequency f_{coll} and to the bridge rupture energy, $\partial_t T \propto \epsilon f_{\text{coll}}$. The same is true for the billiard temperature with its trivial collision frequency $f_{\text{coll}} = 1$.

2.1.1 Coordinates, mapping and phase space

To take advantage of the line segments constituting the billiard trajectories and the symmetries of the events discussed in the last section it is convenient to use the following coordinates that emerge from the Cartesian description by a canonical transformation (Fig. 2.2, [Vol02, Chapter 4])

$$(q_1, q_2; p_1, p_2) \mapsto (\theta, -p; I, Q),$$

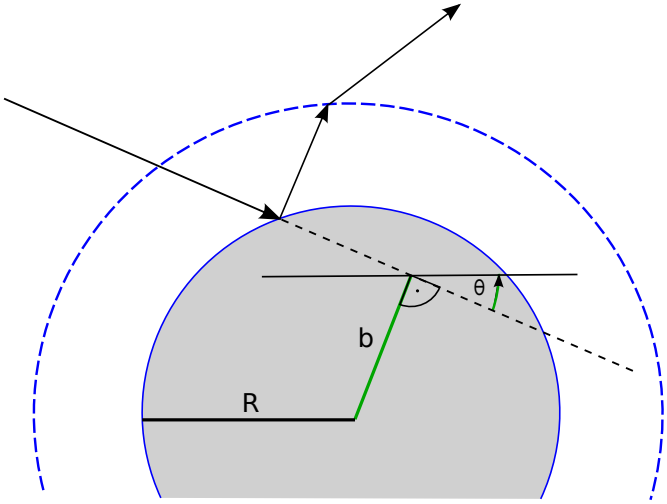

Figure 2.2: **The wet interaction** is included into the Sinai billiard by modified collision rules: The collision itself still follows the law of reflection while the bridge rupture reduces the radial velocity leading to a tilt of the trajectory. The line segments are conveniently described by an angle and the impact parameter.

where the new coordinates are:

$$
\begin{aligned}
I &= q_1 p_2 - q_2 p_1 && \text{(angular momentum)} \\
Q &= (q_1 p_1 + q_2 p_2)/p && \\
p &= \sqrt{p_1^2 + p_2^2} && \text{(absolute value of momentum)} \\
\theta &= \arctan\left(\frac{p_2}{p_1}\right) && \text{(angle of the trajectory with respect to the } q_1\text{-axis)}
\end{aligned}
$$

The corresponding generating function is

$$F_4(p_2, p_2; Q, I) = I \arctan\left(\frac{p_2}{p_1}\right) - Q\sqrt{p_1^2 + p_2^2}.$$

As canonical transformations are measure-preserving the new coordinates allow a meaningful description of the phase space.

The collision Poincaré section allows to eliminate Q: The value of Q specifies where exactly on a trajectory segment determined by I and θ the particle is located. The condition of lying on the boundary (applied either to pre- or to post-collision segments, which results in the two different but equivalent *pre-* and *post-collision sections*) then determines the 3-dimensional Poincaré surface of section as a subspace of (I, Q, p, θ)-space. A point on this surface is determined by (I, p, θ). Furthermore, the number of collisions n determines the system energy $E(n)$ according to Eq. 2.2 so that also the momentum $p(n) = \sqrt{2E(n)}$ is fixed. For a given $p(n)$ the dynamics is thus restricted to a 2-dimensional surface. In terms of the impact parameter

$$b := \frac{I}{p} \tag{2.3}$$

this surface is

$$(I, \theta) = (p(n) \cdot b, \theta) \in p(n) \cdot [-R, R] \times [0, 2\pi] \,,$$

where the values of impact parameters in a collision are restricted by the radius R as no collision occurs otherwise. Here $p(n)$ still appears as a scaling factor and shows that the immediate effect of the liquid bridge dissipation is a *homogenous rescaling* of phase space after each bridge rupture/before each collision. Being homogenous this scaling will not affect or cause any structuring in phase space and we will therefore omit the factor in the following. Eventually

$$(b, \theta) \in [-R, R] \times [0, 2\pi] \tag{2.4}$$

is the 2-dimensional phase space, which has to be supplemented by the number of collisions n and the initial energy.

In the (b, θ)-coordinates just introduced the billiard events are explicitly given by the following maps.

Collision. Due to conservation of energy and angular momentum E and b are unchanged. The angle θ changes according to the law of reflection as sketched in Fig. 2.3 (a and b):

$$\text{collision:} \qquad \theta \mapsto \theta' = \theta + \pi + 2 \text{ asin } b.$$

Periodic boundary. Applying periodic boundary conditions amounts to a change of coordinate origin. Thus, E and θ are unchanged. Rotating Fig. 2.3 (d) through an angle α that specifies whether the particle leaves to the right, top, left or bottom, respectively, gives for the impact parameter:

$$\text{boundary:} \qquad b \mapsto b' = b - L \sin(\theta - \alpha) \,, \qquad \alpha \in \{0, \tfrac{1}{2}\pi, \pi, \tfrac{3}{2}\pi\}. \tag{2.5}$$

Liquid bridge. According to the thin-thread model the energy is reduced by the bridge-rupture energy (Eq. 2.1)

$$\text{bridge:} \qquad E \mapsto E' = E - 1. \tag{2.6}$$

The liquid bridge exerts a central force so that angular momentum is conserved in bridge ruptures, $\sqrt{E} \cdot b = \sqrt{E'} \cdot b'$, and the impact parameter b changes according to

$$\text{bridge:} \qquad b \mapsto b' = \frac{b}{\sqrt{1 - \frac{1}{E}}}. \tag{2.7}$$

By using the relation above and Fig. 2.3 (a),

$$\frac{\sin\varphi}{\sin\varphi'} = \frac{b}{b'} = \sqrt{1 - \tfrac{1}{E}} \Rightarrow \varphi' = \text{asin } \frac{\sin\varphi}{\sqrt{1 - \frac{1}{E}}},$$

so that from Fig. 2.3 (c) the change of θ is found to be

$$\text{bridge:} \qquad \theta \mapsto \theta' = \theta + \text{asin } \left[\frac{b}{(1+D)\sqrt{1 - \frac{1}{E}}} \right] - \text{asin } \frac{b}{1+D}.$$

Figure 2.4 demonstrates that collision, bridge and boundary all act on (b, θ)-space as shearing.

Inelastic collisions instead of bridge rupture. For comparison, inelastic collisions (cf. Sec. 1.1.1) described by a normal, velocity independent coefficient of restitution $\alpha := v'^2_n/v^2_n$ will be considered. In that case the mapping is given by

$$\text{inelastic collision:} \quad \begin{cases} E = \frac{v^2}{2} & \mapsto \frac{v_t^2}{2} + \alpha\frac{v_n^2}{2} = \alpha + b^2(1-\alpha) \\ b & \mapsto \frac{b}{\sqrt{\alpha+b^2(1-\alpha)}} \\ \theta & \mapsto \theta + \pi + \operatorname{asin} b + \operatorname{asin} \frac{b}{\sqrt{\alpha+b^2(1-\alpha)}} \end{cases} . \tag{2.8}$$

It can be obtained by combining the conservation-of-angular-momentum argument employed for the bridge map with the collision map. Due to the variable energy dissipated the collision Poincaré section is no section of constant energy here. Consequently a 3-dimensional (b, θ, E) phase space is needed to characterize the billiard motion under this interaction. For comparison we will consider projections onto the (b, θ) plane, however. This is motivated by the fact that there is no inherent energy scale in the restitution billiard so that a change of energy just corresponds to a rescaling of time. The distribution of energies has no impact on the dynamics in itself.

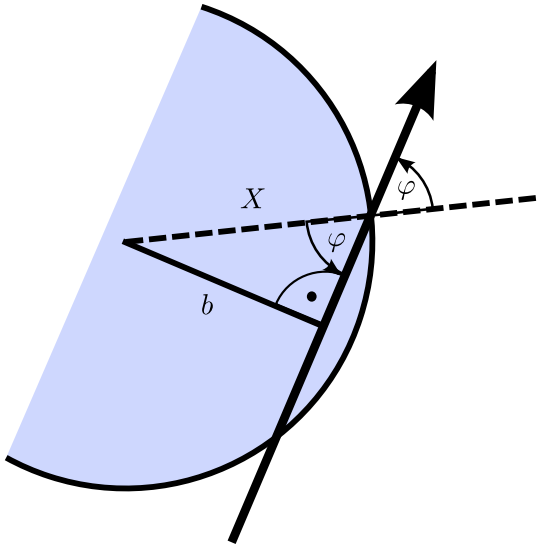

a) $\varphi = \text{asin}\ \frac{b}{X}, \quad X \in \{1, 1 + s_c\}$

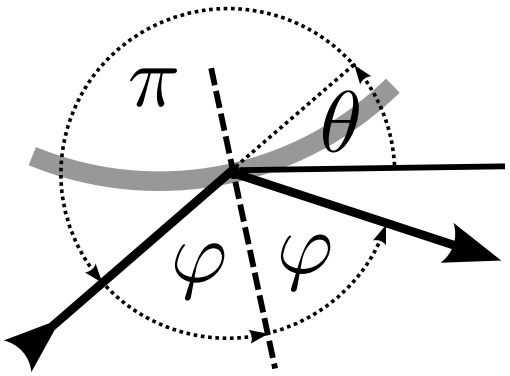

b) $\theta' = \theta + \pi + 2\varphi$

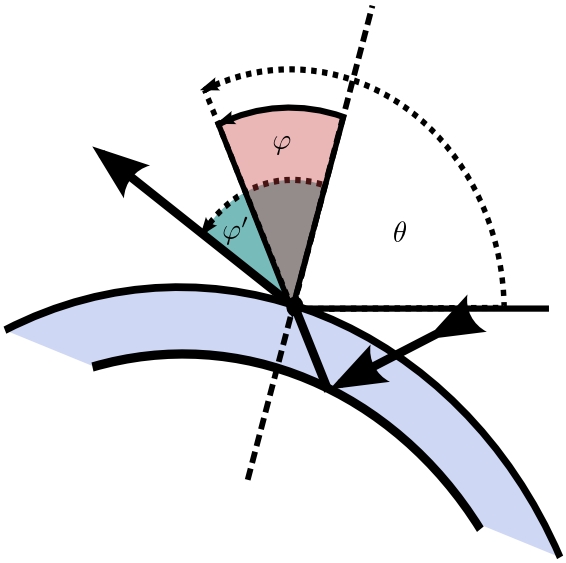

c) $\theta' = \theta + \varphi' - \varphi$

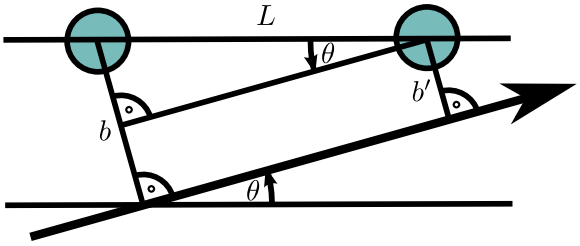

d) $b - b' = L \sin\theta$

Figure 2.3: **Derivation of the billiard maps. a)** The billiard maps are easiest formulated using the trajectory angle with respect to the surface normal, φ. As illustrated, it is readily obtained from the impact parameter b and the radius of the respective circle. **b)** Illustration of the law of reflection from the θ perspective. **c)** Bridge rupture as modeled by the thin-thread model tilts the trajectory as described by a change of θ. **d)** The application of periodic boundary conditions changes the impact parameter as depicted.

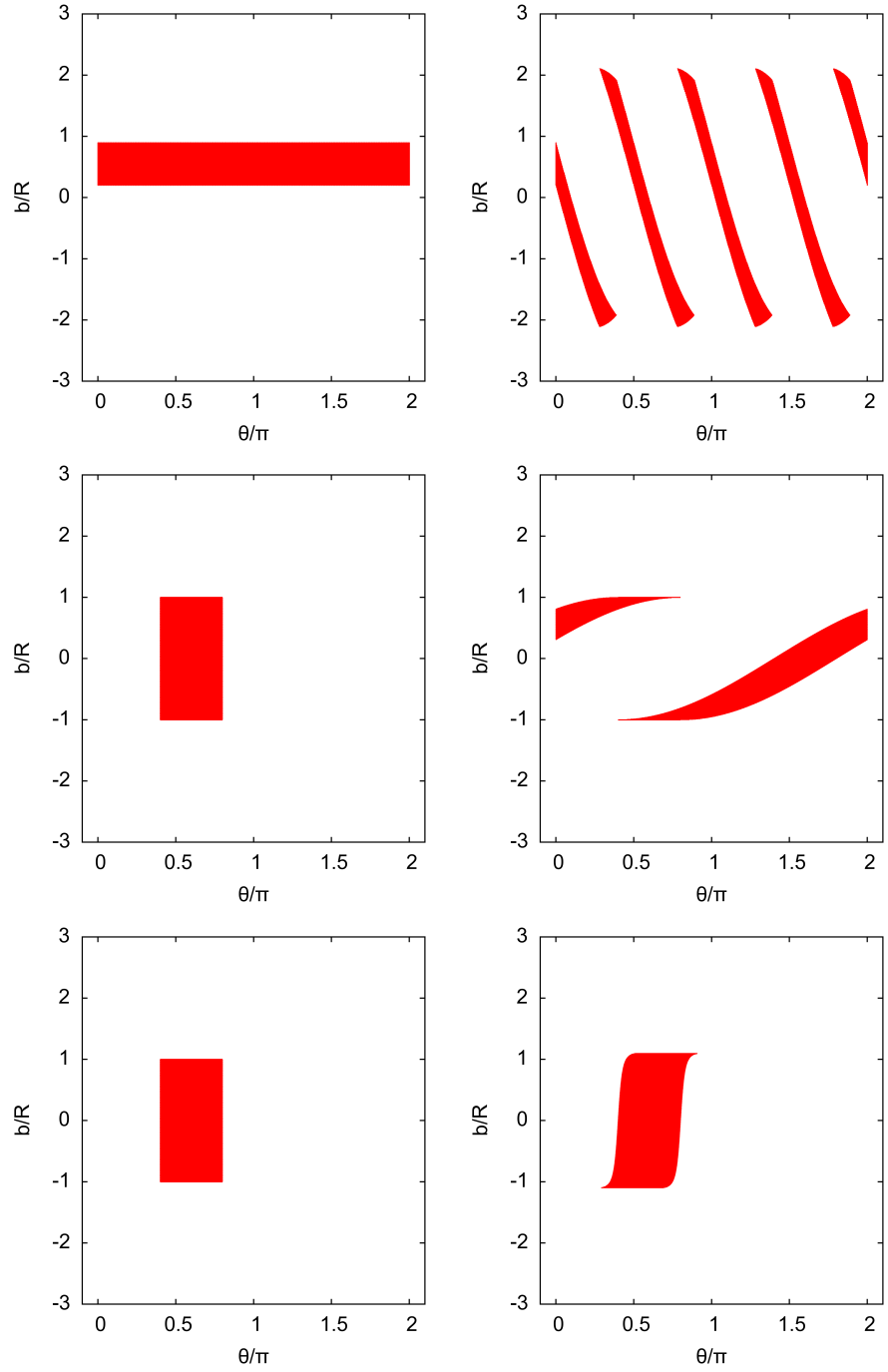

Figure 2.4: **Action of boundary, collision and bridge map on (θ, b)-space.** The initial assembly (left) is subject to one application of the boundary (top), collision (middle) or bridge (bottom) map, respectively. All maps act as shear in the phase space.

2.1.2 Implementation

Simulating the billiard trajectory of an initial state $(b, \theta, E_{\text{ini}})$ consist in successively updating the state according to the event maps derived in the last section. The event type following next is determined by the previous event and the coordinate values. The following diagram illustrates the possibilities: If the radial energy is large enough, $E_{\text{r}} > \epsilon$, a collision is for the thin-film model always followed by a bridge, which has then to be followed by a boundary crossing. After a boundary crossing and the corresponding change of the coordinate system a collision will follow if $b < R$. Otherwise another boundary crossing is performed. If a trajectory reaches the clustered state, i.e. $E_r < \epsilon$, the state is neither propagated nor printed in the following but removed from the assembly. If of interest, the number of clustered states occurring in an assembly of initial conditions is counted as function of time.

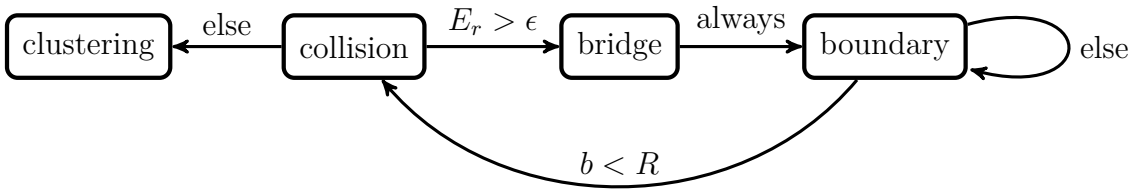

Note that for the boundary crossing the coordinate values of b and θ also determine whether the top, bottom, left or right boundary is crossed. In principle the open horizon of the Sinai billiard (Sec. 1.2.2) allows for an infinite series of boundary crossings. As these trajectories have measure zero in phase space they are however irrelevant for numerically determining the natural distribution. In practice, a trajectory is removed (and counted independently from the clustered states) if more than 10^4 successive boundary crossings were performed.

2.1.3 Transient chaos

Excluding the clustered states from consideration makes the wet Sinai billiard a *transiently chaotic* system: Due to the continuous cooling eventually all initial conditions will reach the clustered state, which is thus the attractor of the system. We observe the transient dynamics before this state is reached. This section quickly reviews some aspects of the theory of transiently chaotic systems that are relevant in the present context.

Transient chaos in general refers to dynamics that takes place on a *chaotic saddle*, i.e. a subset in phase space that is attracting in most directions but has also some exit directions towards an attractor [TG06, Chapter 6]. The exit towards the attractor is conveniently taken to be a *leak*, i.e. an absorbing region, from which trajectories cannot escape. This is exactly the situation in the wet billiard: The clustered states are treated as absorbing region and the saddle is characterized by the natural distribution of non-clustered systems. It is not immediately clear, what the natural distribution is on a chaotic saddle with asymptotic measure zero. As for numerical data in general, the natural distribution is understood here in the sense that the phase space distribution has relaxed away from the initial condition and not in a sense of a limit $n \to \infty$. Thus, to numerically observe the natural distribution on a chaotic saddle an assembly of initial conditions is propagated for

some steps until a steady situation appears. The distribution is then obtained from the frequency of systems in a certain state, normalized to the number of states that remain unclustered.

Trajectories exploring the chaotic saddle represent some kind of a metastable state and an important characteristic of transiently chaotic dynamics is the *lifetime* of trajectories within this state. For strongly chaotic systems the number of trajectories with different initial conditions $N(t)$ is generally expected to decay exponentially with an average lifetime $\langle\tau\rangle$ (cf. [TG06, Chapter 6], [Ott02, Chapter 5]):

$$N(t) \sim \exp\left(-\frac{\tau}{\langle\tau\rangle}\right).$$

This is readily illustrated by the natural assumption that the *rate of escape* from the saddle into the leak κ is given by the size of the leak. This "size" is given by the natural measure μ of the states that will be mapped into the absorbing region. When numerically sampling the respective phase space distribution, the measure of the absorbing region is determined by the trajectories that have been mapped into the absorbing region and will be removed in the next step. Moreover, the normalization has to be adapted to the remaining number of trajectories. With $\mu(L) = \kappa$ (which is just the inverse of the average lifetime τ):

$$\dot{N}(t) = -\kappa N(t) \quad \Longrightarrow \quad N(t) = N(0)\exp\left(-\kappa t\right)$$

Note that this exponential decay passes over to the distribution of lifetimes, $\rho(\tau) \sim \exp\left(\tau/\langle\tau\rangle\right)$,

$$\frac{N(t)}{N(0)} = P(T > t) = 1 - \int_0^t \rho(\tau)\,\mathrm{d}\tau,$$

where $P(T > t)$ denotes the probability that a trajectory has a lifetime $T = \tau > t$ and is thus not clustered at time t.

The concept of transient chaos is a generalization of asymptotic chaos and some research is done into this direction. In particular, extreme long-lived *supertransients* with decay rates decreasing algebraically with some parameter p, $\kappa \sim p^{-\alpha}$, have been discussed in the context of "boundary crisis", e.g. [TL08], [Ott02, Chapter 8]. In the context of enlarged lifetimes the exponential nature of the decay itself, however, has not been found to be modified for strongly chaotic systems. So far, non-exponential, in particular algebraic lifetime distributions, have only been found for *weakly chaotic* systems with "sticky regions" (see [AT09, Sec. VI] and ref. therein).

Before discussing the lifetimes of the wet billiard we turn to its natural distribution that is strictly speaking the distribution on the chaotic saddle of non-clustered states.

2.2 Numerical results for the natural distribution

Simulation. In this section we discuss the natural distribution of the freely-cooling wet billiard. Phase space distributions are obtained numerically as counting density on the phase space, i.e. the weight of each state is given by the frequency of finding an

assembly member in this state normalized to the number of assembly member that remain unclustered. To obtain the natural distribution a random initial distribution, i.e. an assembly of randomly initialized systems, is propagated according to the billiard dynamics (Sec. 2.1.2) until is has relaxed away from the initial distribution.

Observations. The structure of the phase-space distribution of two wet disks depends on the interaction. Figures 2.5 and 2.6 shows simulation results for the (b, θ) phase space of the Sinai billiard with totally elastic collisions and the wet billiard as well as a (b, θ) projection for the dry billiard with restitution (see Sec. 2.1.1). The Sinai billiard is a mixing Hamiltonian, i. e. measure-preserving, system and thus shows a uniform natural distribution (Sec. 1.2.2). As a "standard" dissipative chaotic system the restitution billiard is locally volume-contracting so that the interplay of expanding and contracting directions leads to a fractal phase space distribution as discussed at the beginning of this chapter. The wet billiard has features of both situations: It is dissipative but the dissipation can be hidden in a general rescaling of the momentum coordinate (Sec. 2.1.1). To a considerable extend it thus resembles a Hamiltonian system on every individual energy level. In Fig. 2.5/2.6 we observe that the wet interaction gives rise to structuring of the phase space that turns out to be fractal.

Before investigating how this phase-space structure emerges from the dissipation and hysteresis some general remarks:

Symmetries. The phase space shows symmetries according to the geometric structure of the quadratic lattice corresponding to the periodic boundary conditions. The four-fold rotational symmetry causes invariance under $\pi/2$-shifts and the mirror symmetry of the lattice results in an inversion symmetry of the phase space. This symmetry might be used to improve image quality by only plotting one symmetry block, i.e. $(b, \theta) \in [0, 1] \times [0, \pi/2]$.

Naturality. An initial distribution that is propagated by the freely cooling billiard dynamics cannot relax towards a natural distribution as the latter changes with energy. Consequently, Fig. 2.6 is a priori not expected to yield a good approximation of the natural distribution. To allow the system to relax towards a natural distribution the energy may be kept unchanged upon bridge rupture while b and θ are normally updated by the dynamics. Figures 2.7 and 2.8 show histograms of the wet phase space achieved with and without change of energy. They demonstrate that the stripe pattern only changes slightly with energy so that the difference is barely visible. The comparison further more confirms that the stripe pattern observed indeed is the natural distribution: It is reached independent of the initial conditions. For most purposes it will be sufficient to work with the cooling. This is very convenient as it allows easy access to the natural phase space distribution as a function of energy.

Pre- and post-collision section. (b, θ)-values directly before or directly after a collision constitute two equivalent Poincaré sections. Figures 2.7 and 2.8 show histograms of the wet phase space for these sections. Both show a stripy pattern yet the pre-collision section features nearly straight lines, which might be of advantage in the further analysis compared to the curves of the post-collision section.

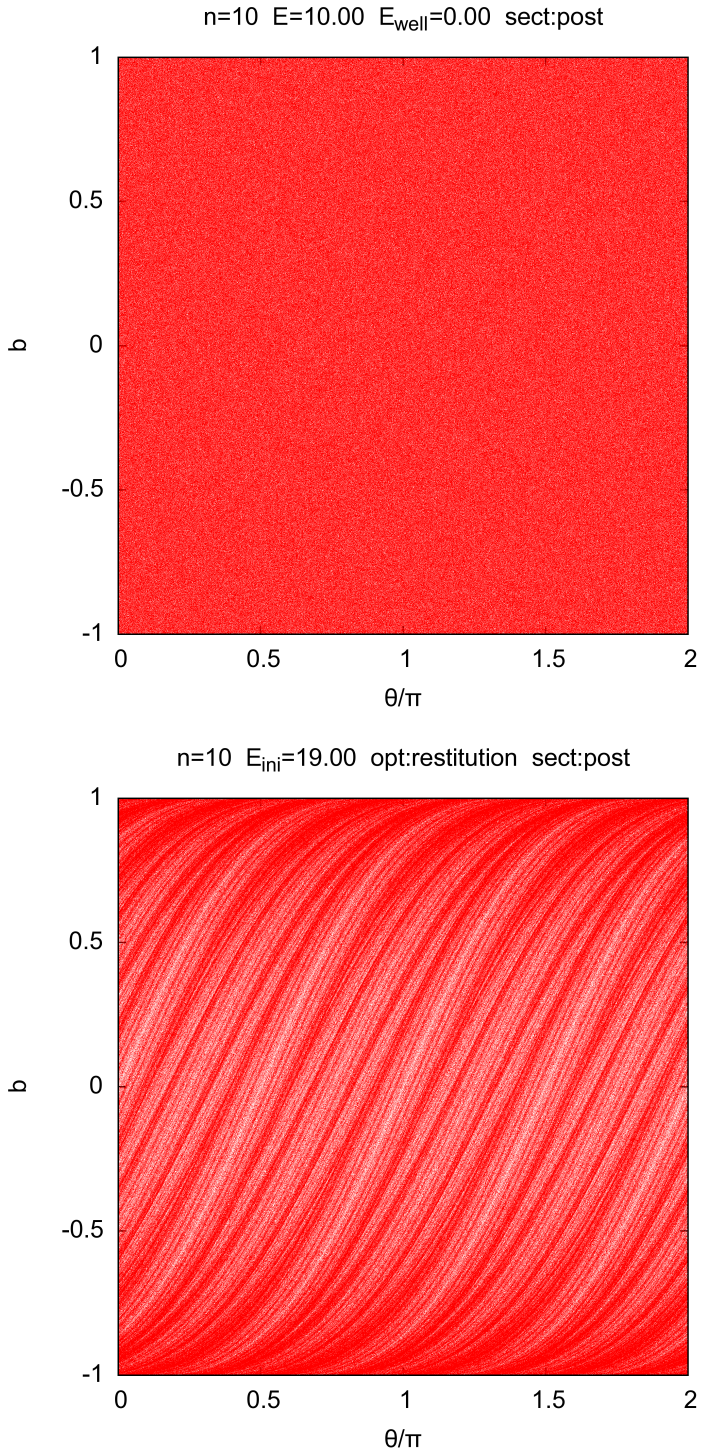

Figure 2.5: **Scatter plots of phase space distributions** obtained by iterating an assembly of uniformly distributed initial conditions according to the maps in Sec. 2.1.1 and printing the resulting states. The structure of the phase-space distribution of two disks depends on the interaction. As a mixing Hamiltonian system the classical billiard with totally elastic collisions (top) relaxes towards a uniform natural distribution, while the dry billiard with restitution (bottom) results in a fractally structured distribution. See Fig. 2.6 for continuation.

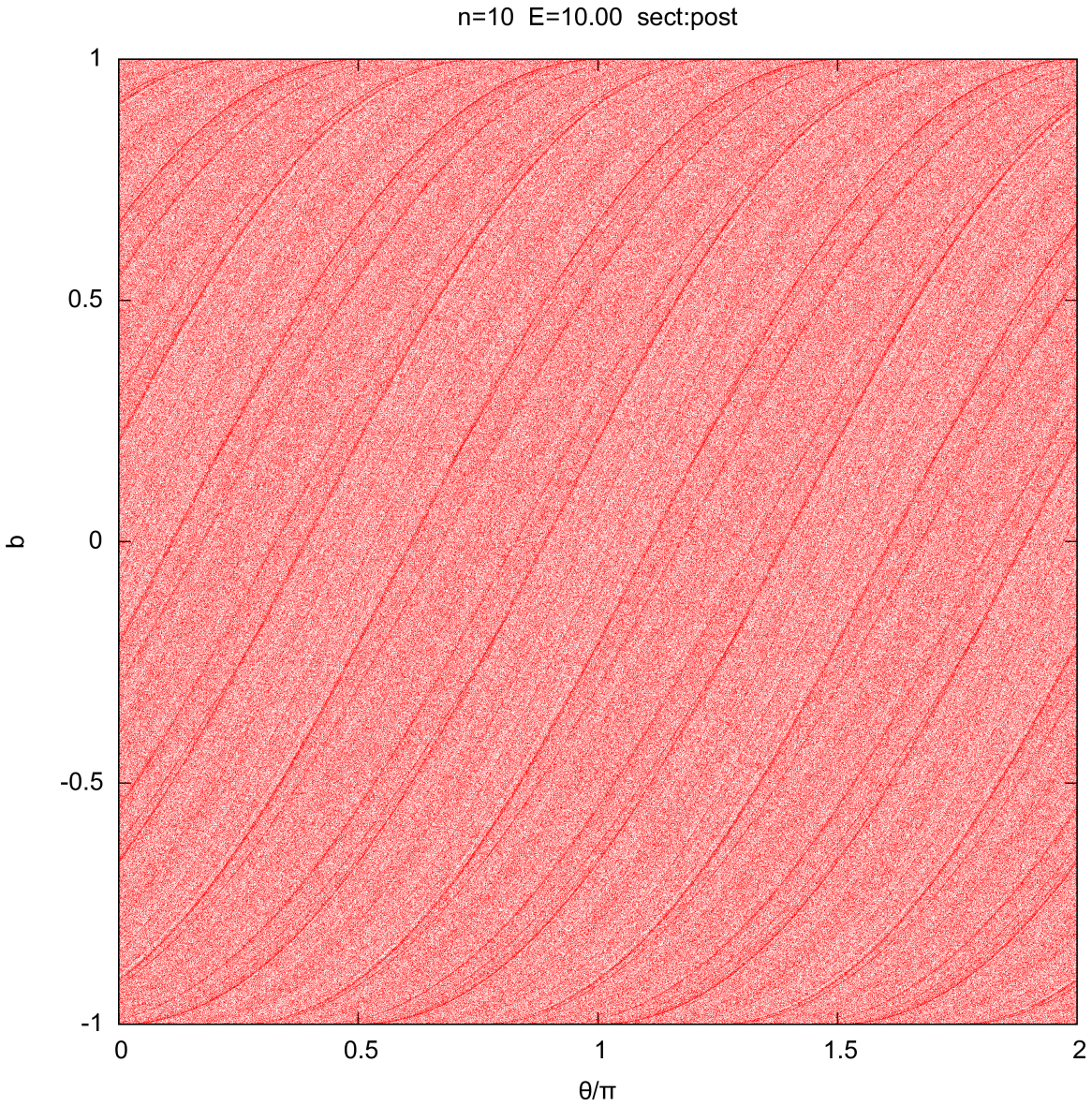

Figure 2.6: **Continuation** of Fig. 2.5: The wet billiard also shows a structured distribution. **Simulation details.** n: number of collisions, E_{ini}: initial energy, E_{well}: bridge rupture energy ϵ (the elastic billiard is obtained for $\epsilon = 0$), $E = E_{ini} - (n-1)\epsilon$: energy after n collisions, "opt": special simulation option here controlling the use of inelastic collisions, "sect": indicating if pre- or post-collision values are plotted. The plots have a resolution of 3000×3000 initial conditions. Apart from mentioned, default parameters were used (see Appendix A).

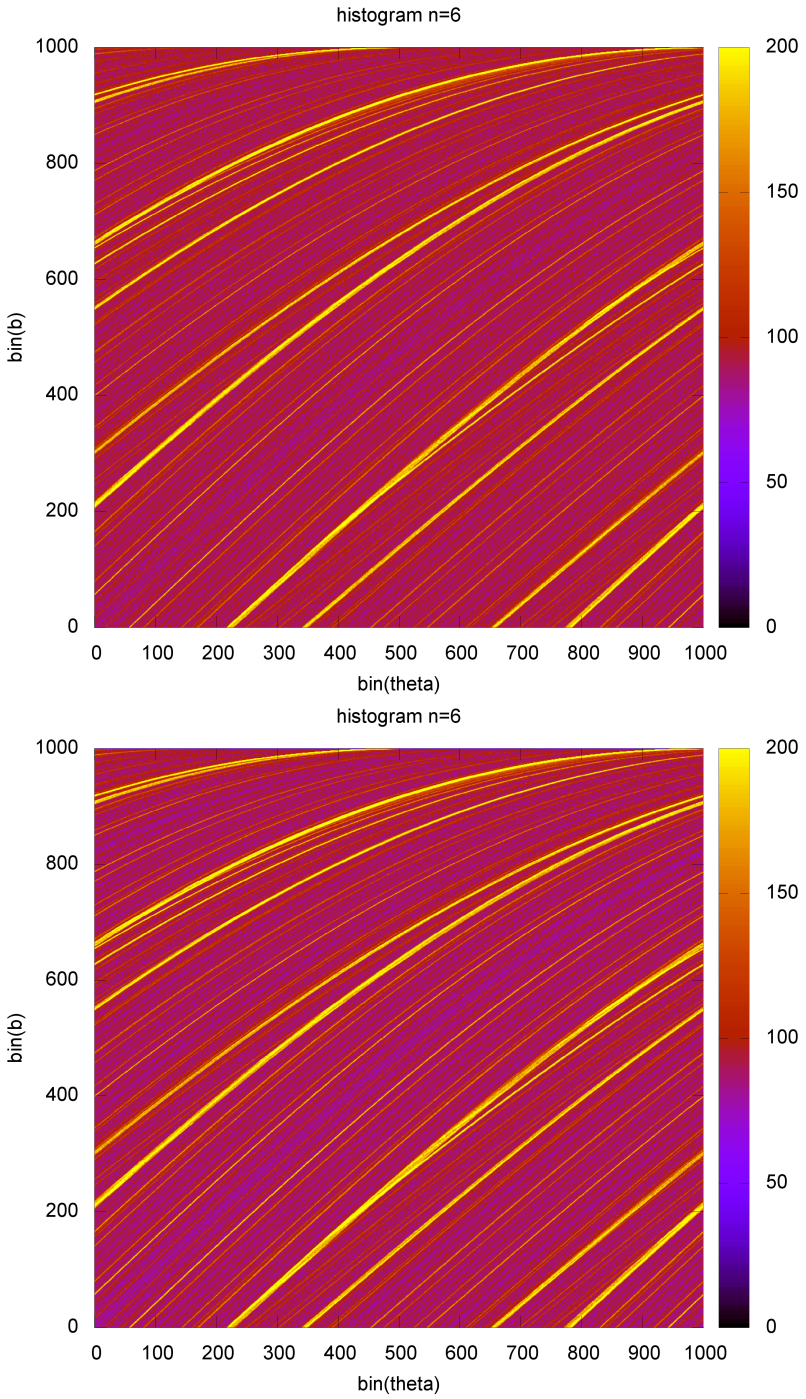

Figure 2.7: **Histograms of the symmetry-reduced wet phase-space distribution, post-collision section.** Top: Free cooling after $n = 6$ collisions, i.e. with energy $E_{\mathrm{ini}} - n\epsilon = 15 - 6 = 9$. Bottom: Billiard dynamics without energy reduction on bridge rupture after $n = 6$ collisions at $E = 9$. The natural distribution slightly changes with energy. Consequently, the histogram obtained by keeping the energy constant is slightly sharper as the system has sufficient time to relax. Note that the similarity between the distributions independent of the initial conditions indicates that the distribution obtained is indeed the natural one. **Simulation details.** Resolution: $n_{\mathrm{bin}} = 1000 \times 1000$. $n_{\mathrm{bin}} \cdot 100$ initial conditions, randomly distributed. Further parameters as in Fig. 2.6.

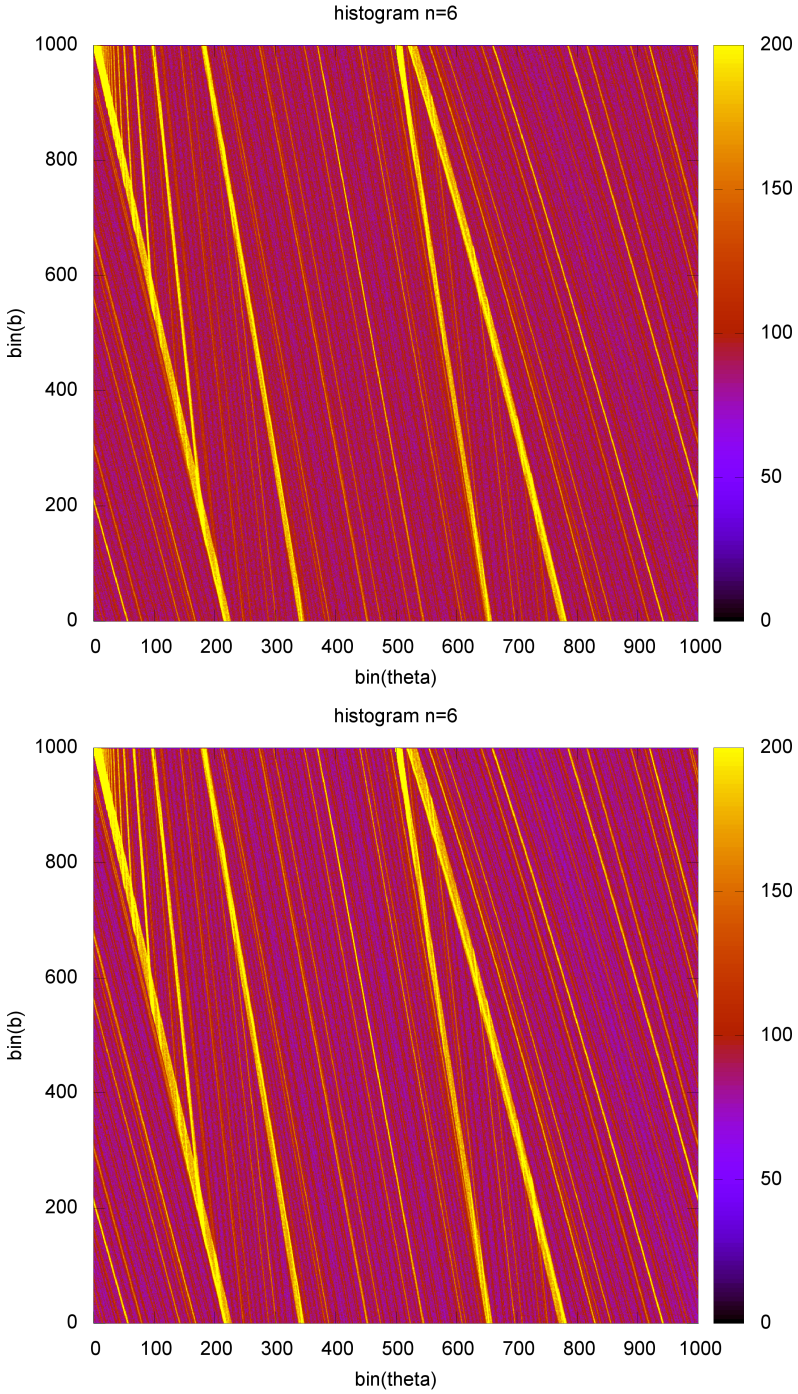

Figure 2.8: **Histograms of the symmetry-reduced wet phase-space distribution, pre-collision section.** Top: Free cooling. Bottom: Propagation without change of energy. Details see Figure 2.7.

2.3 Non-injectivity as origin of fractal structure

The fractal structure in the wet phase space is caused by a mechanism that is qualitatively different from the one in the dry case illustrated by the baker map (Fig. 2.1). Rather than variability of the phase-space compression rate the structure does not emerge from deficiency of phase volume but is due to a surplus of volume: The fractal structure emerging in the wet billiard dynamics mainly results from non-injective regions of the billiard map: Due to the direction dependence of the thin-thread model two trajectories – one colliding and one passing trajectory – evolve into a single one after a bridge rupture (see Fig. 2.9). This merging means that the point (b, θ) describing the final trajectory has two preimages (*2→1-mapping*). The regions in phase space resulting from such a double folding of phase space end up with higher density than the regions that are mapped bijectively. Iterative mapping and double folding eventually causes the fractal distribution. Note that in contrast to the distribution obtained in the dry case, which has a Cantor type support with box counting dimension $D_0 < 2$, the support of the natural distribution of the wet billiard fills the whole phase space so that $D_0 = 2$. The distribution is fractal in the sense that its information dimension D_1 is smaller than the box counting dimension of its support, $D_1 < D_0$ (for a detailed discussion see [TG06, Sec. 2.3]).

The 2→1-regions are characterized by the fact that the impact parameters $b < 1$ encountered after a collision are transformed by the bridge map to values $b' = \text{bridge}(b)$ that coincide with the values $b > 1$ of passing trajectories, that is:

$$|b'| > 1.$$

Using the bridge map Eq. 2.7 and recalling $b < 1$ the above condition gives the critical impact parameter for 2→1-mapping:

$$b_{2\to1} := \sqrt{1 - \frac{1}{E}} < |b| < 1.$$

At low kinetic energies a second effect characteristic to the wet granular matter occurs: clustering. The two interacting disks form a cluster if the radial part of the kinetic energy E_{rad} is smaller than the bridge rupture energy $\epsilon = 1$:

$$E_{\text{rad}} < 1.$$

With $E = E_{\text{rad}} + E_{\text{tan}} = E\cos^2\varphi + E\sin^2\varphi$, where φ denotes the angle between trajectory and surface normal (see Fig. 2.3) a critical impact parameter b_{c} is obtained above which clustering occurs (s_{c}: bridge-rupture distance):

$$1 > E\cos^2\varphi = E\left(1 - \frac{b^2}{(1+s_{\text{c}})^2}\right)$$
$$\Rightarrow b_{\text{c}} := (1+s_{\text{c}})\sqrt{1 - \frac{1}{E}} < |b| < 1.$$

If $b_{\text{c}} \geq 1$ no clustering occurs. From this condition the critical energy dividing the *clustering* and *pre-clustering regime* can be obtained:

$$b_{\text{c}}(E_{\text{c}}) = 1 \qquad \Rightarrow \qquad E_{\text{c}} = \left\lceil \frac{1}{1 - \frac{1}{(1+s_{\text{c}})^2}} \right\rceil. \tag{2.9}$$

The ceiling function is used because the energy decreases in portions of ϵ.

Figure 2.10 sketches the situation: 2→1-mapping occurs for all energies, clustering only in the low energy clustering regime, $E < E_c$. Both effects occur for large impact parameters $|b|$ and since $b_c/b_{2\to1} = 1 + s_c > 1$ the clustering region lies completely within the 2→1-region:

$$\begin{aligned} \textbf{2→1-mapping:} \quad & |b| \in [b_{2\to1}, 1] \\ \textbf{clustering:} \quad & |b| \in [b_c, 1] \end{aligned}$$

$$\sqrt{1 - \frac{1}{E}} = \qquad b_{2\to1} < b_c \qquad = (1 + s_c)\sqrt{1 - \frac{1}{E}}. \tag{2.10}$$

The clustering region is treated as an absorbing region in phase space and clustered trajectories are removed from the assembly. Thus, after the onset of clustering for $E < E_c$ the 2→1-effect is partially cancelled: Only the passing trajectory remains while the second one that has been subject to collision and bridge interaction is removed. In other words: The leak lies in the non-injective image region and it removes some trajectories corresponding to the collision and bridge rupture branch of the preimage.

Clustering alone would not produce phase space structure as it does not affect surjectivity: The bridge map (Eq. 2.7) uniformly expands the non-clustering part of phase space with $|b| \in [0, b_c]$ to the interval $[0, 1]$. Thus – eventually thanks to the conservation of angular momentum – the phase space of the Poincaré section at the next collision is completely covered by the image of the part of phase space remaining after the removal of bound states.

2.3.1 2→1-mapping

To check if phase-space structure is indeed caused by phase space folding due to 2→1-mapping as described in the previous section the following simulation is performed: An assembly is initialized with post-bridge impact-parameter values b' that lie within the bridge image of the 2→1-region (i.e. the assembly consists of closely passing trajectories),

$$|b| \in [b_{2\to1}, 1] \qquad \xrightarrow{\text{Eq. 2.7}} \qquad |b'| \in \left[1, \frac{1}{\sqrt{1 - \frac{1}{E}}}\right],$$

and propagated until the next collision to see what pattern the critical region takes in the collision section. Figure 2.11 shows that the resulting stripe pattern is just the first order pattern of the fractal structure. As pre-collision values are displayed instead of the post-collision ones, it is also possible to identify the geometric origin of the pattern.

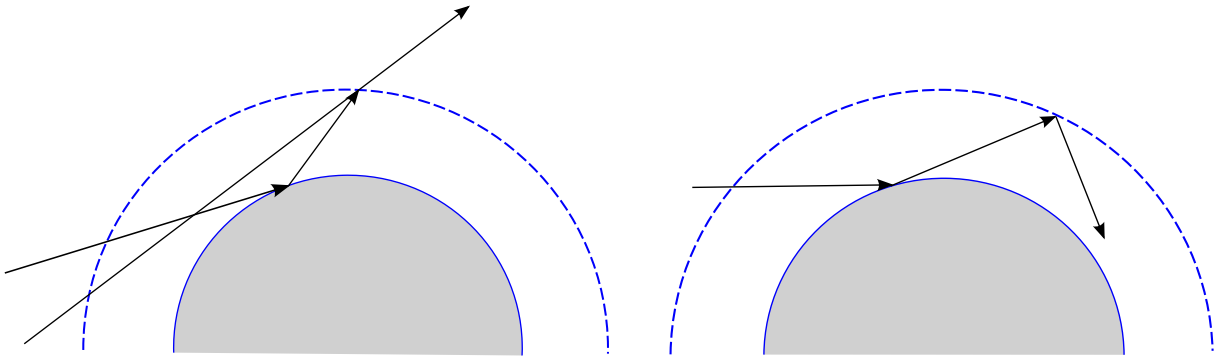

Figure 2.9: **2→1-mapping and clustering** are two effects characteristic to the thin-thread model that govern the fractal distributions on the phase space. 2→1-mapping (left) occurs for all energies, clustering (right) only in the low energy clustering regime. Both effects occur for large impact parameters $|b|$.

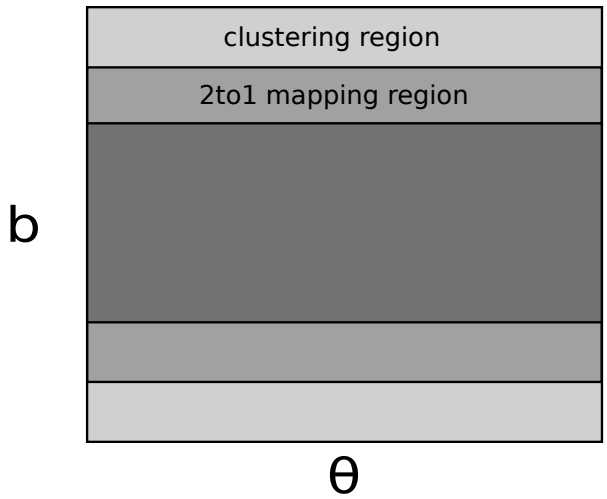

Figure 2.10: **Sketch of the 2→1-mapping and clustering region in (b, θ) space for low energies.** The clustering region lies within the 2→1-region so that their structure generating effects cancel out. Shown above are the positions of the regions in the collision section although 2→1-mapping and clustering actually become effective only later with bridge rupturing.

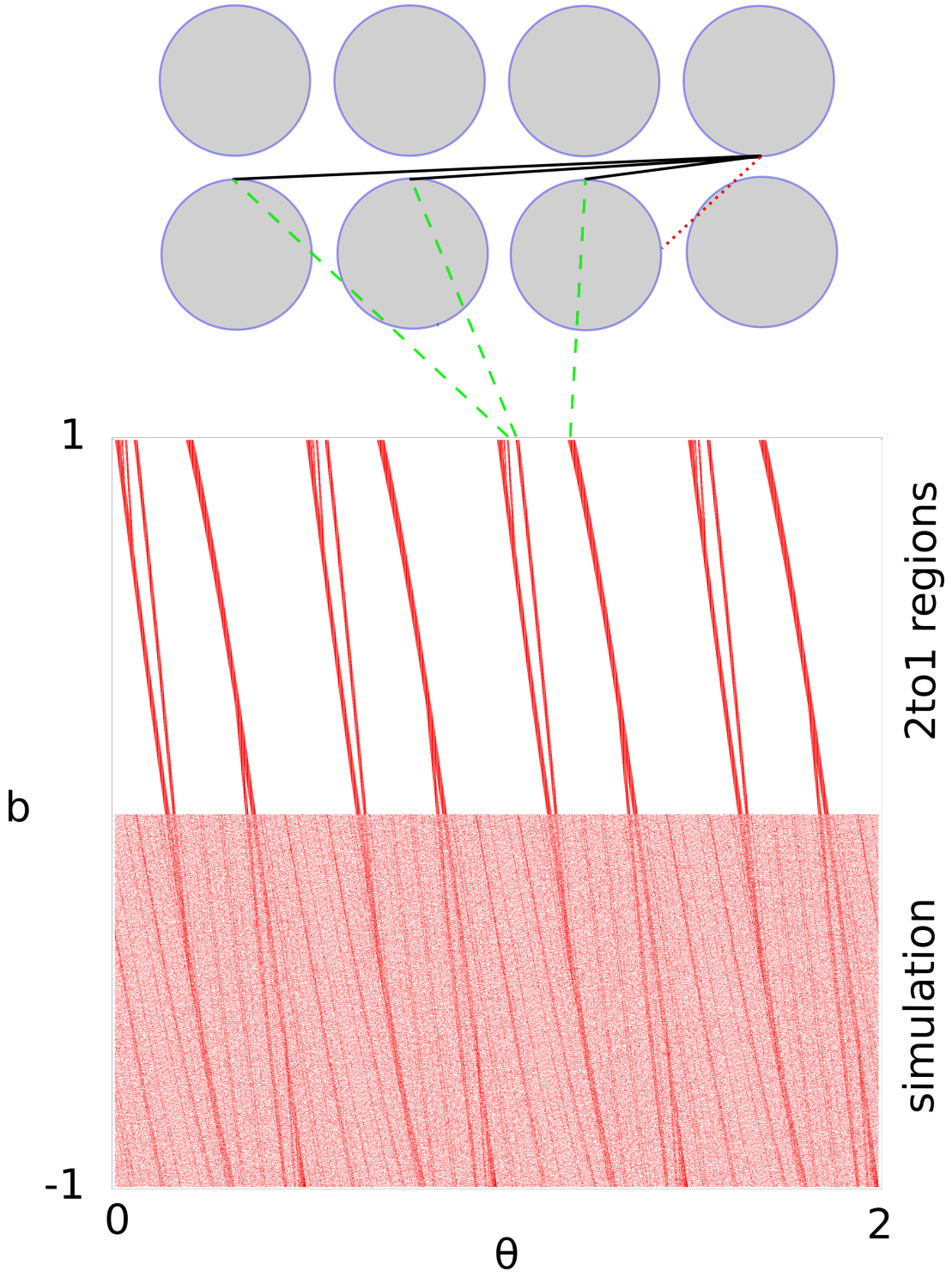

Figure 2.11: **The pre-collision density ("simulation") and the expected 2→1-region ("theory") match perfectly**. Depending on the angle the stripe pattern can be assigned to the geometrical structure. To additionally check whether the origin of the first order stripe pattern lies in the geometric arrangement of scatters the radius was chosen large enough to block the diagonal channels (red dotted line).

2.3.2 Interplay of 2→1-mapping and clustering

To examine whether the onset of clustering truly counteracts the 2→1-mapping we quantify the amount of phase-space structure by means of an *information entropy* (e.g. [Set07]),

$$\begin{aligned} S_\epsilon(n) &= -\frac{1}{\nu_{\text{bin}}} \sum_{i=1}^{\nu_{\text{bin}}} \rho_i \ln \rho_i \qquad \text{with} \qquad \rho_i = \frac{\nu_i(n)}{N(n)/\nu_{\text{bin}}} \\ &= -\sum_{i=1}^{\nu_{\text{bin}}} \frac{\nu_i(n)}{N(n)} \ln \left(\frac{\nu_i(n)}{N(n)} \nu_{\text{bin}} \right), \end{aligned}$$

where $N(n)$ is the number of assembly members after n collisions, $\nu_{\text{bin}} = \epsilon^{-1/2}$ the number of bins and $\nu_i(n)$ the number of assembly members in the ith bin at time n. The entropy is normalized such that it yields zero for a uniform distribution $\nu_i = N/\nu_{\text{bin}}$. Note that n corresponds to an energy E via Eq. 2.2. Having in mind Fig. 2.7 and 2.8 n has been chosen to simplify the simulation.

Figure 2.12 (top) shows simulation results for different ν_{bin}. The initial decrease of entropy can be assigned to the relaxation from the initial distribution towards the stripe pattern. In the consecutive pre-clustering regime the entropy decreases further, which indicates that the natural distribution belonging to the respective energy gradually show stronger structuring. Finally, with onset of clustering, the entropy apparently approaches a plateau. The entropy values, which reflect the amount of structure in the natural distribution at the given energy $E(n)$ (see Eq. 2.2), can be explained by the size of the 2→1-region belonging to E. In Fig. 2.12 (bottom) the width of the impact parameter ranges Δb obtained from Eq. 2.10 are plotted against energy:

$$\begin{aligned} \Delta b_{2\to1}\,(E > E_c) &= 1 - \sqrt{1 - \tfrac{1}{E}} \\ \Delta b_{2\to1}\,(E < E_c) &= L\sqrt{1 - \tfrac{1}{E}} \\ \Delta b_{\text{c}}\,(E < E_c) &= 1 - (1 + s_{\text{c}})\sqrt{1 - \tfrac{1}{E}}. \end{aligned}$$

The figure shows that in the pre-clustering regime the 2→1-region grows with n, explaining the decrease in entropy. In the clustering regime the clustering region emerges at expense of the effective 2→1-region and prevents a further decrease of entropy.

We do not further investigate the structure emerging in the phase space of the wet billiard as the basic principles were illustrated. Instead we concentrate on the clustering in the following section. However, we like to mention further steps to model the fractal structure: Based on a simple overlapping baker map (cf. Fig. 2.1) with a compression factor $c > 1/2$ it should be possible to estimate the information dimension of the structure along the lines of [TG06, Problem 2.16]. Numerically the information dimension can be determined from the information entropy (cf. [MTV04, Eq. 10]).

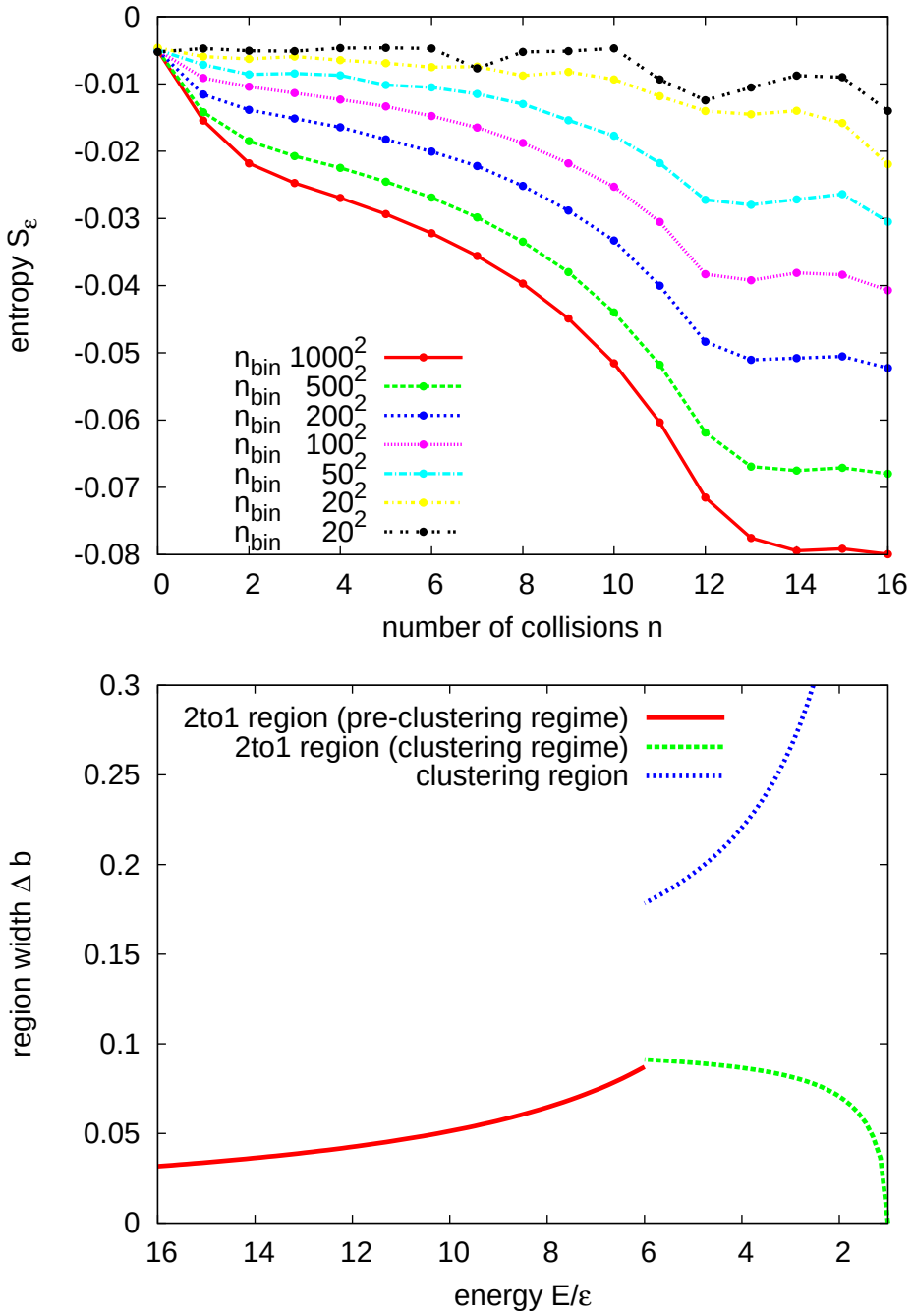

Figure 2.12: **Amount of structure in the natural distribution as quantified by the information entropy S_ϵ.** The entropy shows differences before and after onset of clustering. **Pre-Clustering:** The 2→1-region grows with n. As the amount of structure increases the entropy decreases. **Clustering:** The clustering region increases at the expense of the effective 2→1-region and prevents a further decrease of entropy. Note that the n- and E-axis correspond to each other.

2.4 Clustering

Despite of all the phase-space structure that was in detail explained in the previous sections a uniform distribution is still a sufficiently good approximation when deriving less microscopic properties of the dynamics. In particular, projecting the phase space distribution onto the coordinate axes, i.e. marginalizing one coordinate, yields uniform distributions (cf. Appendix B.1). This indicates, in particular, that for a many-particle system no structure remains in the few-particle distribution function on which kinetic theories basically rely [Rei98, Sec. S6.A].

As a demonstration and application of this fact we will in the following study the probability of a the two-disks gas to be clustered after n collisions if started with a random initial condition. Figure 2.13 (red dots) shows simulation results for this *survival probability* $P(n)$ that were obtained from the remaining number of unclustered states $N(n)$ out of a set of $N(0)$ trajectories with different initial conditions:

$$P(n) = \frac{N(n)}{N(0)}.$$

In the pre-clustering regime, i. e. for energies larger than the critical energy, $E > E_c$ (see Eq. 2.9), no clustering can occur so that $P(E) = 1$. For $E < E_c$ in the clustering regime the survival probability rapidly decreases with decreasing energy. If the remaining energy is smaller than the bridge rupture energy, $E < \epsilon$, there are no more free states.

Following section 2.1.3 the number of the clustering phase states per collision, i.e. the clustering probability $P(\text{cluster}|E)$ per collision and thus the clustering or escape rate κ is determined by the natural measure of the clustering region (cf. Eq. 2.10)

$$(\theta, b) \in [0, 2\pi] \times ([-1, -b_c(E)] \cup [b_c(E), 1]).$$

As the clustering region does not depend on the angle θ effectively only the projection of the phase space distribution onto the b-axis is needed. As this projection is a uniform distribution (cf. B.1), the energy dependent clustering rate is given by

$$\kappa(E) = P(\text{cluster}|E) = \begin{cases} 1 & \text{if } E < 1 \\ 1 - (1 + s_c)\sqrt{1 - \frac{1}{E}} & \text{if } 1 < E < E_c \\ 0 & \text{else} \end{cases}. \tag{2.11}$$

The number of unclustered states $N(n) = N(0)P(n)$ is consequently determined by the expression

$$\partial_n N = -\kappa(E) \cdot N.$$

The clustering rate depends on E and via Eq. 2.2 on n so that with $E_c = E(n_c)$ the clustering rate in the non-trivial regime $n_c < n < E_{\text{ini}}$ takes the form

$$\kappa(E(n)) = 1 - (1 + s_c)\sqrt{1 - \frac{1}{E_c - (n - n_c)}}.$$

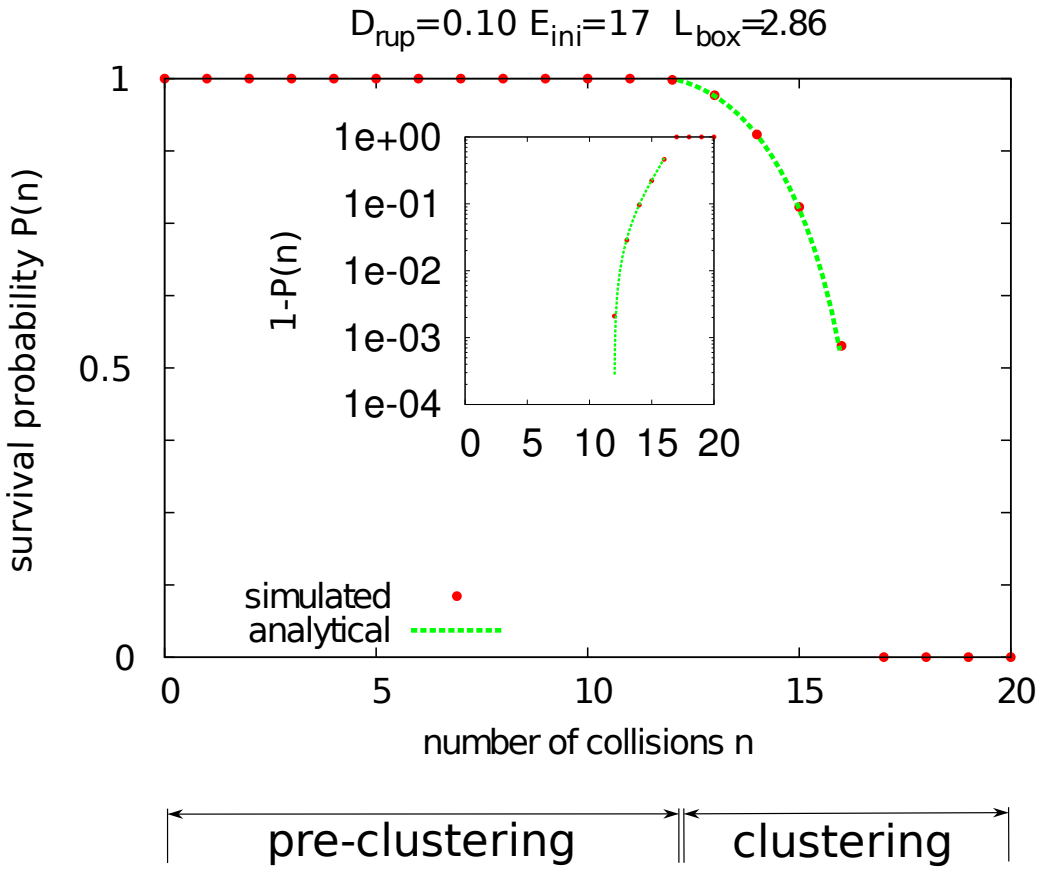

Figure 2.13: **Survival probability as function of number of collisions.** Recall that the number of collisions n corresponds to an energy $E(n)$. The plot thus shows the probability $P(E)$ for a system with an arbitrary initial condition and energy E not to cluster. The simulation data and analytical prediction (see main text) fit perfectly. Note that from Eq. 2.9 and the given parameters $E_c = 6$ so that clustering is from Eq. 2.2 expected to start at $n_c = 12$. This is indeed observed (see inset).

The resulting differential equation is found to be solved by

$$N(n+n_c) = N_0 \exp\left(\int_0^n \kappa(n')\,\mathrm{d}n'\right)$$
$$= N_0 \frac{\exp\left\{-n-(1+L)\left[\sqrt{(E_c-n)(E_c-n-1)}+\ln\left(\sqrt{E_c-n}+\sqrt{E_c-n-1}\right)\right]\right\}}{\exp\left\{-(1+L)\left[\sqrt{E_c(E_c-1)}+(1+L)\ln\left(\sqrt{E_c}+\sqrt{E_c-1}\right)\right]\right\}},$$

where the integral was evaluated using MATHEMATICA. Consequently, the freely-cooling wet billiard is expected to show an exponential-type escape of trajectories as expected for a strongly chaotic system. However, the energy dependence of the leak causes a rather complicated exponent. Figure 2.13 (green line) shows that the simulation results are well met. The clustering example discussed thus illustrates that assuming a uniform phase space distribution remains a valid approximation for wet particles.

2.5 Side note: Thick-film model

The 2→1-mapping of the thin-thread model is a feature not necessarily resulting from a hysteretic interaction. It is therefore interesting to take a brief look at the thick-film variant of the wet interaction (see section 1.1.3), which is hysteretic and everywhere bijective. The possible sequence of events is altered as compared to the thin-film wet billiard (cf. section 3.1.1):

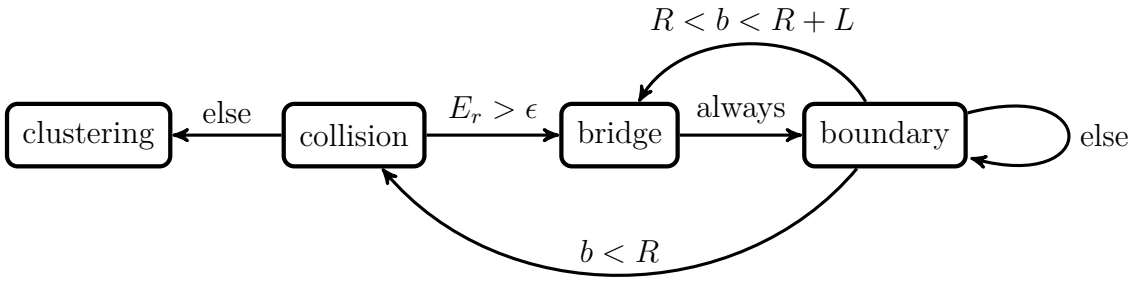

As dissipation happens upon bridge rupture the Poincaré section has to be placed pre-bridge rather than post-collision to have a section of constant energy. Consequently, the phase space spans an interval $[-(R+s_c), R+s_c]$. Furthermore, there is no critical energy E_c (see section 2.3) above which clustering is absent: If the particle touches the liquid film tangentially with zero radial energy it will cluster irrespective of the absolute energy. The probability to cluster, however, decreases with increasing energy and is in line with Eq. 2.10 given by ($R = 1$):

$$P(\text{cluster}|E) = \begin{cases} 1 & \text{if } E < 1 \\ 1 - \frac{b_c(E)}{1+s_c} = 1 - \sqrt{1 - \frac{1}{E}} & \text{else} \end{cases} \tag{2.12}$$

Without the 2→1-mapping and as clustering itself will not produce phase space structure (see section 2.3), the thick-film billiard is expected to have a uniform phase space distribution. This is not the case: Figure 2.14 demonstrates that for the freely-cooling thick-film billiard some slight stripes are visible in the phase space distribution. For unclear reasons the structure vanishes if the energy is not reduced on bridge rupture. Thus, the natural distribution of the thick film billiard remains unclear. Preliminary observations (not shown here) indicate that the stripe pattern is independent of the system energy. This suggests that subtle geometric effects play a role in explaining the phase space of the thick-film billiard.

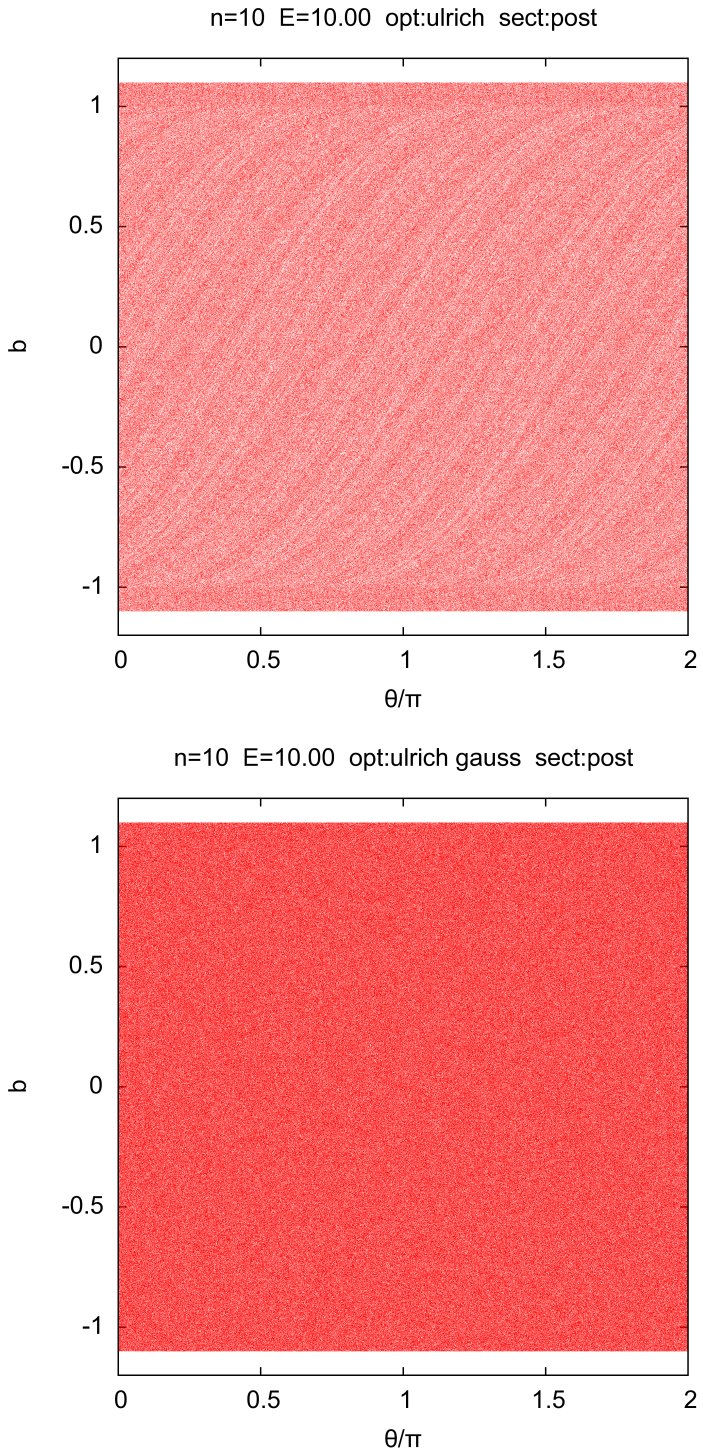

Figure 2.14: **Scatter plots of the thick-film phase space.** The phase space distribution of the freely-cooling thick-film billiard shows structure (top). When the energy is not reduced on bridge rupture, however, the structure vanishes (bottom). Note that the missing structure in the bottom scatter plot is not caused by too many points; structure remains absent for fewer points. **Key to the captions.** See Fig. 2.6

Chapter 3

Sheared wet billiard

As a dissipative system with no dynamic but only the static two-particle cluster as an equilibrium state the wet billiard (and granular matter in general) is studied as non-equilibrium system. Free cooling as studied in the previous chapter corresponds to a steady decrease of energy. Nevertheless, the accessible energy surface as support of the natural distribution is controlled by the Poincaré section (Sec. 2.1.1) in this setting.

In the present chapter dissipation caused by the liquid bridges will be contrasted with an energy input to the billiard system. Shearing is chosen as a driving mechanism for reasons already discussed (Sec. 1). Although the energy input due to shear prevents the collision-Poincaré section from being a section of constant energy a steady state situation with a fixed (average) energy would offer another mechanism to control the energy coordinate. For the combination of Lees-Edwards boundary conditions and wet granular matter it is however still an open question under what conditions steady states occur (cf. Sec. 1.1.4). Next to further exploring the phase space of wet granular matter in a driven situation the sheared Sinai billiard in its minimality thus seems a good setup to explore the question when and why steady states might occur in sheared wet granular matter.

Eventually, it is not obvious whether clustering still occurs in the sheared billiard. To probe natural distributions it would on the one hand be convenient to suppress clustering. On the other hand, clustering in the sheared billiard might result in an interesting example of transient chaos.

3.1 The system

Shearing as implemented by Lees-Edwards boundary conditions (Sec. 1.1.4) only affects the latter but leaves the other events, i.e. collision and bridge rupture unchanged. Instead of static periodic images the periodic images at the two Lees-Edwards boundaries of the billiard box parallel to the shear layer are taken to be moving with a shear speed s (Fig. 3.1). Crossing a Lees-Edwards boundary thus means a coordinate transformation into a moving frame of reference and results in a change of velocity. The shearing motion introduces a direct time-dependence into the billiard dynamics. Nevertheless it is still convenient to maintain the post/pre-collision Poincaré section and the number of collisions as resulting evolution variable: Unnaturally high weighting of long collision-free flights that arises from the unavoidably infinite horizon of the shearing geometry is thus

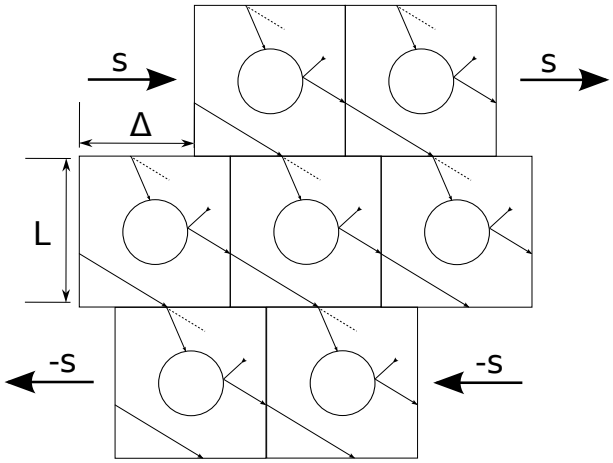

Figure 3.1: **Sinai billiard with Lees-Edwards boundary conditions.** The periodic images attached to top and bottom move with shear speed s. When crossing the Lees-Edwards boundary the trajectory is thus transformed to a moving frame of reference. This results in a change of the velocity component parallel to the direction of shear.

prevented. The real time t is accounted for by an additional phase-space dimension.

Mapping. Performing a boundary crossing according to Lees-Edwards boundary conditions only affects the velocity component parallel to the boundary and leaves the perpendicular one unchanged. Lees-Edwards boundary conditions are thus a concept that is easier described in cartesian coordinates than in the (b, θ, E)-coordinates used so far. To be able to compare to the previous results it is nevertheless convenient to have a description of Lees-Edwards boundary conditions in those coordinates. We will obtain this description by formulating Lees-Edwards boundary conditions in Cartesian coordinates and then perform a transformation of coordinates. As Lees-Edwards boundary conditions affect the speed $v = |v| = \sqrt{2E}$ we will use v or E equivalently in this chapter, starting with v in the following derivation. To avoid confusion we recall that the sheared billiard is symmetric with respect to π-rotation (see Fig. 3.1) and restrict this derivation to $\theta \in [0, \pi]$ and positive shear speed $s > 0$.

The sheared billiard dynamics still consists of line segments (Fig. 3.1). As described in Sec. 2.1.1 the direction is given by θ while $b = I/|v|$ defines its position with respect to the origin. From a "Cartesian" viewpoint $|v|$ and θ are the polar representation of a velocity vector $\vec{v} = (v_x, v_y)$. They define the slope of the trajectory while b is related to the axis intercept Δ_x (Fig. 3.2, left). Transforming between these representations of the trajectory segments is possible by means of

$$\mathrm{T}\left(\theta, b, v\right) = \left(v_x, v_y, \Delta_x\right) = \left(v\cos\theta, v\sin\theta, \frac{b}{\sin\theta}\right)$$

$$\mathrm{T}^{-1}\left(v_x, v_y, \Delta_x\right) = \left(\theta, b, v\right) = \left(\operatorname{atan}\left(\frac{v_y}{v_x}\right), \Delta_x \sin\left[\operatorname{atan}\left(\frac{v_y}{v_x}\right)\right], \sqrt{v_x^2 + v_y^2}\right).$$

To derive the Lees-Edwards-boundary-map we describe the line segments constituting the billiard dynamics as (Fig. 3.2, left)

$$x\left(y\right) = \Delta x + y\frac{v_x}{v_y}.$$

Crossing the Lees-Edwards boundary corresponds to a coordinate transformation into a new frame of reference moving with velocity $\vec{s} = (s, 0)$. The centers $\vec{O}(t) = (O_x(t), L)$ of the top row boxes (with respect to the old origin) are displaced as

$$O_x(t) = O_x(0) + st = zL + st, \qquad z \in \mathbb{Z},$$

where the boxes are assumed to be aligned to the center row at time $t = 0$. Note that at this point "real" time as opposed to the number of collisions n that served as time-variable so far is introduced to the sheared billiard. At the Lees-Edwards boundary one of the two adjacent boxes will be entered. Which of the two depends on the x-coordinate of the crossing point, $x_c := x(y = L/2)$, so that the x-coordinate of the new origin, $\Delta O_x(t)$, is determined from

$$\Delta O_x(t) = \begin{cases} (st \bmod L) & \text{if } |x_c - (st \bmod L)| < \frac{L}{2} \\ (st \bmod L) - \operatorname{sgn}(s)\, L & \text{else} \end{cases}. \tag{3.1}$$

Using this and Fig. 3.2 (right) to illustrate the new representation of Δ_x, the coordinates the Lees-Edwards boundary boundary map is given by

$$\mathrm{LE}|_{\Delta O_x(t_b)}(v_x, v_y, \Delta_x) = \left(v_x - s, v_y, \Delta_x + \frac{L}{2}\left(\frac{v_x}{v_y} + \frac{v_x - s}{v_y}\right) - \Delta O_x(t_b)\right).$$

Applying this transformation to the Lees-Edwards-boundary map L yields the desired formulation:

$$\begin{aligned} &(\theta, b, v) \mapsto \mathrm{T}^{-1} \cdot \mathrm{LE}|_{\Delta O_x(t_b)} \cdot \mathrm{T}(\theta, b, v) \qquad (3.2) \\ &= \left(\theta', \sin\theta' \left[\frac{b}{\sin\theta} - \Delta O_x(t_b) + \frac{L}{2}\left(\frac{1}{\tan\theta} + \frac{1}{\tan\theta'}\right)\right], \sqrt{(v\sin\theta)^2 + (v\cos\theta - s)^2}\right), \end{aligned}$$

where $\Delta O_x(t_b)$ as in Eq. 3.1 and

$$\theta' = \arctan\left(\frac{v\sin\theta}{v\cos\theta - s}\right).$$

The boundary map derived only applies for the two sides of the square billiard box that are parallel to the shearing motion. For the remaining two sides the boundary conditions of the sheared billiard are completed by plain periodic boundary conditions (Eq. 2.5).

Phase space. The sheared billiard has a four-dimensional phase space: As the post/pre-collision Poincaré section no longer coincides with a section of constant energy the latter emerges as a 3rd nontrivial coordinate besides (θ, b). The fourth dimension is due to the *phase* $\Delta := \Delta O_x(t_b)$, i.e. the offset of the moving Lees-Edwards box that corresponds to the real time or to the total distance a particles has travelled. The phase space

$$(\theta, b, E, \Delta) \in [0, 2\pi] \times [-R, R] \times \mathbb{R} \times \left[-\tfrac{L}{2}, \tfrac{L}{2}\right] \tag{3.3}$$

is bounded in θ, b and Δ direction while the energy is not a priori limited. Under what conditions the energy increases, decreases or finds a steady-state will have to be evaluated.

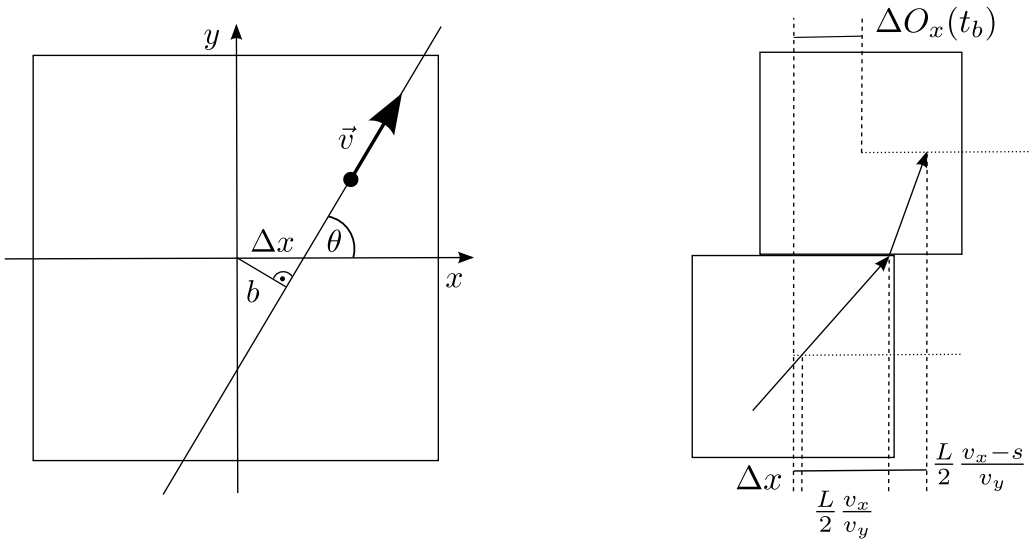

Figure 3.2: **Sketches to illustrate Lees-Edwards-boundary mapping.** Left: A trajectory segment is equivalently described by an angle θ and the impact parameter b or by the velocity vector $\vec{v} = (v_x, v_y)$ and an axis intercept Δx. Right: Crossing the Lees-Edwards boundary means a coordinate transformation into a new reference system moving with velocity $\vec{s} = (s, 0)$. The sketch illustrates how the axis intercept Δx transforms. It is a snapshot at the time of boundary crossing t_b, i.e. the position of the new origin is depicted at that time: $\Delta O_x = \Delta O_x(t_b)$.

3.1.1 Implementation

The implementation of the sheared billiard emerges from the simple billiard (Sec. 2.1.2) by expanding the boundary. With "LE boundary" denoting a Lees-Edwards boundary crossing and "simple boundary" a crossing of the remaining two simple periodic boundaries the sequence-of-events diagram looks as follows:

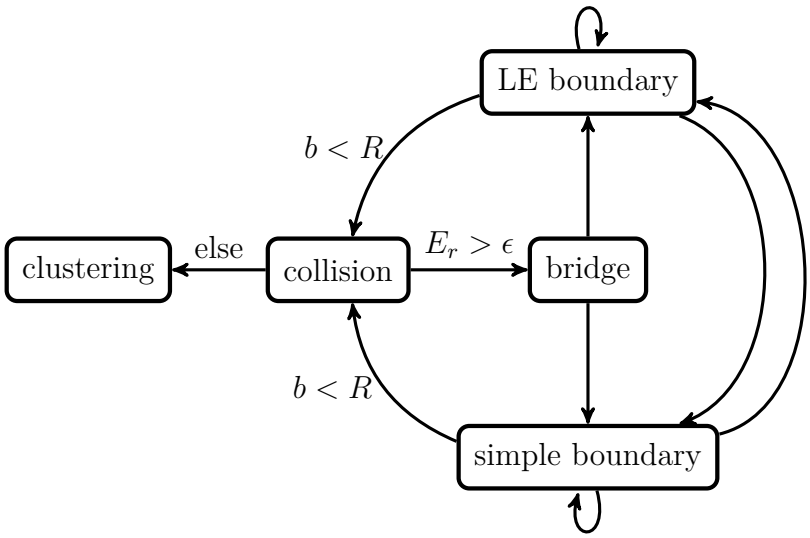

Due to the additional phase space variables a state is now determined by a the four-tuple as in Eq. 3.3. In the simulations the real time t is used instead of the phase Δ. As for the simple billiard, type and details of the boundaries are determined by the coordinates.

Also, for the thick-film billiard additional direct transitions from the boundaries to the bridge without interjacent collision are again possible.

3.2 Observations

We start the discussion of the sheared wet billiard by presenting the numeric observations. Before discussing the phase space distribution, it is however at place to trace the setting and to show that this phase space is unbound on the "new" energy axis and that clustering remains possible. To place the results obtained for the thin-film sheared billiard, we will contrast them with the sheared billiards with thin-film, elastic and inelastic interaction. When referring to "the wet billiards" common results for the thin-film and thick-film billiards are meant.

3.2.1 Acceleration vs. lifetimes

This section is concerned with the average energy $\langle E \rangle$ of the sheared billiards. The average is taken over an assembly of systems with different initial conditions and only systems that are not in the clustered state are taken into account. Figures 3.3 to 3.6 show the numerical results for the sheared systems with thin-film, thick-film, elastic and inelastic collisions. We point out the following key observations and questions resulting for the wet sheared billiard that will be explained in the following sections:

- In contrast to the sheared dry case the sheared wet billiard has no stable steady state (Figs. 3.3, 3.4 and 3.6, top). What difference between the inelastic and wet dissipation causes this?
- There are two time regimes in which $\langle E \rangle$ is a linear function of the number of collisions n (Figs. 3.3, 3.4 and 3.6, bottom). Is some kind of relaxation into an asymptotic state taking place despite of the changing energy? Why does this effect not occur in the elastic sheared billiard (Fig. 3.5)?
- For the wet billiards the energy initially increases for shear speeds larger than a critical shear speed, $s > s_c^0$ and decreases for $s < s_c^0 \approx \sqrt{2}$ (Figs. 3.3 and 3.4). What determines s_c^0?
- With growing n the energy starts increasing even for $s < s_c^0$ (Fig. 3.3 and 3.4). Why?

The sheared wet billiard constitutes a billiard system whose boundaries are moving (periodically) in time: Instead of performing the change of coordinate system at the time t_b of boundary crossing (cf. Fig. 3.2, right) it could equivalently be performed together with the collision. On collision the point particle may then be accelerated (if the boundary moves towards it) or decelerated (if the boundary retreats). A possibly occurring net acceleration is called *Fermi acceleration* after an idea of Enrico Fermi to explain the acceleration of charged particles that collide with chaotically moving magnetic clouds. The hypothesis currently under investigation is that a billiard geometry that is chaotic if the boundaries are not moving will show Fermi acceleration for moving boundaries, and an

important open question in this field is to explore how the acceleration is related to the properties of billiards and its chaotic dynamics. For further discussion see e.g. [Los07] and references therein. This background adds the following item:

- The sheared billiards experience Fermi acceleration. How can the observations and explanations be placed into this field of research?

Similar to the non-sheared billiard (Sec. 2.4), clustering is still observed when applying Lees-Edwards boundary conditions. How is the occurrence of clustering, however, influenced by the increasing $\langle E \rangle$? We find (Figs. 3.7 to 3.9):

- High average energies do not prevent clustering. This indicates a broad energy distribution that always covers low energies (Fig. 3.7). On the other hand the clustering region should affect the energy distribution. How are energy distribution and clustering interrelated?

- The lifetime distribution decays with a power-law tail (Figs. 3.8 and 3.9). In view of Sec. 2.1.3 this an unexpected observation. What causes the power-law? What determines the exponent?

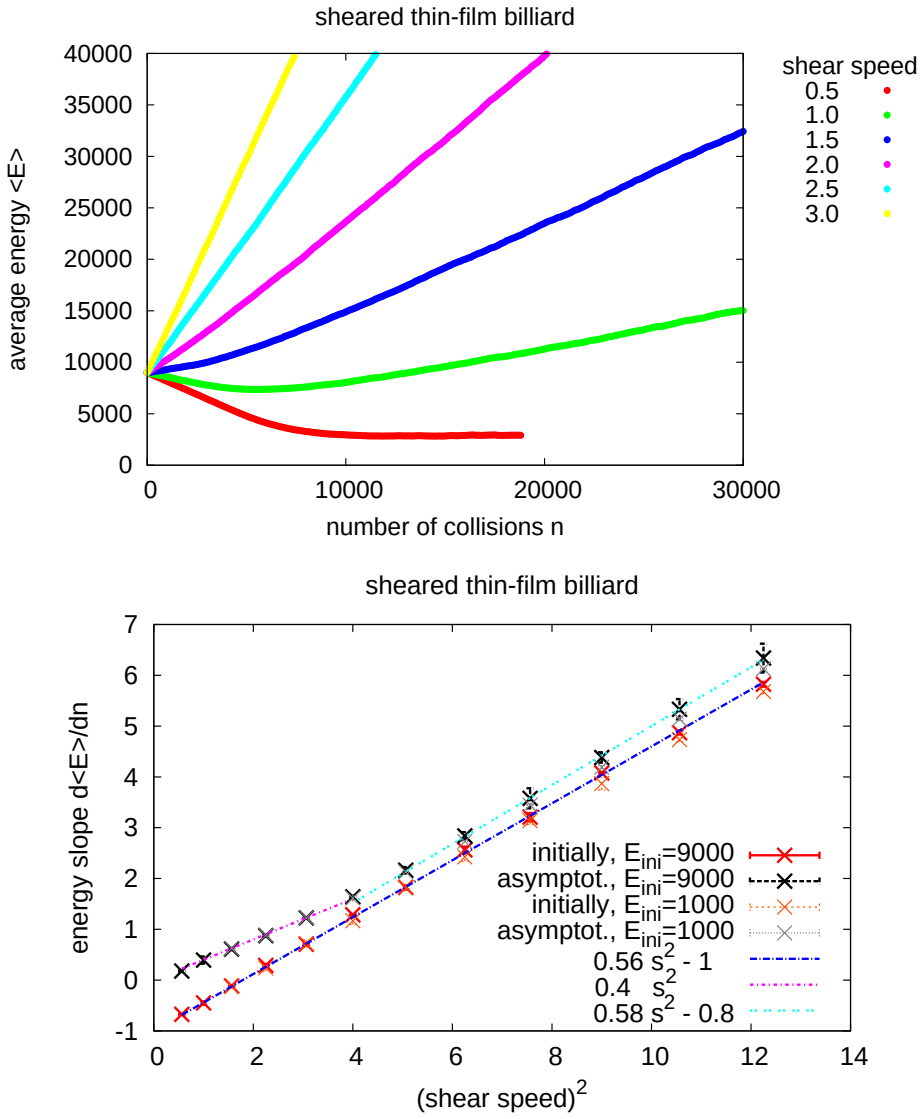

Figure 3.3: **Sheared thin-film billiard: Average energy.** The ensemble average of the system energy $\langle E\rangle$ does not relax to a steady-state value (top). Two regimes in which $\langle E\rangle$ is a linear function of the number of collisions n are identified. The slopes $\mathrm{d}\langle E\rangle/\mathrm{d}n$ are proportional to the shear speed s (bottom). Initially it is $\langle E\rangle \propto (s^2/2-1)$, i.e. there is critical shear speed $s_c^0 \approx \sqrt{2}$ so that $\langle E\rangle$ decreases for $s < s_c^0$ and increases for $s > s_c^0$. For larger n, $\langle E\rangle$ grows even for $s < s_c^0$ (The phase space plots Figs. B.6 to B.8 confirm that this is a typical behavior and not caused by remaining atypical trajectories). For the slope $\mathrm{d}\langle E\rangle/\mathrm{d}n \sim s^2$ remains but the exact form splits up into two regimes. These are not exactly separated by s_c^0 but rather by $s_c^\infty = 2$. The results appear independent of the initial energy $\langle E_{\mathrm{ini}}\rangle$. **Simulation details.** Average over non-clustered out of $3 \cdot 10^4$ initial conditions, initial energy constant $E_{\mathrm{ini}} = 1000$ or uniformly distributed in $[7000, 11000]$ (due to high energies the latter not expected to differ much from isoenergetic case), $n_{\max} = 5 \cdot 10^6$ and $n_{\max} = 3 \cdot 10^4$ steps, respectively. To keep statistical errors small all data points displayed are averaged over at least 1000 trajectories. The uncertainty expressed by the error bars is dominated by the variability due to different fitting intervals for the energy slope. Apart from mentioned, default parameters were used (cf. Appendix A).

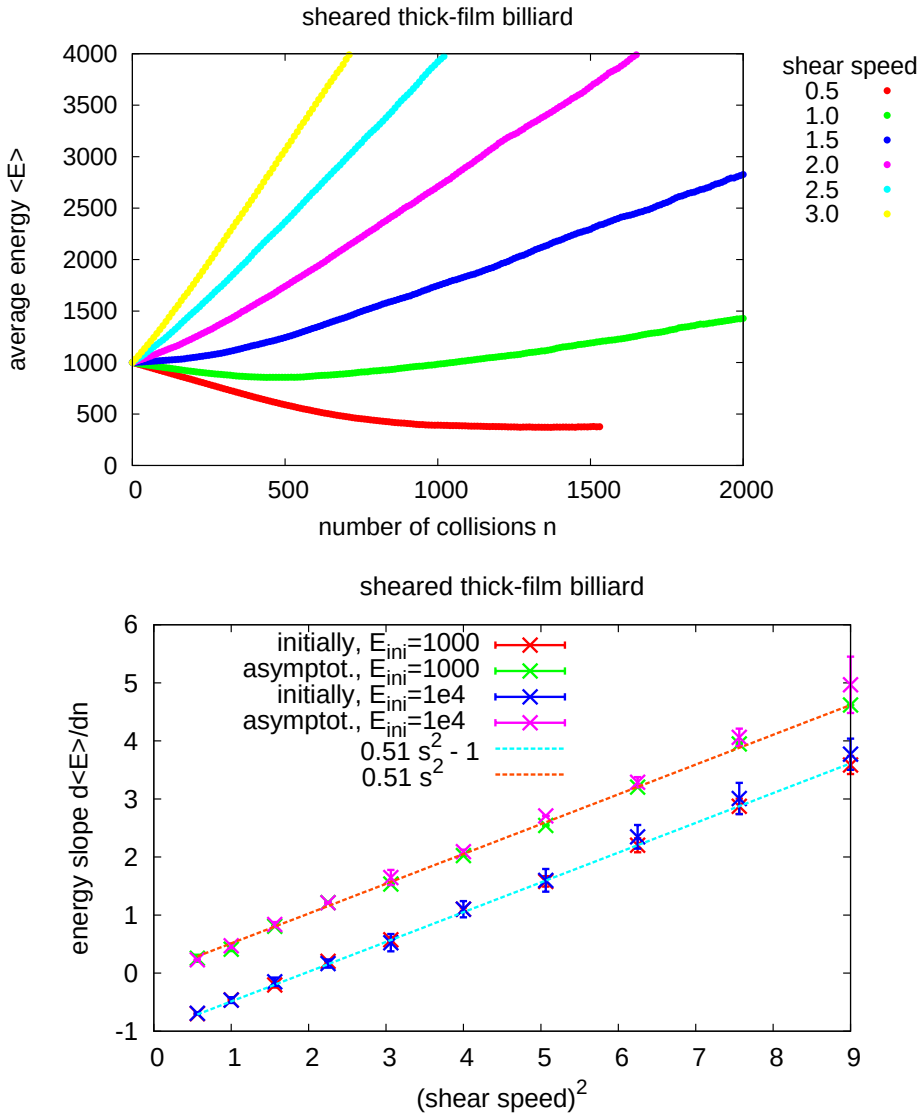

Figure 3.4: **Sheared thick-film billiard: Average energy.** Like the thin-film billiard (Fig. 3.3) the thick-film billiard has no stable steady states but shows two regimes of linear dependence $\langle E\rangle\,(n)$ (top). The initial slopes are essentially as described for the thin-film billiard (bottom). For large n, however, the situation appears to be simpler: $\mathrm{d}\langle E\rangle/\mathrm{d}n \approx s^2/2$ uniformly for large and small s. Again the results appear more or less independent of the initial energy $\langle E_{\mathrm{ini}}\rangle$ and the uncertainty expressed by the error bars are obtained by different fitting intervals for the energy slope. **Simulation details.** Average over remaining non-clustered systems out of $3 \cdot 10^4$ and $2 \cdot 10^4$ initial conditions, respectively, with initial energy $E_{\mathrm{ini}} = 1000$ and 10^4, $n_{\max} = 10^4$ and $2 \cdot 10^6$ steps, respectively. To keep statistical errors small all data points displayed are averaged over at least 1000 trajectories with different initial conditions. Apart from mentioned, default parameters were used (cf. Appendix A).

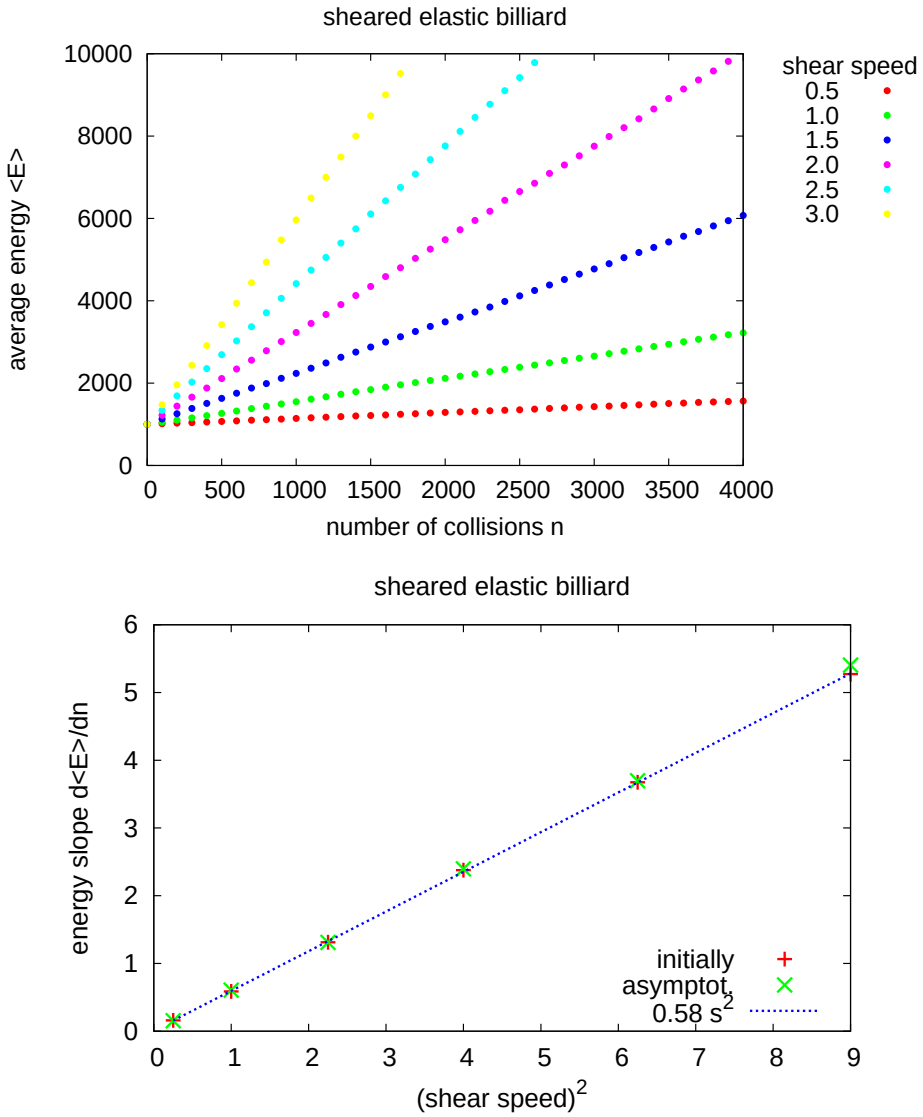

Figure 3.5: **Sheared elastic billiard: Average energy.** Due to the absence of dissipation energy input from shearing always heats up the system (top). The average energy linearly increases proportional to the square of the shear speed, $\langle E \rangle = 0.58 \cdot s^2 \cdot n$ (bottom). As for the wet billiards (Figs. 3.3 and 3.4) this seems reasonable because $s^2/2$ is the average energy input from the Lees-Edwards boundary conditions. The proportionality constant 0.58 coincides with the one found in the large-n regime of thin-film billiard. **Simulation details.** Average over 10^4 isoenergetic initial distribution with $E_{\mathrm{ini}} = 1000$, $n_{\max} = 10^4$ steps. Apart from mentioned, default parameters were used (cf. Appendix A).

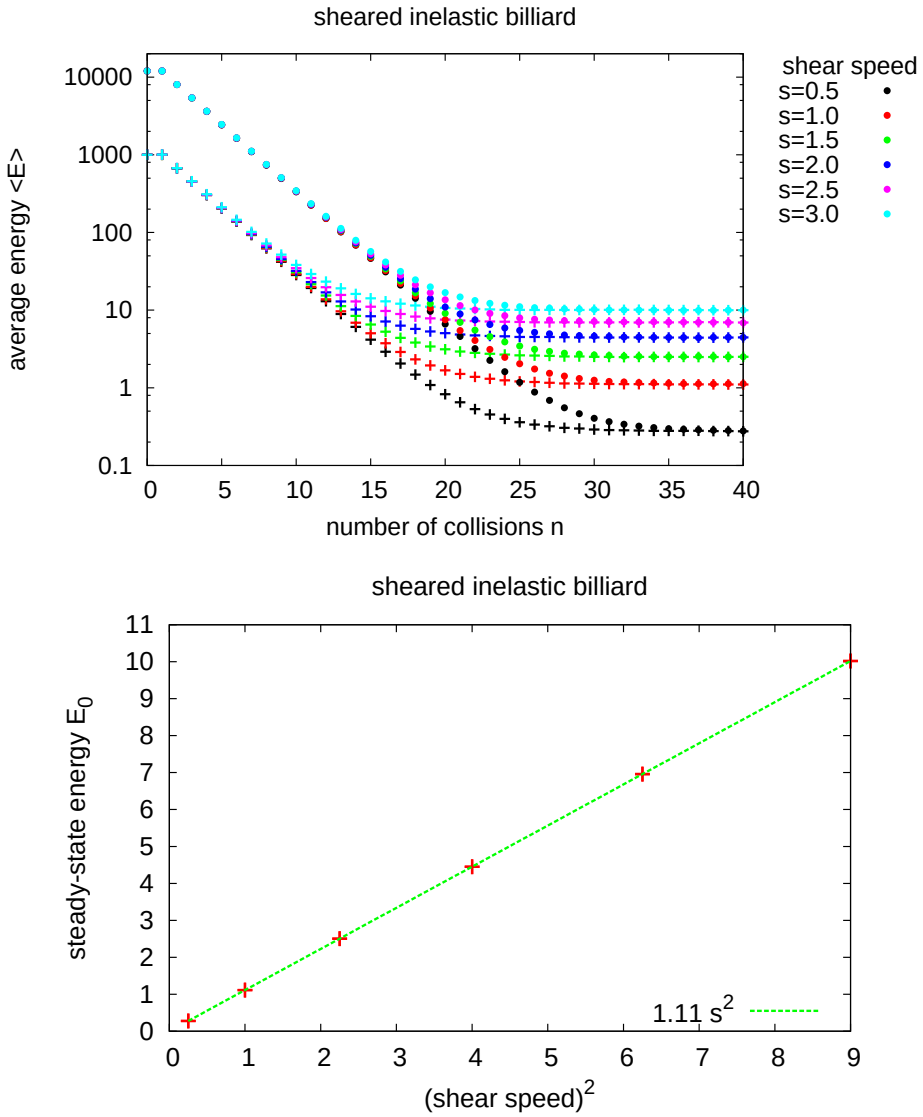

Figure 3.6: **Sheared inelastic billiard: Average energy.** The average energy $\langle E \rangle$ of the inelastic billiard quickly approaches a steady state (top). The steady-state energy value appears independent of the initial energy and proportional to the shear speed s^2 (bottom). **Simulation details.** Average over $2 \cdot 10^4$ initial conditions with initial energy $E_{\text{ini}} = \{1000, 12000\}$, $n_{\max} = 1000$ and 10^4, respectively, coefficient of normal restitution $\alpha = 0.5$. Apart from mentioned, default parameters were used (cf. Appendix A).

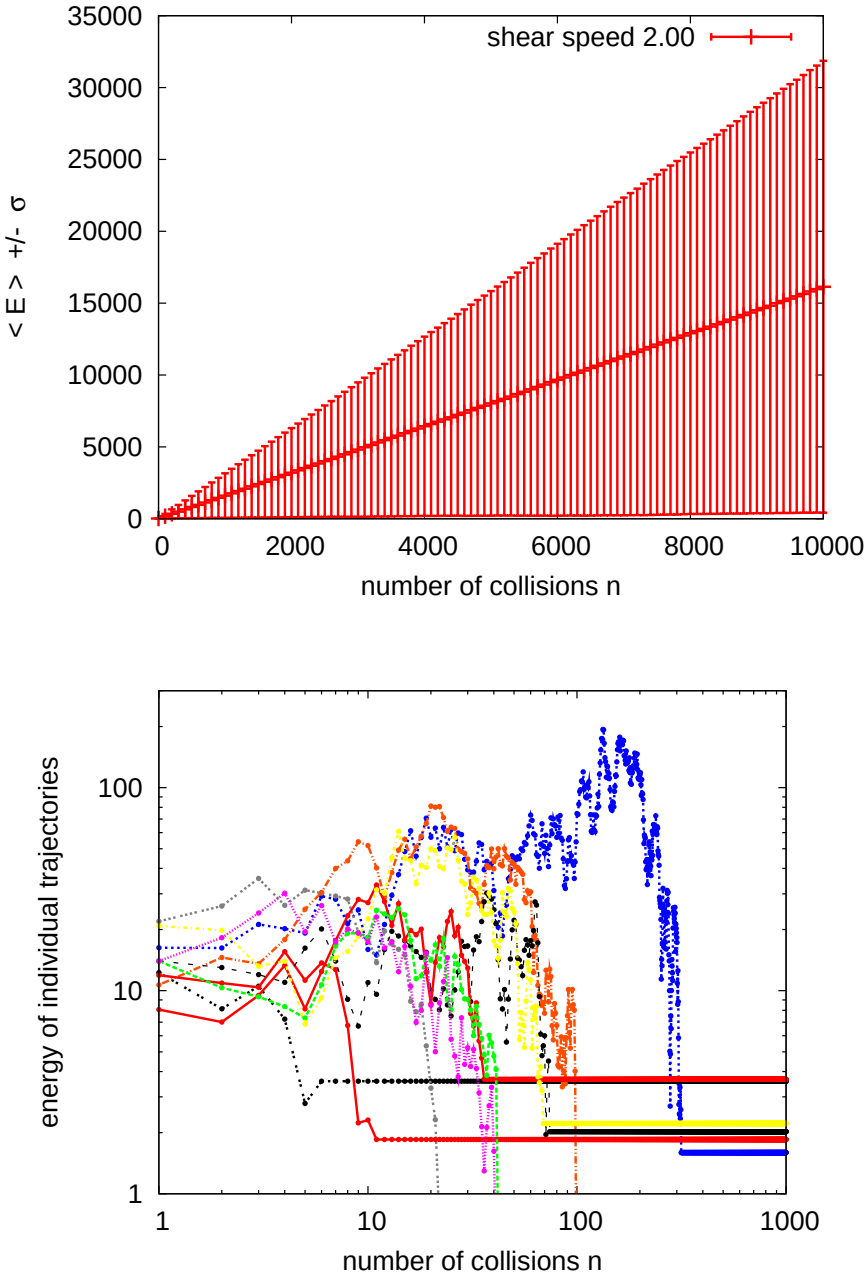

Figure 3.7: **Clustering despite of acceleration for the thin-film billiard.** For broad energy distributions that always cover very low energies clustering is possible despite of very high average energies. The top figure indicates a standard deviation σ linearly growing with the average energy $\langle E \rangle$ and illustrates variability within the assembly. As to be expected for (quasi-) ergodic dynamics, the large energy fluctuations can also be observed over time as the bottom figure showing energy trajectories for individual thin-film billiards depicts. For all systems the horizontal lines that are eventually encountered for large n amount to clustered systems with remaining energy $E < E_c$, where E_c is the critical energy from Eq. 2.9.

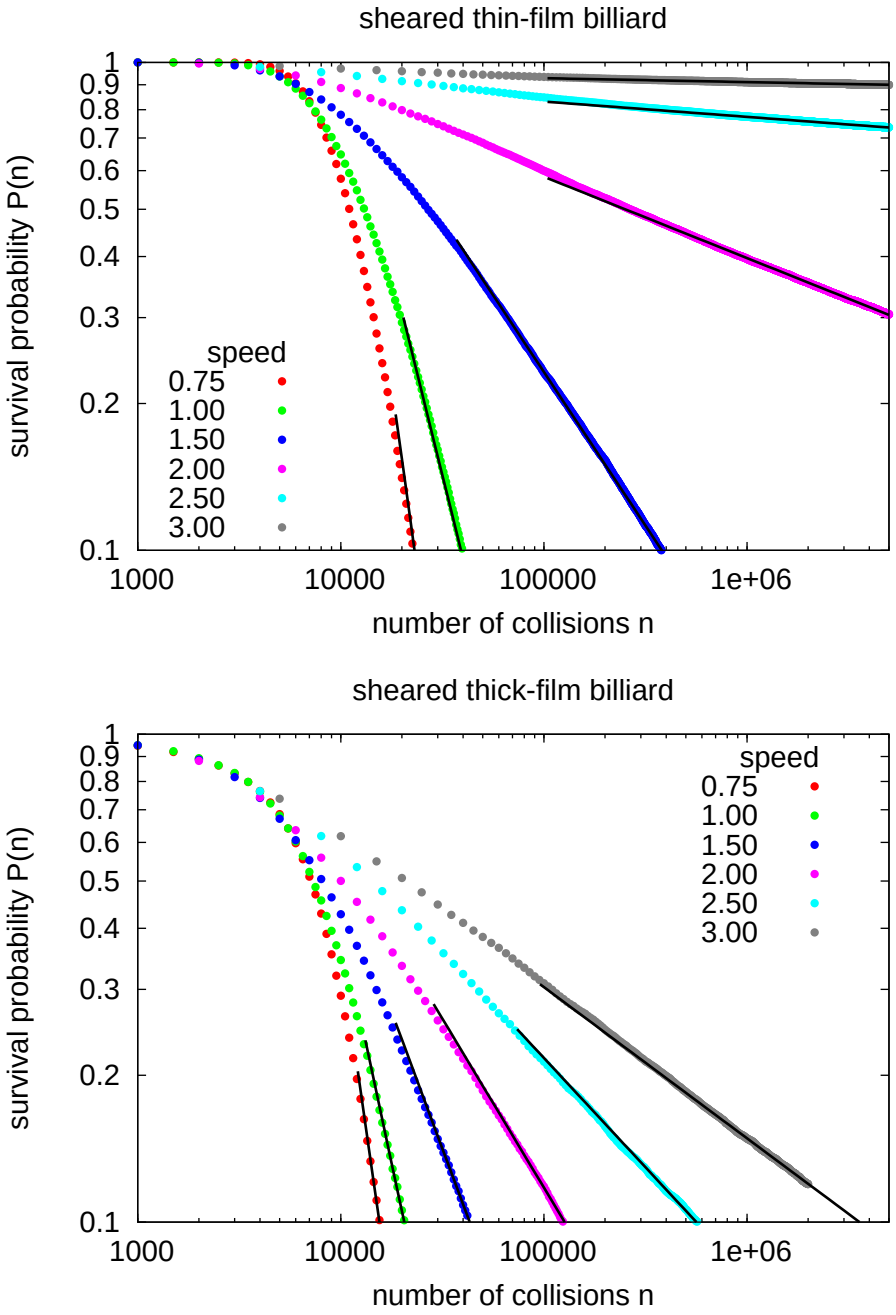

Figure 3.8: **Survival probability of sheared wet billiards.** In spite of increasing average energies (see Fig. 3.3) there remains a probability for individual systems to end up in the clustered state. For both wet billiards the survival probability $P(n)$ for a system with arbitrary initial condition not to be in the clustered state after n collisions decays with a power-law tail. In other words $1-P(n)$ is the cumulative lifetime distribution. In view of Sec. 2.1.3 the power-law lifetime distribution is an unexpected observation. Comparing the wet billiards the thick-film billiard experiences a higher probability to cluster. This is not unexpected because clustering may occur for all energies in the thick-film billiard (cf. Eq. 2.12). **Simulation details.** See Figs. 3.3 and 3.4 for $\langle E_{\text{ini}} \rangle = 9000$ or 10^4, respectively.

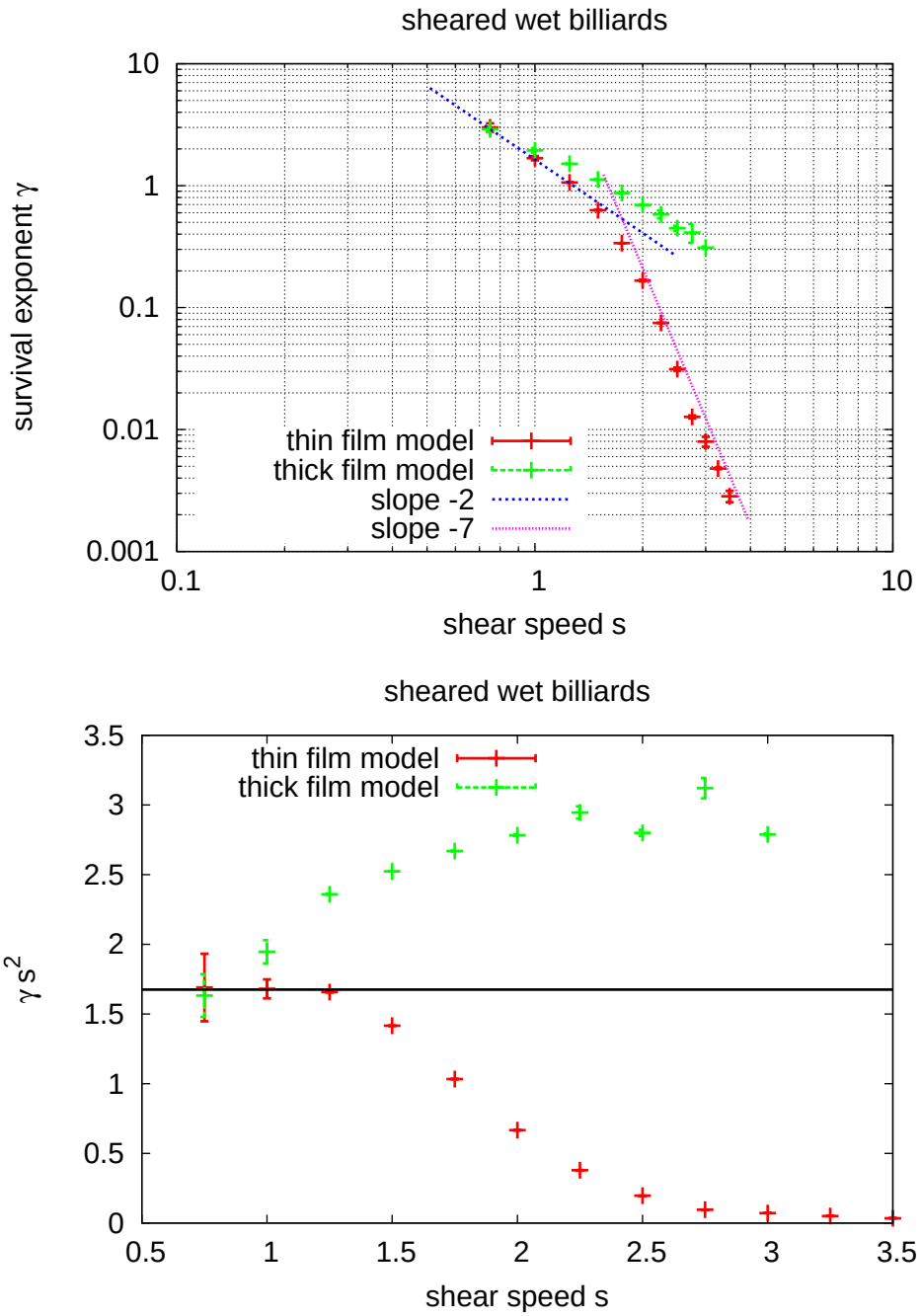

Figure 3.9: **Shear-speed dependence of the survival exponent.** The survival exponent γ depends on the shear speed s as shown. There seem to be two regimes separated rather by the initial critical value $s_c^0 \approx \sqrt{2}$ than by the asymptotic $s_c^\infty \approx 2$ (see Fig. 3.3). The bottom figure suggests that the thin-film billiard survival exponent is $\propto s^2$ for $s < s_c^0$ and gradually approaches zero, i.e. no clustering, for $s > s_c^0$. The survival exponent of the thick-film billiard shows a more uniform behavior. Note that the slopes in the top figure are mere guides to the eye. **Simulation details.** See Fig. 3.8.

3.2.2 Phase space and energy distribution

As discussed in the previous section clustering is still present in the sheared wet billiard. It therefore is a transiently chaotic system and we discuss phase space distributions on the chaotic saddle of non-clustered states (cf. Sec. 2.1.3). The phase space is 4-dimensional and as a consequence of the Fermi acceleration unbound in the energy coordinate[1]. Conveniently, the energy distribution, i.e. the projection of the phase space distribution onto the energy coordinate is asymptotically found to scale with the average energy $\langle E\rangle$ (Figs. 3.10 and 3.11). Thanks to this *scaling behavior*, a stationary "natural" phase space distribution can at least be observed on the rescaled phase space $(\theta, b, \Delta, \tilde{E})$ with $\tilde{E} := E/\langle E\rangle$.

Energy distribution. The energy distribution is assumed to be basically relaxed as soon as scaling occurs. For initial energies in the range of 10^3 to 10^4 this is the case after $n_s \approx 5 \cdot 10^4$ to 10^5 collisions. To ensure proper sampling especially of low energies, $E/\langle E\rangle \in [0, \delta]$, the simulation should be continued for about two recurrence times n_r into that region, $\Delta n = 2 \cdot n_r$. The recurrence time can be calculated from the escape rate κ [AT09], $n_r \sim \kappa^{-1}$. From Sec. 3.4 and Fig. 3.9 we find $\Delta n \sim n_s/7 \sim n_s$. Consequently, the energy distributions displayed should be sufficiently relaxed and well sampled. Furthermore, the simulations for $s = 2, 3$ were initialized with an exponential distribution of energies ($\langle E_{\mathrm{ini}}\rangle = 10^4$) to show that the deviation of the resulting distribution will not vanish by further relaxation. For $s = 1$ an isoenergetic initial distribution was chosen to show relaxation towards an almost exponential distribution. We summarize the following observations for the energy distribution of sheared billiards (Figs. 3.10 to 3.12):

- For the thin- (Fig. 3.10) and thick-film (Fig. 3.11, top) as well as for the elastic billiard (Fig. 3.11, bottom) the energy distribution asymptotically relaxes towards a distribution that scales with the average energy $\langle E\rangle$. Figure 3.13 illustrates that the two different times regimes found for the development of $\langle E\rangle$ in Figs. 3.3 and 3.4 seem to correspond to the relaxation towards and the asymptotically relaxed energy distribution, respectively.

  The initial energy development as introduced in the previous section seems to correspond to the relaxation towards the scaling distribution (see Fig. 3.13).

- The shape of the rescaled energy distribution roughly resembles an exponential function (Figs. 3.10 and 3.11),

$$\rho_{\langle E\rangle}(E) \approx \frac{1}{\langle E\rangle} \exp\left(-\frac{E}{\langle E\rangle}\right). \tag{3.4}$$

  The speed distribution consequently resembles the 2-dimensional Maxwell distribution as

$$\rho_{\langle E\rangle}(E)\,\mathrm{d}E \approx \frac{1}{\langle E\rangle} \exp\left(-\frac{E}{\langle E\rangle}\right)\mathrm{d}E \Longrightarrow \rho_{\langle E\rangle}(v)\,\mathrm{d}v \approx \frac{v}{\langle E\rangle} \exp\left(-\frac{v^2}{2\langle E\rangle}\right)\mathrm{d}v.$$

- There are noticeable deviations from the exponential distribution (Fig. 3.12).

[1] It should be recalled at this point that high energies are from a physical point of view outside the range of applicability of the thin-thread model to wet granular matter (cf. Sec. 1.1.2).

Natural distribution. Except for the energy coordinate the phase space distribution is found to be about uniform (see Appendix B.2). With the rescaled volume element

$$\mathrm{d}\tilde{\Gamma} = \mathrm{d}\theta\,\mathrm{d}b\,\mathrm{d}\Delta\,\mathrm{d}\tfrac{E}{\langle E\rangle}$$

the natural distribution reads

$$\rho\left(\theta, b, \Delta, \tilde{E}\right)\mathrm{d}\tilde{\Gamma} = \rho_\theta\left(\theta\right)\rho_b\left(b\right)\rho_{\tilde{E}}(\tilde{E})\rho_\Delta\left(\Delta\right)\mathrm{d}\tilde{\Gamma} = \frac{1}{2\pi}\frac{1}{2R}\frac{1}{L}f(\tilde{E})\mathrm{d}\tilde{\Gamma}, \tag{3.5}$$

where $f(x) \approx \exp(-x)$ denotes the scaling function of the energy distribution.

Concerning the Δ-coordinate this result is in contrast to previous results for a Lorentz gas sheared by an extended version of Lees-Edwards boundary conditions that enforces steady states [PIM94]. For this system the authors observed a strong structuring of the phase space in the Δ-dimension. The reasons given, however, seem to be rather a pathology of the algorithm than a property of the sheared Lorentz gas. Therefore it is no surprise to find different results for the simple Lees-Edwards boundary conditions.

From the previous chapter no significant structure but roughly uniformity was to be expected for the θ-b planes and projections. The stripe pattern related to the 2→1-mapping of the thin-film interaction (Sec. 2.3) will in principle not be suppressed by the shearing although the geometrical origin is complicated. Detecting it in a 2-dimensional section of the 4-dimensional phase space requires huge assemblies, however. As no new insights related to this effect are to be expected from studying it in the sheared system we will not further investigate this matter. Instead we concentrate on the energy distribution, which is also connected to understanding the observations from the previous section. The main questions arising is how the energy distribution and the scaling property can be understood from the underlying billiard dynamics. If the deviation from the exponential distribution are caused by correlations it seems especially interesting to identify these: Figure 3.12 indicates that liquid bridges decrease such correlations.

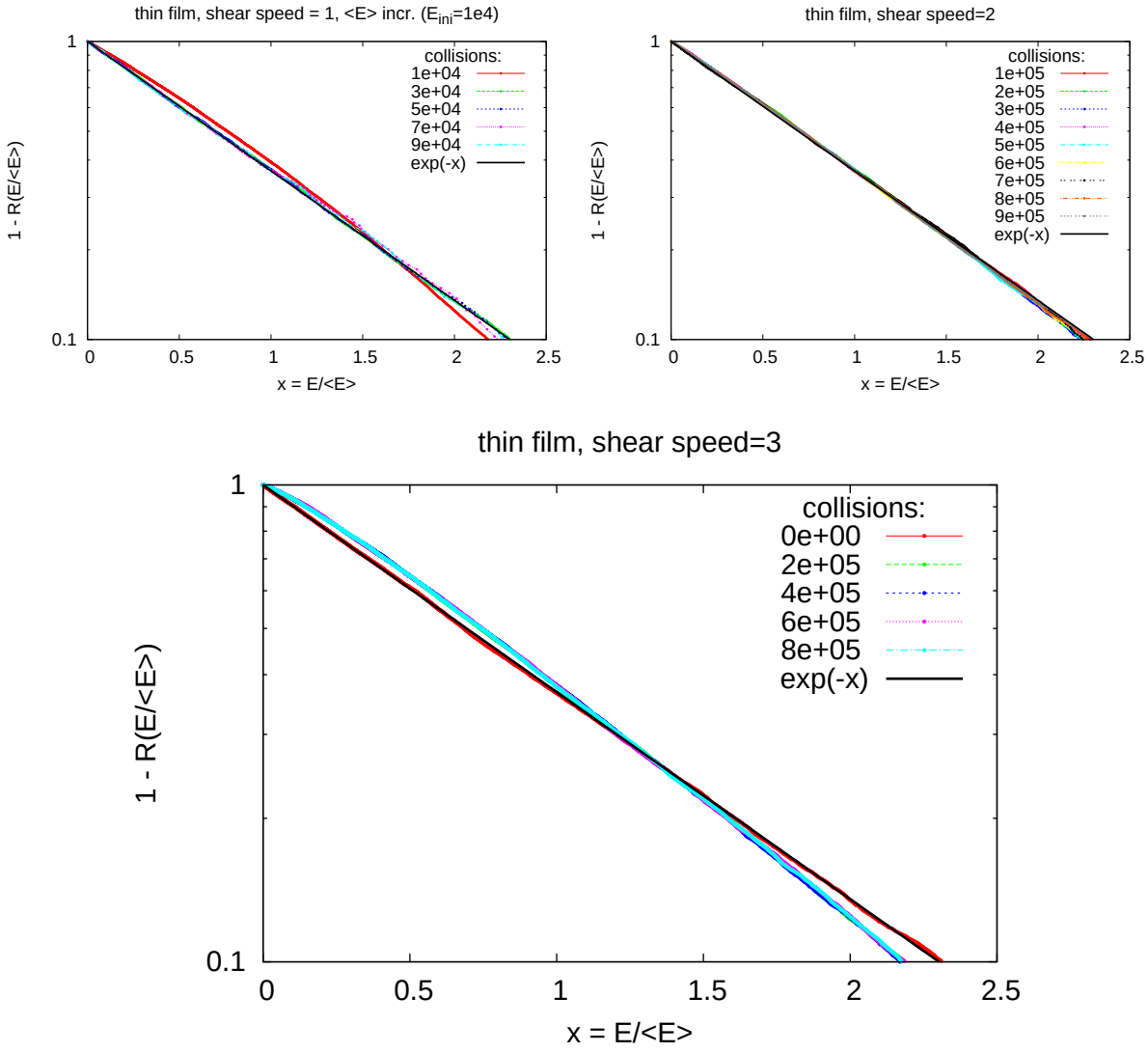

Figure 3.10: **Normalized cumulative energy distribution $R(x)$ of the sheared thin-film billiard for different shear speeds s in the asymptotic regime.** For high as well as low s the energy distribution scales with the average energy $\langle E\rangle$. Note that in the asymptotic regime $\langle E\rangle$ increases even for low shear speeds (Fig. 3.3). The rescaled energy $x := E/\langle E\rangle$ almost follows an exponential distribution as $R(x) = 1 - \exp(-x) \Longrightarrow \rho(x)\,\mathrm{d}x = \exp(-x)\,\mathrm{d}x$. There are however deviations from the exponential: The actual energy distribution possesses an exponential tail but deviates for smaller x. These deviations grow with increasing s, see Fig. 3.12. **Simulation details.** For $s = 1$ (top left) an isoenergetic initial distribution was chosen to show relaxation towards an almost exponential distribution. The simulations for $s = 2, 3$ (top right and bottom, respectively) were initialized with an exponential distribution of energies ($\langle E_{\mathrm{ini}}\rangle = 10^4$) to show that the deviation of the resulting distribution will not vanish by further relaxation. The distributions are normalized with respect to non-clustered states so that clustering is not represented. $N = 2 \cdot 10^4$ initial conditions for $s = 2, 3$, $N = 4 \cdot 10^4$ initial conditions for $s = 1$ to compensate high clustering probability (see Fig. 3.8); nevertheless fewer time steps are necessary to retain data quality. Each distribution is based on $> 10^3$ initial conditions. Apart from mentioned, default parameters were used (cf. Appendix A).

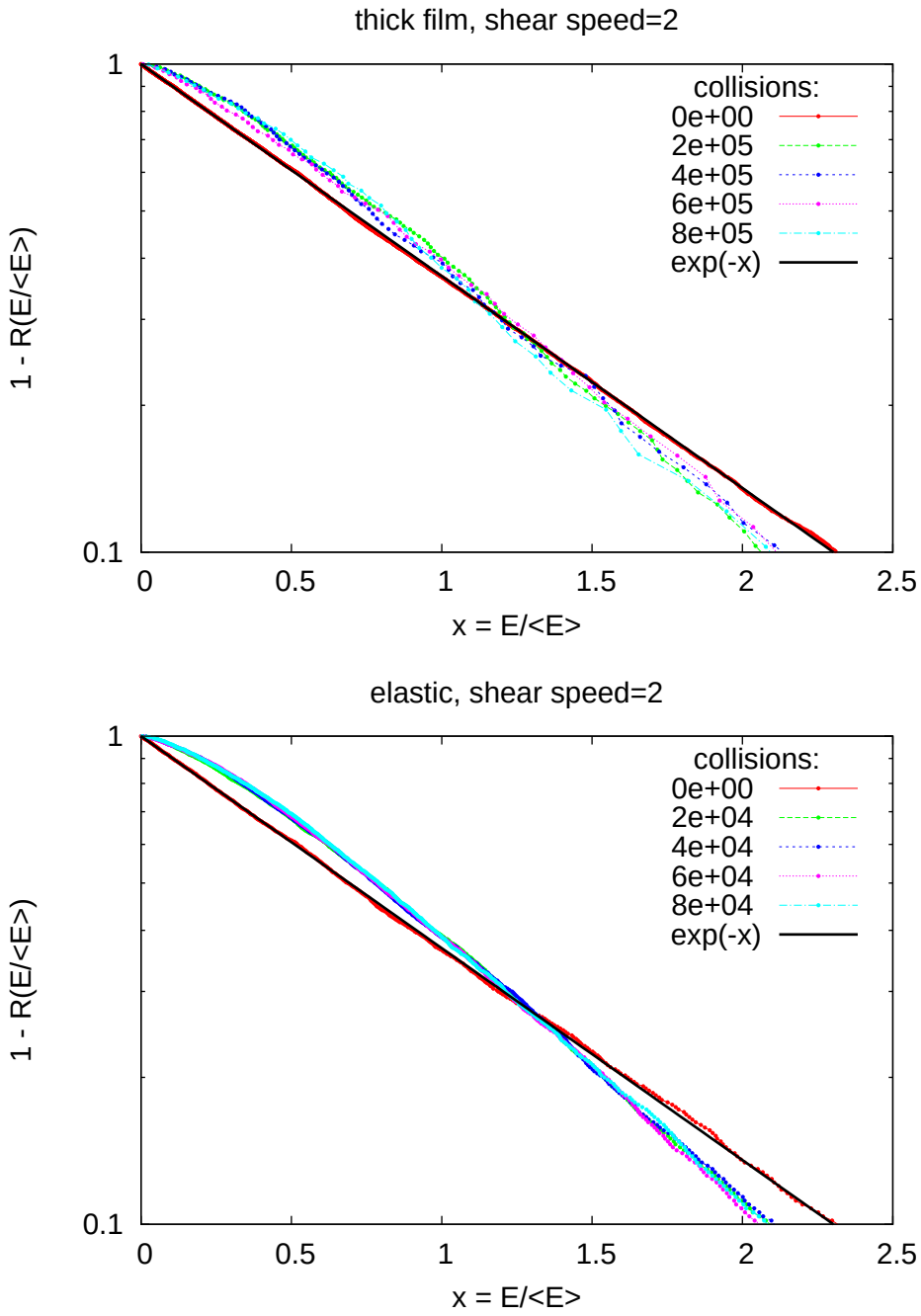

Figure 3.11: **Normalized cumulative energy distribution $R(x)$ of the sheared elastic and thick-film billiard in the asymptotic regime.** Like the sheared thin-film billiard (Fig. 3.10) the two other accelerating billiard systems show energy distributions that scale with the average energy $\langle E \rangle$. The deviations from the exponential energy, respectively Maxwellian velocity distribution (see Fig. 3.10) are more pronounced at smaller shear speeds (see also Fig. 3.12). **Simulation details.** Due to the normalization of the distribution clustering in the thick-film model (top) is not represented. $N = 2 \cdot 10^4$ initial conditions for thick-film model (top) out of which about 600 survived until the last distribution, $N = 5 \cdot 10^3$ initial conditions without loss for the elastic billiard (bottom). Both simulations were initialized with an exponential distribution of energies ($\langle E_{\text{ini}} \rangle = 10^4$ and 10^3 for thick film and elastic billiard, respectively). Apart from mentioned, default parameters were used (cf. Appendix A).

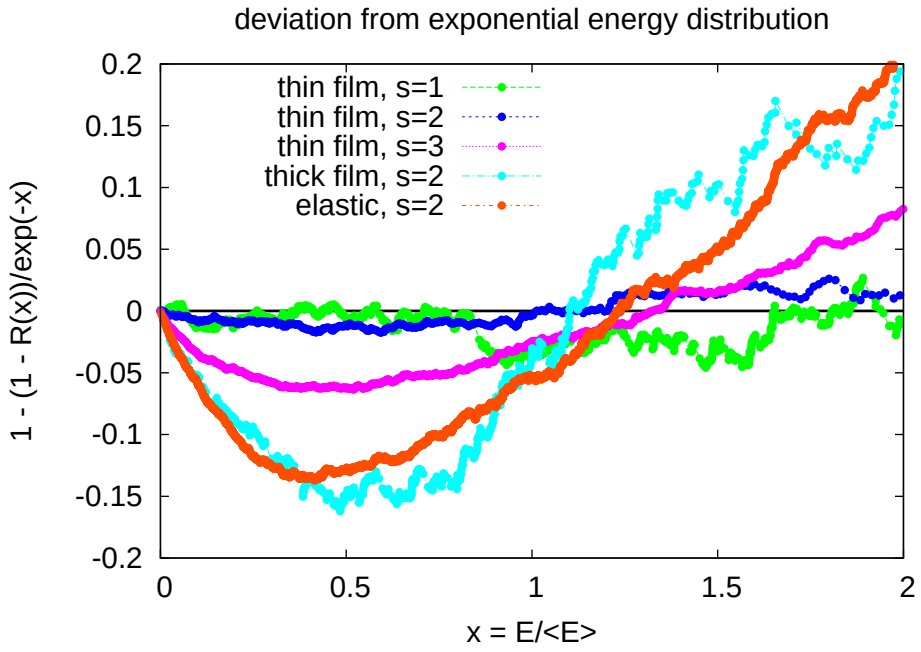

Figure 3.12: **Deviation from an exponential energy distribution.** As shown in Figs. 3.10 and 3.11 the sheared billiards possess energy distributions that scale with the average energy $\langle E \rangle$ and have a roughly exponential shape. There are deviations from the exponential, however. This figure focuses on the deviations by transforming the normalized cumulative energy distribution $R(E/\langle E \rangle)$ according to the labels. For the thin-film model at shear speed $s = 1$ the situation is unclear, but $s = 2$ strongly indicates a slight deviation that was not visible in the untransformed representation. For $s = 3$ there is a notable deviation. This indicates that the deviation grows with shear speed, which seems reasonable as for very high shear speeds the liquid bridge interaction should be negligible and the elastic billiard should be approached. The latter shows strong deviations. The thick-film model features deviations, which are comparable in strength to the elastic case. **Simulation details.** See Figs. 3.10 and 3.11.

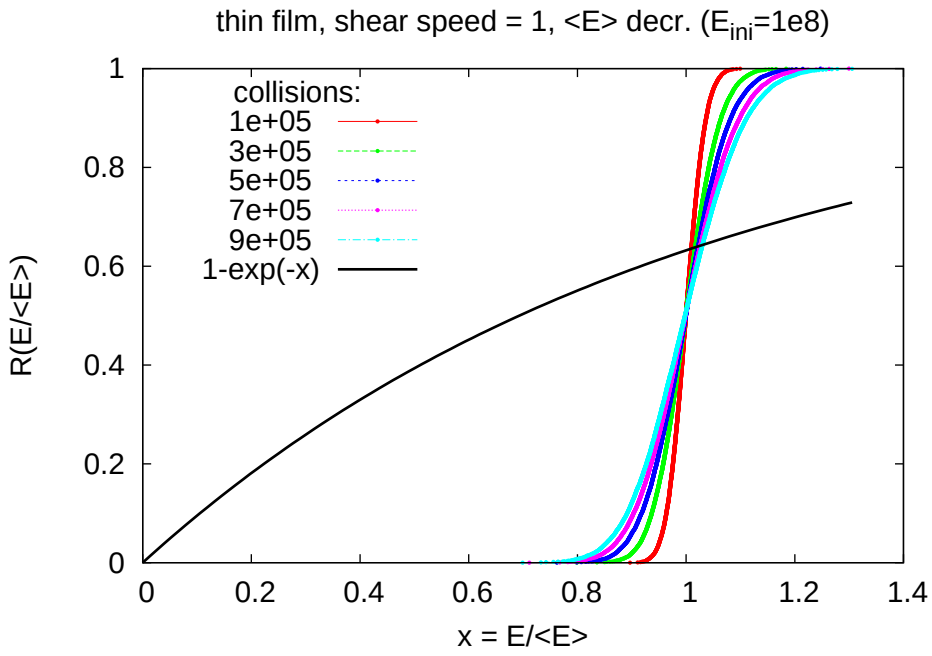

Figure 3.13: **Normalized cumulative energy distribution for the sheared thin-film model with low shear speed, initial regime.** For small shear rates like $s = 1$ the average energy $\langle E \rangle$ initially decreases linearly before asymptotically crossing over to linear increase (Fig. 3.3). The assembly displayed was isoenergetically initialized with a very high initial energy $E_{\text{ini}} = 10^8$. Thus, the time of crossover was sufficiently delayed to observe an energy distribution for the decreasing-$\langle E \rangle$ regime. In contrast to the asymptotic regime (Fig. 3.10) no scaling behavior is observed. Instead the distribution broadens, i.e. the standard deviation σ grows while the mean value $\langle E \rangle$ remains fixed. **Simulation details.** No system loss due clustering. $N = 2 \cdot 10^4$ initial conditions. $1 - \exp(-E/\langle E \rangle)$ was plotted for comparison to the asymptotic state. Apart from mentioned, default parameters were used (cf. Appendix A).

3.3 Fokker-Planck approach to the energy dynamics

The energy dynamics described in the previous section can be modeled as a generalized random walk that corresponds to a diffusion process with drift. We start this section by recalling how the Fokker-Planck equation formalizes the relationship between random walks and diffusion processes. Section 3.3.2 then intuitively connects the Fokker-Planck formalism to the sheared billiard dynamics and gives an overview of how the observation from Sec. 3.2 can be explained and modeled in principle. In the subsequent sections the presented ideas will eventually be substantiated.

3.3.1 Background

As discussed in Sec. 1.2.1 microscopic dynamics that are strongly chaotic allow for a stochastic ansatz in deriving equations for the macroscopic variables. The *Fokker-Planck equation* results from such an approach and goes back to Einstein's treatment of Brownian motion [Ein05]. Instead of considering the complete microscopic dynamics, the Fokker-Planck equation offers an equation of motion for the distribution function $\rho(x,t)$ of a fluctuating macroscopic variable[2] (e.g. [Ris89]):

$$\partial_t \rho(x,t) = \underbrace{-\partial_x \left[M(x)\rho(x,t)\right]}_{\text{drift}} + \underbrace{\tfrac{D}{2}\partial_x^2 \rho(x,t)}_{\text{diffusion}}. \tag{3.6}$$

The fluctuations, which are in principle determined by the micro-dynamics, are accounted for by (approximately Gaussian) stochastic fluctuations and lead to the diffusion term with constant *diffusion coefficient* D. The drift term incorporates the directed change of the macroscopic variable and is characterized by the *drift coefficient* M. From a transport-theoretic point of view the Fokker-Planck equation is an advection-diffusion equation resulting from the continuity equation corresponding to the conservation of probability:

$$\partial_t \rho(x,t) = -\partial_x j, \qquad j = \underbrace{M(x)\rho(x,t)}_{\text{advection}} - \underbrace{\tfrac{D}{2}\partial_x \rho(x,t)}_{\text{conduction}}$$

The probability current density j consist of an advective and a conductive part corresponding to directed motion and fluctuations.

The drift and diffusion coefficients M and D can be derived from a stochastic model of the microscopic dynamics. If, in particular, the microscopic dynamics can be modeled as a *generalized random walk*[3] the corresponding master equation might[4] be approximated by a Fokker-Planck equation [Gar85, Sec. 7.2.1]. The generalized random walk is characterized by the *transition probability* $\rho(x'|x)$ (per unit time) from state x to x', i.e. the probability distribution to find a new state x' given that the old state was x. The drift coefficient M is the first moment of the increment $\Delta x = x' - x$,

$$M(x) = \langle \Delta x \rangle = \int \Delta x \, \rho(x'|x) \, \mathrm{d}x', \tag{3.7}$$

[2] For simplicity we restrict the discussion to one dimension and constant diffusion coefficients in the present context.

[3] A generalized random walk shall denote here a Markovian jump processes, i.e. memoryless stochastic process that changes its state in discrete steps.

[4] For strict applicability of the Fokker-Planck equation the transition probability has to fulfill certain scaling assumptions. On a practical basis, however, the approximation works in most cases.

and reflects that a drift corresponds to the average change or movement of the macroscopic variable. The diffusion coefficient, on the contrary, is given as the second moment,

$$D\left(x\right) = \langle (\Delta x)^2 \rangle = \int (\Delta x)^2 \, \rho\left(x'|x\right) \, \mathrm{d}x', \tag{3.8}$$

and thus incorporates the stochastified microscopic fluctuations. The Fokker-Planck equation thus formalizes the relationship between random walks and diffusion processes.

To illustrate this we apply Eqs. 3.7 and 3.8 to a simple random walk with step size s and transition probability ρ,

$$\rho(x'|x) = \frac{1}{2}\left(\delta_{x',x-s} + \delta_{x',x+s}\right) \Longrightarrow M = 0, D = \frac{s^2}{2}.$$

The corresponding Fokker-Planck equation takes the form of the diffusion equation where the diffusion coefficient is related to the step size of the random walk. Note that a random walk in two independent coordinates can be decomposed to obtain the transport coefficients as above. Afterwards combining the Fokker-Planck equation for the individual coordinates yields the 2-dimensional diffusion equation with coordinate-independent diffusion coefficient D.

We finish by recalling some solutions of the diffusion equation: The fundamental solution ρ_f with initial conditions $\rho_f(x,0) = \delta(x)$ of the diffusion equation in d-dimensions on $(-\infty, \infty)$ that vanishes at ∞ is a Gaussian distribution [Tay96, p. 217]:

$$\rho_f(\vec{x}, t) = \frac{1}{(2\pi D t)^{d/2}} \, \exp\left(-\frac{\vec{x}^2}{2Dt}\right). \tag{3.9}$$

Note that this solution is also observed asymptotically, $t \to \infty$ and $\langle x \rangle \gg x_0$, for some localized initial condition. Thus, the asymptotic scaling of the mean-square displacement typical to diffusion follows:

$$\langle \vec{x}^2 \rangle = \int_{-\infty}^{\infty} \vec{x}^2 \rho_f(x,t) \, \mathrm{d}\vec{x} = dDt.$$

The fundamental solution $\rho_a(x,t)$ of the 1-dimensional diffusion equation on $\mathbb{R}^+$ with absorbing boundary condition, $\rho_a(x=0,t) = 0$, takes asymptotically the form of the Maxwell speed distribution in 2 dimensions. This is found from Eq. 3.9 by the method of mirror images,

$$\begin{aligned}
\rho_a(x,t) &= \mathcal{N}\left[\rho_f(x - x_0, t) - \rho_f(-(x - x_0), t)\right] \\
&= \mathcal{N}' \, \exp\left(-\frac{x^2 + x_0^2}{2Dt}\right) \sinh\left(\frac{x^2}{Dt}\frac{x_0}{x}\right) \overset{x_0 \ll \langle x \rangle}{\approx} \mathcal{N}'' \, x \, \exp\left(-\frac{x^2}{2Dt}\right) \\
&= \frac{1}{Dt} \, x \, \exp\left(-\frac{x^2}{2Dt}\right) \qquad \text{with} \qquad x \in \mathbb{R}^+
\end{aligned} \tag{3.10}$$

where the $\mathcal{N}$ are determined from normalization. We note the exact proportionality of the mean-square displacement to Dt in this case,

$$\langle x^2 \rangle = \int_0^{\infty} x^2 \rho_a(x,t) \, \mathrm{d}x = 2Dt \tag{3.11}$$

and remark that for *algebraic corrections* to the Gaussian the above relation holds with a modified proportionality constant ($k > 0, G > -1$):

$$\rho_c(x,t) = \frac{x^G \exp\left(-k\frac{x^2}{2Dt}\right)}{\int_0^\infty x^G \exp\left(-k\frac{x^2}{2Dt}\right) \mathrm{d}x} \qquad \Rightarrow \qquad \langle \vec{x}^2 \rangle = \frac{(1+G)}{k} Dt \tag{3.12}$$

3.3.2 Intuitive picture

Given that the chaotic billiard dynamics ensures undirected motion (i.e. especially that the θ-distribution is always uniform) Lees-Edwards boundary conditions (Sec. 1.1.4/3.1, all notation as explained there) can be viewed as causing a random walk with step size s in the velocity component parallel to the boundary, v_x: Crossing a top boundary means $v_x \to v_x + s$ while crossing a bottom boundary implies $v_x \to v_x - s$. Further assuming that the billiard dynamics are sufficiently chaotic to ensure $\rho(v_y) = \rho(v_x)$, i.e. the collisions distribute the velocity change in some sense evenly between the velocity components, the velocity dynamics of the sheared billiard systems can be modeled as an unbiased, unrestricted random walk in the two velocity dimensions. Following the previous section, the velocity distribution $\rho(v_x, v_y, t)$ is consequently expected to be described by the 2-dimensional diffusion equation

$$\partial_t \rho(v_x, v_y, t) = \frac{D}{2}\left[\partial_{v_x}^2 \rho(v_x, v_y, t) + \partial_{v_y}^2 \rho(v_x, v_y, t)\right],$$

with a diffusion coefficient $D \propto s^2$ and zero-boundary conditions at infinity. From Eq. 3.9 and $\rho(t=0) = \delta(v_x)\delta(v_y)$ the velocity components follow the distribution

$$\rho(v_x, v_y, t)\ \mathrm{d}v_x \mathrm{d}v_y = \frac{1}{2\pi Dt} \exp\left(-\frac{v_x^2 + v_y^2}{2Dt}\right) \mathrm{d}v_x \mathrm{d}v_y$$

$$\Rightarrow \qquad \rho(v,t)\ \mathrm{d}v = \frac{1}{Dt}\, v \exp\left(-\frac{v^2}{2Dt}\right) \mathrm{d}v, \tag{3.13}$$

which corresponds to the 2-dimensional Maxwell distribution of the speed v. This coincides to a first approximation with the billiard simulations (see Figs. 3.10 and 3.11). It shows that the energy increase is due to *diffusive broadening*, which is (asymptotically, $v(0) \approx 0$) given by the mean-square displacement (cf. Eq. 3.11):

$$\langle E \rangle = \frac{1}{2}\langle v^2 \rangle \approx Dt. \tag{3.14}$$

The 2-dimensional random walk picture is illuminating to understand how Lees-Edwards boundary conditions increase the system energy although they appear to be a symmetric concept. For further studying the energy/speed dynamics, however, a 1-dimensional process is more suitable. Expressing the 2-dimensional diffusion equation in polar coordinates allows to take advantage of the rotational symmetry. Only considering the radial part v shows that the speed is described by a 1-dimensional diffusion equation with drift ([Gar85, Sec. 5.3.1]):

$$\partial_t \rho(v,t) = -\partial_v \frac{D}{2v} \rho(v,t) + \frac{D}{2} \partial_v^2 \rho(v,t).$$

As $v > 0$ and as non-moving particles are removed from the simulations (cf. Sec. 3.1.1) there is an absorbing boundary at $v = 0$ for the 1-dimensional diffusion. This boundary prevents a symmetric broadening as occurring in the 2-dimensional case. Consequently, the speed/energy distribution is influenced by diffusive broadening (Eq. 3.11) as well as by the drift. The drift coefficient decreases with increasing speed, reflecting the fact that the number of states at a given distance v from the origin in the plane increases with v. Low v are thus less likely, resulting in a drift to higher v. From a geometric viewpoint the diffusive motion in the plane has been reduced to a diffusive dynamics on $[0, \infty]$ with a potential hump with maximum at 0. Recalling that the average energy increase by a Lees-Edwards boundary crossing, s^2 (Eq. 1.6), is independent of the system speed and thus insignificant for $v \gg s$ this seems plausible. Neglecting the drift effects for $\langle v \rangle \gg s$ asymptotically leaves pure diffusion, and taking into account the boundary (Eq. 3.10) recovers Eqs. 3.13 and 3.14.

So far neither dissipation due to the wet interaction nor clustering have been discussed. The former results in a drift towards smaller speeds and is incorporated by modifying the drift coefficient. As the liquid bridge dissipation is independent of the system energy (cf. Eq. 1.4) the effects of the liquid bridges should decrease with increasing v just as the drift effect of the Lees-Edwards boundaries does. Another way to motivate the $1/v$ dependence is that the variable transformation from $E = v^2/2$ to v has a factor v in the Jacobian. Consequently, the modified drift coefficient μ should thus be of the form $\mu \sim (s^2 - \epsilon)/v$. The liquid bridges have no diffusive effect so that the asymptotic diffusion regime is expected to remain unaffected by incorporation of liquid bridges. In fact, within the approximation of Eq. 3.13 the energy distributions for the wet and elastic billiard coincide (see Figs. 3.10 and 3.11).

For the thin-film billiard clustering only occurs below a critical energy E_c (Eq. 2.9) and thus corresponds to an absorbing boundary close to zero, i.e. the plane or the potential hump are correspondingly cut out. The thick-film billiard can reach the clustered state for all energies with decreasing probability (cf. Eq. 2.12). Thus, absorption takes place in the bulk and not in a boundary region.

While the diffusive effects can be studied well in the asymptotics the drift effects can be isolated if an assembly is initialized with an energy/speed distribution that does not reach out to the boundary, e.g. $\rho(v, 0) = \delta(v - v_0)$ or $\rho(v, 0)$ uniform on some interval separated from $v = 0$. In these cases diffusive broadening will initially be symmetric and not affect the averages. Not having to consider diffusion and circumventing the velocity dependence in the drift coefficient, the energy development in the drift regime is easiest obtained by a direct balancing of the dissipation, $-\epsilon n$, and the energy input due to shearing, $s^2 n$. This way the energy is expected to change according to

$$\langle \Delta E \rangle + \epsilon \propto s^2,$$

where the proportionality is determined by the average number of boundary crossings per collision. Section 3.3.3 uses this perspective to illustrate the absence of a steady state for the wet billiards (Figs. 3.3 and 3.4, top).

For the wet billiards the drift and diffusion regime can be told apart from a change in energy slope (Figs. 3.3 and 3.4, bottom). For the elastic billiard no change is found (Fig. 3.5). This finding is probably due to the fact that for $\epsilon = 0$ the drift and diffusion coefficients are very similar so that the energy increase appears the same in both regimes.

The sketch of the sheared billiard energy dynamics presented so far will be supported and concretized in the following sections:

- In Sec. 3.3.4 a stochastic model for the deterministic billiard energy dynamics is derived. As the deviations from the exponential energy distribution cannot be explained by a simple random walk as depicted so far a generalization with varying and velocity-dependent step-size is needed. By simulations the generalized random walk is shown to reproduce the energy distributions found in Figs. 3.10 and 3.11 qualitatively. In particular, the correlations that cause the deviation from the exponential distribution of Figs. 3.10 to 3.12 are identified. Quantitative restrictions are discussed.
- Section 3.3.5 derives the transport coefficients. As discussed, the diffusion coefficient is shown to be constant while the drift coefficient decreases as $1/v$.
- The resulting Fokker-Planck equation is discussed in Sec. 3.3.6. It is exemplarily solved for the elastic case.

In Sec. 3.4 the power-law lifetime distribution found for the wet billiards (Fig. 3.8) is finally explained by the unboundedness of phase space, which is caused by Fermi acceleration, and results in an effectively shrinking leak. The quantitative treatment of the clustering rate shows possible restrictions of the previous asymptotic discussion of the energy distribution.

3.3.3 Energy balance and acceleration

Instead of finding a steady state as in the dry case (Fig. 3.6) the average energy $\langle E \rangle$ of the wet billiards is asymptotically described by diffusive broadening. This observation can be explained by considering the transition from an initial distribution localized at (or around) an energy $E_0 > 0$. Initially diffusion only affects the width of the distribution but not its mean $\langle E \rangle$. Thus energy balancing suffices to describe the change in $\langle E \rangle$. The absence of a steady state in the wet billiards is then readily explained by the fact that they are lacking a feed-back mechanism to adjust to the steady-state energy. After all, both the energy input due to Lees-Edwards boundary conditions and the amount of energy dissipated by a bridge rupture are independent of the system energy. In contrast, inelastic dissipation is proportional to the energy (Sec. 1.1): For low energies the constant energy input from the boundary conditions dominates the evolution so that energy rises – for large energy, dissipation dominates so that energy decreases. For systems with dissipation due to a finite coefficient of restitution the contributions balance for some intermediate E such that the dynamics approaches a well-defined steady state.

On average, the crossing of a Lees-Edwards boundary increases the system energy by $(\Delta E)_{\mathrm{LE}} = s^2/2$ (Eq. 1.6). In an inelastic collision the dissipation is (cf. Eq. 2.8)

$$(\Delta E)_{\mathrm{res}} = (\alpha - 1)\,\frac{\langle v_n^2 \rangle}{2} = -\,(1-\alpha)\,E\langle \cos^2\varphi \rangle =: -c\,(\alpha)\cdot E,$$

where $v_n = v\cos\varphi$ with the incident angle φ is used and the average $\langle\cdot\rangle$ is taken over the phase-space distribution $\rho\,(\varphi)$. The total energy change per collision is

$$(\Delta E)_{\mathrm{dry}} = \nu\frac{s^2}{2} - c\cdot E,$$

where the *average number of boundary crossings per collision*, $\nu = n_{\mathrm{LEBC}}/n_{\mathrm{coll}}$, has been introduced to weight the events according to their occurrence (see Fig. B.14 for numerical data). A steady state (with respect to the number of collisions) fulfills $\Delta E = 0$. In the inelastic billiard there exists a steady-state energy E_0 for all shear speeds s:

$$(\Delta E)_{\mathrm{dry}} \stackrel{!}{=} 0 \quad \Longrightarrow \quad E_0 = \frac{\nu}{2c} s^2 \propto s^2$$

It is proportional to s^2 as confirmed by the simulation results (Fig. 3.6). Note that E_0 grows with the boundary crossing frequency ν. Assuming φ to be uniformly distributed, i.e. $\langle \cos^2 \varphi \rangle = 1/2$, the parameter values $\alpha = 1/2$, as in Fig. 3.6, and $\nu = 0.9$, from Fig. B.14, yield: $E_0 = 1.8 s^2$. This proportionality constant disagrees with the numerical data in Fig. 3.6. The reason probably is that φ is not uniformly distributed: The normal restitution causes an alignment of collision partners (cf. [PB04, Sec. 6.3]), which results in a higher population of large impact parameters (Fig. 2.5, bottom).

Similarly, in the wet billiards a bridge rupture decreases the energy by $(\Delta E)_{\mathrm{bridge}} = -\epsilon$ (Eq. 2.6). The total energy change per collision for the thin-film billiard is thus

$$(\Delta E)_{\mathrm{wet}} = \nu \frac{s^2}{2} - \epsilon$$

As observed in the simulations (Figs. 3.3 and 3.4), the steady-state condition is only fulfilled for a critical shear speed s_c that matches the constant dissipation ϵ:

$$(\Delta E)_{\mathrm{wet}} \stackrel{!}{=} 0 \quad \Longrightarrow \quad \left(s_c^0\right)^2 = \frac{2\epsilon}{\nu} \approx \begin{cases} 2.1 & \text{thin film} \\ 2.3 & \text{thick film} \end{cases} \tag{3.15}$$

The numerical value has been obtained using $\epsilon = 1$ and $\nu = 0.96$ for the thin-film and 0.87 for the thick-film billiard (Fig. B.14). The value $(s_c^0)^2 \approx 2$ coincides with the initial s_c^0 from Figs. 3.3 and 3.4. For $s = s_c^0$ a steady state should exist. It is not stable, however: Due to inevitable fluctuations in the dynamics the system will eventually always cross over to the energy-increasing diffusive regime.

3.3.4 Stochastic model of the speed dynamics

The sheared billiard systems are chaotic and thus feature fast decay of correlations (see Fig. B.13). Relying on this feature a generalized random walk model for the deterministic speed dynamics of the sheared elastic and thin-film billiard is derived in the following. Recall after all that a simple random walk would not reproduce the deviations from the exponential energy distribution (Sec. 3.3.2). Based on Sec. 3.3.2 the speed v is chosen to be the random-walk variable while for graphical representations $E = v^2/2$ with its almost exponential distribution is more convenient.

Deterministic billiard speed dynamics. Before presenting the corresponding stochastic model we review the deterministic billiard dynamics: There are two events affecting the energy or speed, respectively: On the one hand Lees-Edwards boundary crossing with (cf. Eq. 3.2)

$$\mathrm{LE}\,(v) = \sqrt{v^2 + s^2 + 2sv\cos\theta}, \tag{3.16}$$

where we recall that the speed dynamics depends directly only on θ and that depending on θ the speed can increase or decrease. For the wet billiard systems, on the other hand, bridge rupture decreases the speed without dependence on the other coordinates (cf. Eq. 2.6):

$$\mathrm{B}\,(v) = \sqrt{v^2 - 2\epsilon}. \tag{3.17}$$

Each collision is followed by a number $\chi = 0, 1, 2, ..$ of Lees-Edwards boundary crossings that is determined by the billiard dynamics (cf. Sec. 3.1.1):

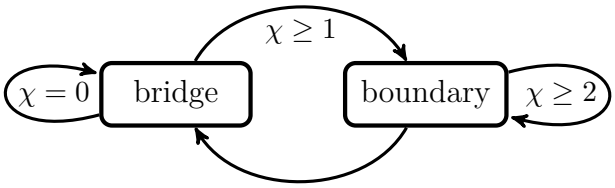

For the wet billiards the above energy modifications have to be augmented by clustering of particles. For the thin-film billiard this happens if $E < E_c$ (see Eq. 2.9) with an energy-dependent probability $P\,(\text{cluster}|E)$ that is given by the size of the clustering region (Eq. 2.11). The corresponding expression for the speed reads:

$$P\,(\text{cluster}|v) = \begin{cases} 1 & \text{if } v < \sqrt{2} \\ 1 - (1+L)\sqrt{1 - \frac{2}{v^2}} & \text{if } v < \sqrt{2E_c}\,. \\ 0 & \text{else} \end{cases} \tag{3.18}$$

Stochastic modeling. The deterministic θ in $\mathrm{LE}\,(v)$ is replaced by a stochastic one,

$$\mathrm{LE}_\Theta\,(v) = \sqrt{v^2 + s^2 + 2sv\cos\Theta_n},$$

where Θ_n is a random variable that is assumed to be uniformly distributed in $[0, \pi]$ as it substitutes a post-collision angle (see Appendix B.2 for numerical data). Due to the π-rotation symmetry of Lees-Edwards boundary conditions it is again sufficient to restrict the discussion to the first and second quadrant while $s > 0$. All Θ_n are assumed to be uncorrelated, incorporating the fast decay of correlations (Fig. B.13).

For the bridge map no stochastification is necessary as it only depends on v and the parameter ϵ, not on the other coordinates. Thus, Eq. 3.17 is maintained in the stochastic model.

For simplicity we assume that a collision is either followed, $\chi = 1$, or not followed, $\chi = 0$, by a single Lees-Edwards boundary crossing. This is modeled by a binary random variable X with $X = 1$ for boundary crossing and $X = 0$ for two consecutive collisions, respectively:

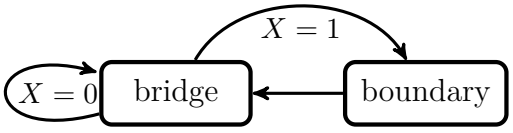

The boundary crossing thus becomes optional:

$$\mathrm{LE}_{\Theta,X}\,(v) = \sqrt{v^2 + X\,(s^2 + 2sv\cos\Theta_n)}.$$

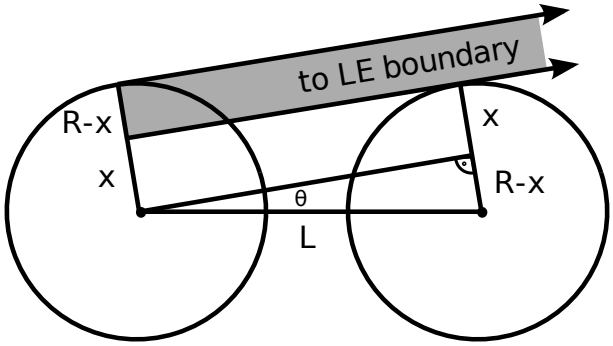

Figure 3.14: **Lees-Edwards boundary crossing probability as function of θ.** Based on Appendix B.2 it is assumed that the post-collision impact parameter b is uniformly distributed in $[-R, R]$ where R is the radius. For the elastic billiard the probability that a collision is followed by a Lees-Edwards boundary ($X = 1$) is then given by $P(X = 1|\theta) = \frac{R-x}{2R} = \frac{L|\sin\theta|}{2R}$ as long as $|\sin\theta| \leq \frac{2R}{L}$. For $\frac{2R}{L} \leq |\sin\theta| < 1$ the boundary will be crossed irrespective of b, i.e. $P(X = 1|\theta) = 1$. Equation 3.19 follows with $R = 1$. For the thin-film billiard the argument above has to be based on the post-bridge instead of the post-collision situation. The values of b and θ are still uniformly distributed here, but the impact parameter is spread on $[-R/\sqrt{1-\frac{\epsilon}{E}}, R/\sqrt{1-\frac{\epsilon}{E}}]$ (see Eq. 2.7). In the sketch this only affects the post-collision part, i.e. the left scatterer and $P(X = 1|\theta) = \frac{L|\sin\theta|}{2R}\sqrt{1-\frac{\epsilon}{E}}$. For $\langle E\rangle \gg \epsilon$ as in the scaling regime the correction is small, however, and the elastic approximation is sufficient for qualitative considerations.

The probability of finding a boundary crossing ($X = 1$) depends in principle on θ as well as on b. Assuming b to be uniformly distributed (Appendix B.2) it is possible to average out the b-dependence. Figure 3.14 derives this correlation for the elastic billiard. As the spatial dynamics is only slightly influenced by the bridge-rupture map for $\langle E\rangle \gg \epsilon$, the expression is also a sufficient approximation for the thin-film billiard:

$$P(X = 1|\theta) = \begin{cases} \frac{L}{2}|\sin\theta| & \text{if } |\sin\theta| < \frac{2}{L} \\ 1 & \text{if } |\sin\theta| \geq \frac{2}{L} \end{cases}. \tag{3.19}$$

This correlation of X on Θ will prove to be responsible for the deviations from the exponential energy distribution.

Clustering as described by Eq. 3.18 could be included by means of a third random variable. For simplicity $P(\text{cluster}|v)$ from Eq. 3.18 is instead replaced by step function with $P(\text{cluster}|v < C) = 1$ and $P(\text{cluster}|v > C) = 0$ where C is some suitable constant. For the elastic case $C = 0$ implements an absorbing boundary at $v = 0$. There exists an absorbing boundary because the state $v = 0$ may only be reached by particles parallel to the Lees-Edwards boundary that happen to cross due to numerical imprecision. These pathological non-colliding trajectories are filtered in the simulation (cf. Sec. 2.1.2). In the wet case the clustering constant C should be determined such that the absolute clustering probability is preserved,

$$P(\text{cluster}) = \int_0^{\sqrt{2E_c}} P(\text{cluster}|v)\,\rho(v)\,\mathrm{d}v \stackrel{!}{=} \int_0^C \rho(v)\,\mathrm{d}v.$$

Here $\rho(v)$ is the velocity distribution for very small velocities. However, nothing is known about the energy distribution for low energies as the numerical data does not properly

resolve very small energies/speeds. Therefore $C > \sqrt{2\epsilon}$ has to be chosen more or less arbitrarily. The present model thus only qualitatively captures clustering.

The elements just discussed can now be combined to describe a (one-step) stochastic process. One possibility to do so is the following:

$$v_{n+1} = \begin{cases} 0 & \text{if} \quad v_n \leq C \\ \mathrm{LE}_{\Theta,X}(\mathrm{B}(v_n)) = \sqrt{v_n^2 - 2\epsilon + X\left(s^2 + 2s\sqrt{v_n^2 - 2\epsilon}\cos\Theta\right)} & \text{else} \end{cases}$$

Here the bridge rupture is performed before the (possible) boundary crossing. This order of events is in accordance with the post-collision Poincaré section of the billiard dynamics: Starting in a post-collision position bridge rupture comes before boundary crossing. Moreover, the clustering condition is checked before the bridge, i.e. the bridge rupture and boundary crossing cycle is only performed if the speed was high enough to rupture the bridge.

A slightly different version to set the stochastic process up is the following:

$$v_{n+1} = \begin{cases} 0 & \text{if} \quad \mathrm{LE}_{\Theta,X}(v_n) \leq C \\ \mathrm{B}(\mathrm{LE}_{\Theta X}(v_n)) = \sqrt{v_n^2 + X\left(s^2 + 2sv_n\cos\Theta\right) - 2\epsilon} & \text{else} \end{cases}.$$

In this version the (possible) boundary crossing is performed first, followed by the bridge. This shifted sequence is no problem, however, as it only corresponds to increasing the initial energy by 2ϵ. The price to pay for the reversed order of events is the complicated clustering condition. As C must be estimated anyway, it does not harm to handle the clustering condition roughly by introducing some other constant $C' \leq C$:

$$1) \qquad v_{n+1} = \begin{cases} 0 & \text{if} \quad v_n \leq C' \text{ or } v_n \notin \mathbb{R} \\ \sqrt{v_n^2 + X\left(s^2 + 2sv_n\cos\Theta\right) - 2\epsilon} & \text{else} \end{cases}. \tag{3.20}$$

The clustering condition is loosened to compensate for situations with $v_n < C < \mathrm{LE}_{\Theta,X}(v_n)$. If $\mathrm{LE}_{\Theta,X}(v_n) < C < v_n$ the radicand might become negative, which is also filtered. The (asymptotic) results presented in the following are, however, insensitive to the implementation of the clustering condition.

Figure 3.15 compares the rescaled energy distribution obtained from simulating the stochastic model Eq. 3.20 (*type* 1) with $\epsilon = 0 = C'$ to the billiard simulations for the elastic case. The deviations from the exponential distribution are qualitatively reproduced. The figure also illustrates that the model can be further simplified (*type* 2) without loss of performance by replacing the binary variable X with its expectation value,

$$\langle X \rangle = \int_0^{\pi} P\left(X = 1|\theta\right)\rho\left(\theta\right)\,\mathrm{d}\theta = 2\int_0^{\pi/2} P\left(X = 1|\theta\right)\rho\left(\theta\right)\,\mathrm{d}\theta \quad \text{with} \quad \rho\left(\theta\right) = \frac{1}{\pi}. \tag{3.21}$$

The expectation value $\langle X \rangle$ is a constant depending on the system parameters L and R and the simplified process used from now on reads:

$$2) \qquad v_{n+1} = \begin{cases} 0 & \text{if} \quad v_n < C' \text{ or } v_n \notin \mathbb{R} \\ \sqrt{v_n^2 - 2\epsilon + \langle X \rangle\left(s^2 + 2sv_n\cos\Theta\right)} & \text{else} \end{cases} \tag{3.22}$$

A third variant of the process (*type* 3) illustrates that the correlation between Θ and X (Eq. 3.19) causes the deviation from the exponential as the θ-dependent crossing probability transforms the uniform post-collision θ-distribution into a non-uniform one at the boundary: Reconsider the type-1 stochastic process Eq. 3.20 but replace the correlated binary variable X by an uncorrelated $\tilde{X}$ with $P(\tilde{X}=1|\theta) = P(\tilde{X}=1) = \langle X \rangle$ such that the expectation value does not change:

$$3) \qquad v_{n+1} = \begin{cases} 0 & \text{if} \quad v_n \leq C' \text{ or } v_n \notin \mathbb{R} \\ \sqrt{v_n^2 + \tilde{X}\left(s^2 + 2sv_n\cos\Theta\right) - 2\epsilon} & \text{else} \end{cases}$$

For this process the crossing probability is θ-independent, which keeps the uniformity of θ also at the boundary and results in an exponential speed distribution. Note that the type-3 process is merely a formal example. Its billiard counterpart would require an unnatural non-uniform θ-distribution in the post-collision section.

Figure 3.16 compares the rescaled energy distribution obtained by the type-2 stochastic process Eq. 3.22 with $\epsilon = 1$ and $C' = \sqrt{3}$ to the billiard simulations for different shear speeds. The qualitative dependencies of the extent of the deviations seem to be met: Increasing shear speed s increases the dimension of the deviation and the presence of bridge dissipation decreases it.

Except for its shape given by rescaling $E/\langle E \rangle$ the energy distribution is characterized by the average energy $\langle E \rangle$. Figure 3.17 shows that the average energy increases linearly with a slope that is proportional to s^2. The proportionality constants, however, strongly deviate from the ones found in the billiard simulations (Figs. 3.3 and 3.5).

To understand the limitations of the stochastic model and especially the poor capture of the average energy it is useful to recall the assumptions behind the stochastic model:

- In between two Lees-Edwards boundary crossings the billiard dynamics is sufficiently chaotic to replace the deterministic θ in the energy change on Lees-Edwards boundary crossing by a stochastic one without memory; correlations as in Fig. B.13 can be neglected. Substituting a post-collision angle, θ is assumed to be uniformly distributed in $[0, 2\pi]$ (see Sec. B.2 for numerical data).

- For the thin-film billiard the energy-dependent clustering probability Eq. 3.18 was replaced by a simple removal of systems with E smaller than a somewhat arbitrary constant.

- In the deterministic billiard dynamics several boundary crossings may occur in between two collisions. For the stochastic model it was in contrast assumed that a collision is either followed or not followed by a single Lees-Edwards boundary crossing. To obtain a probability for crossing that only depends on θ the impact parameter b is assumed to be uniformly distributed (Sec. B.2).

Besides the fact that clustering is not modeled very accurately, the modified sequence of events in the last assumption clearly is the weakness of the stochastic approach as far as the energy distribution is concerned. In particular, assuming a maximum of one Lees-Edwards boundary in between two collisions prevents the model from exhibiting the same number of boundary crossings per collision $\nu = n_{\mathrm{LEBC}}/n_{\mathrm{coll}}$ as found for the billiard simulations (Fig. B.14). As the value of ν greatly influences the energy input it is not to

be expected that the stochastic model quantitatively reproduces the energy increase. The same applies via Eq. 3.11 or Eq. 3.12, respectively, to the diffusion coefficient. It should be noted that simply setting $\langle X \rangle = \nu$ does not solve the problem as this way the number of (subsequent) collisions is reduced instead of introducing consecutive Lees-Edwards boundaries. Furthermore the non-uniformity of the θ-distribution at the boundary would be affected by this approach.

Nevertheless, connecting the diffusion coefficient of the speed dynamics to the geometry-dependent quantity $\langle X \rangle$ and thus to the spatial diffusion in the Lorentz grid is an achievement: In the asymptotic scaling regime particle speeds are usually very large as compared to the shear speed. Thus, the Lorentz grid is hardly moving and results from the literature on spatial diffusion in the (non-sheared) Lorentz gas should apply. In [KD00] the authors discuss the effects of correlations and collisionless passing of symmetry cells onto the spatial diffusion coefficient. In [KD00, Fig. 1(a)] they find that the corrections increase the diffusion coefficient by about 50% for a triangular lattice with a gap size between scatterers of 0.3 radii. This quantitatively resembles the difference between Figs. 3.5/3.3 and Fig. 3.17. For lack of other explanations we also attribute the two different acceleration regimes found for the asymptotic thin-film billiard (Fig. 3.3) to correlations affecting the diffusion coefficient.

Note that the apparent underestimation of the deviation from the exponential energy distribution found in Figs. 3.15 and 3.16 is likely caused by comparing shear speeds instead of diffusion coefficients.

In the following we will not detail on this quantitative matter. Instead we concentrate on the scaling shape of the energy distribution and show that the stochastic process and consequently the billiard dynamics it models indeed corresponds to a generalized diffusion as proposed in Sec. 3.3.2.

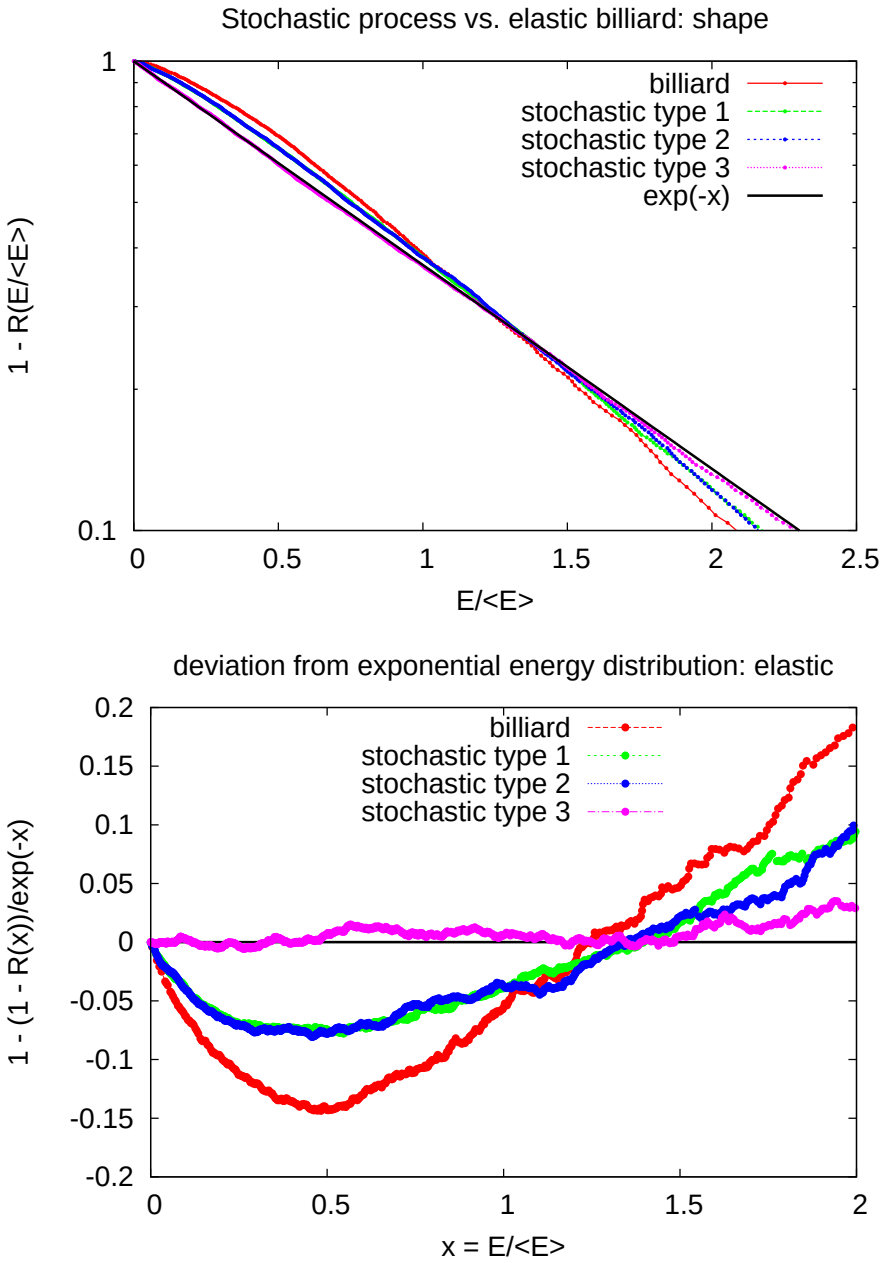

Figure 3.15: **Stochastic model vs. billiard simulations: Shape of elastic energy distribution for different model types.** The figure compares the rescaled cumulative energy distributions of three slightly different stochastic processes designed to model the billiard energy dynamics (see main text) are compared to the billiard simulations for the elastic case. The stochastic models differ in how the sequence of collisions and Lees-Edwards boundaries is determined (see main text). The energy distributions of processes 1 and 2 coincide. Qualitatively, their distributions show the same deviation from an exponential distribution as for the billiard simulations. The billiard simulations yield are stronger deviation, however, at least if the comparison is based on the shear speed s. Comparing diffusion coefficients instead might give a different picture. The type-3 stochastic process results in an exponential energy distribution. **Simulation details.** Energy distribution after $n_{\max} = 8 \cdot 10^4$ steps, $s = 2$, $\epsilon = 0$. For billiard data details see Fig. 3.11, the stochastic process was initialized with $N = 10^4$ initial energies distributed as $\exp(E/1000)$.

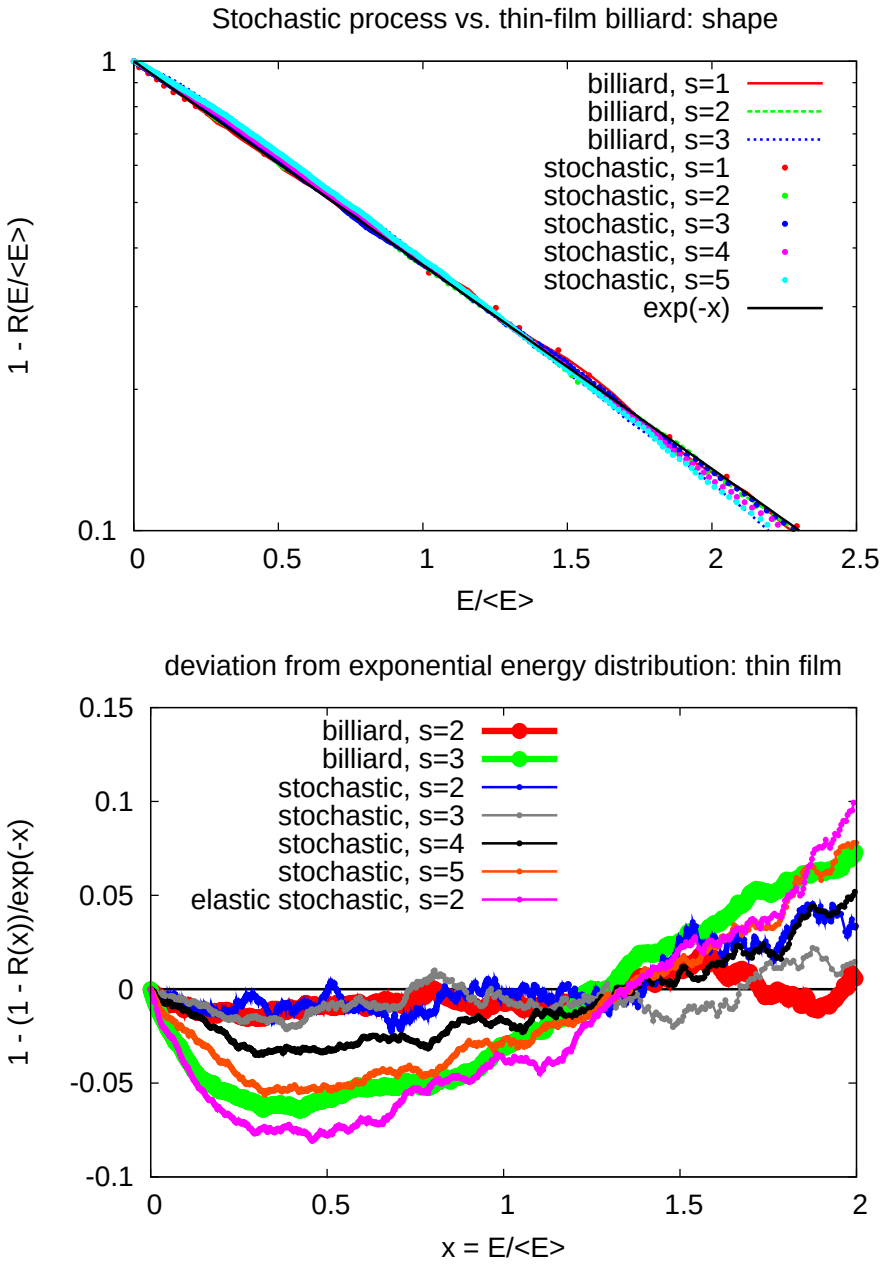

Figure 3.16: **Stochastic model vs. billiard simulations: Shape of thin-film energy distribution for different shear speeds.** The figure compares the energy distribution resulting from the stochastic process Eq. 3.22 designed to model the billiard energy dynamics and the billiard results for different shear speeds s. As observed for the deterministic billiard dynamics (Fig. 3.12) the liquid bridge dissipation brings the distribution closer to the exponential (compare pink and orange). Similar to the elastic case (Fig. 3.15), the stochastic model underestimates the degree of deviation (compare blue and turquois). The qualitative dependence of the deviation on s is however reproduced: It increases with increasing s. **Simulation details.** For billiard data details see Fig. 3.10. When comparing diffusion coefficients instead of shear speeds, low s in the stochastic process correspond to even lower s in the billiard (see main text). The noisy data is thus due to strong clustering. For $\epsilon = 1$ and $s > 2$ ($s = 2$) the stochastic process was initialized with $N = 1\,(4) \cdot 10^4$ initial energies distributed as $\exp(E/1000)$.

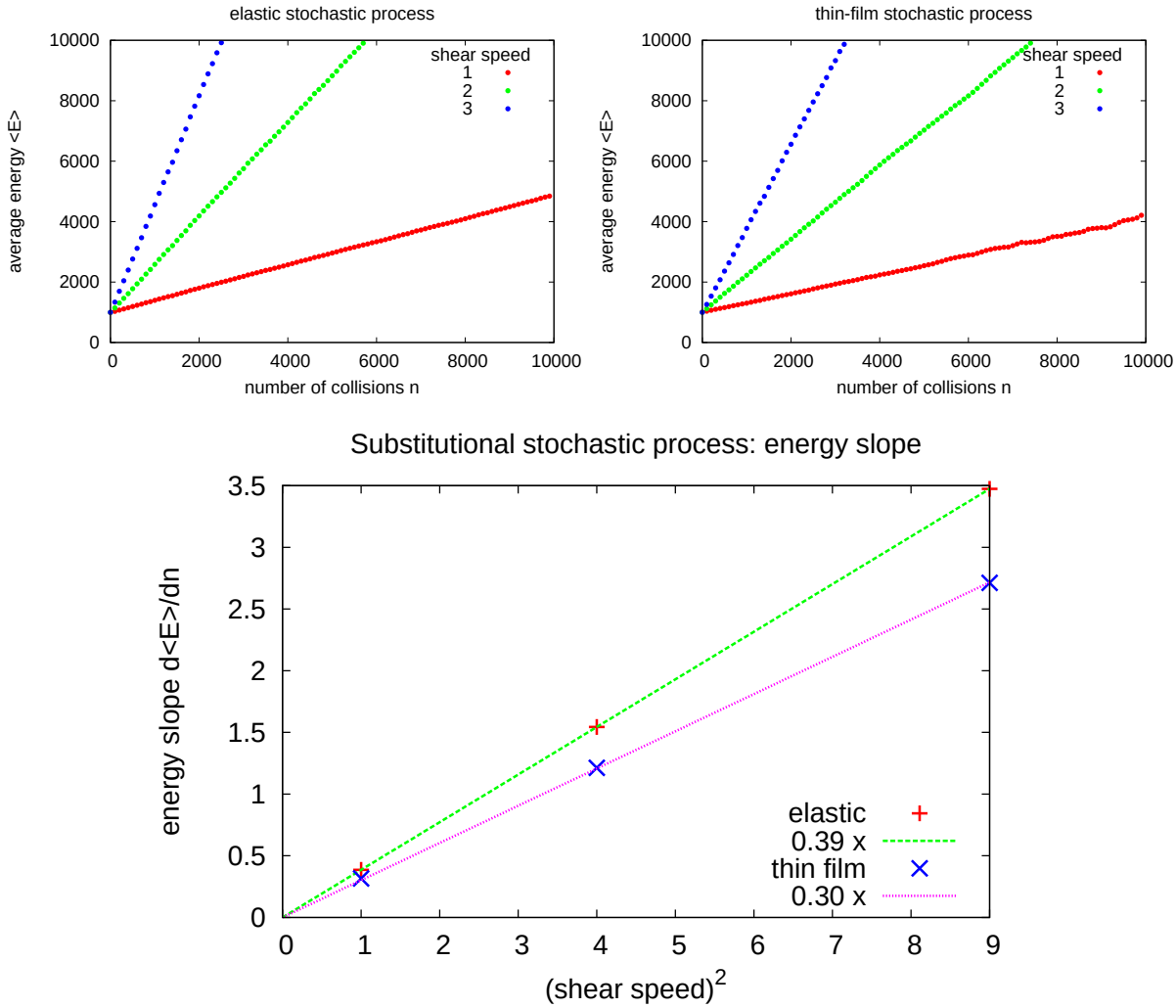

Figure 3.17: **Stochastic Process: Average energy development.** In addition to the stationary shape of the rescaled energy distribution the development of the average energy $\langle E \rangle$ is of interest. The figure shows that $\langle E \rangle$ grows linearly (top) with a slope that is asymptotically proportional to s^2 (bottom) for the elastic (top left) as well as for the thin-film (top right) stochastic process. (Note that the initial regime found for the billiard simulations in Figs. 3.3 and 3.5 is not observed due to initialization with an exponential distribution.) Thus, the stochastic model reflects the qualitative characteristics of the asymptotic energy development. It fails, however, in quantitative terms: The proportionality constants $c_{\text{thin}}^{\text{stoch}} \approx 0.3$ and $c_{\text{elastic}}^{\text{stoch}} \approx 0.4$ for the thin-film and elastic billiard, respectively, differ in value and ratio from the billiard values $c_{\text{thin}}^{\text{billiard}} \approx 0.6$ and $c_{\text{elastic}}^{\text{billiard}} \approx 0.5$ from Figs. 3.3 and 3.5. **Simulation details.** The stochastic model Eq. 3.22 was used with $\epsilon = 1$ for the thin-film case. It was initialized with $N = 10^4$ initial energies distributed as $\exp(E/1000)$ and propagated for $n_{\max} = 10^4$ collisions. For the thin-film data about 1000 systems survived up to $n_{\max}$. In the bottom plot asymptotic slopes obtained by fitting a linear function to the complete data set are displayed.

3.3.5 Drift and diffusion coefficients

The stochastic model process for the speed dynamics introduced in the last section is a generalized random-walk (cf. Sec. 3.3.1) with an absorbing boundary. The corresponding speed distribution can approximately be described by a Fokker-Planck equation (Eq. 3.6). Before solving the Fokker-Planck equation in Sec. 3.3.6 the transport coefficients need to be derived. Following Eqs. 3.7 and 3.8 the drift coefficient M and diffusion coefficient D are given by the first and second moment

$$\begin{aligned} M = \langle \Delta v \rangle &= \int (\Delta v)\ \rho_{v_{n+1}}(v_{n+1}|v_n)\,\mathrm{d}v_{n+1} = \int (\Delta v)\ \rho_\Theta(\theta|v_n)\,\mathrm{d}\theta &= \frac{1}{\pi}\int_0^\pi (\Delta v)\ \mathrm{d}\theta \\ D = \langle (\Delta v)^2 \rangle &= \int (\Delta v)^2 \rho_{v_{n+1}}(v_{n+1}|v_n)\,\mathrm{d}v_{n+1} = \int (\Delta v)^2 \rho_\Theta(\theta|v_n)\,\mathrm{d}\theta &= \frac{1}{\pi}\int_0^\pi (\Delta v)^2\,\mathrm{d}\theta \end{aligned}$$

of the speed increment from Eq. 3.22,

$$\Delta v := v_{n+1} - v_n = \sqrt{v_n^2 - 2\epsilon + \langle X\rangle\left(s^2 + 2sv_n\cos\Theta\right)} - v_n.$$

Note that the calculation of the expectation values is simplified by using the transition probability density ρ_Θ that was found to be uniform (Sec. B.2) and that Θ was assumed to be independent of v when deriving the process. To facilitate the calculation, Δv is expanded for $v \gg 1$. This step is well justified as the Fermi acceleration quickly results in average speeds that are large compared to the shear speed s. Naturally, this approximation does not model clustering properly. This is no real loss of predictive power, however, as the stochastic model severely approximates clustering anyway. The approximate increment reads

$$\Delta v = -\frac{\epsilon}{v} + \frac{\langle X\rangle s^2}{2v} + s\langle X\rangle\cos\theta - \frac{\langle X\rangle^2 s^2\cos^2\theta}{2v} + \mathcal{O}\left(\frac{1}{v^2}\right),$$

so that the resulting coefficients are (up to $\mathcal{O}(v^{-2})$):

$$M = \frac{\frac{\langle X\rangle}{2}s^2 - \frac{\langle X\rangle^2}{4}s^2 - \epsilon}{v}, \qquad D = \frac{\langle X\rangle^2}{2}s^2. \tag{3.23}$$

The coefficients depend on ϵ as well as on s and via $\langle X\rangle$ and Eq. 3.21 on R and L so that all billiard parameters are included. They follow the form predicted in Sec. 3.3.2.

We remark that the property of the diffusion coefficient to be constant motivates the preference for the speed v above the energy $E = v^2/2$ as variable for the Markov process. In fact, the corresponding energy process results in an energy-independent drift coefficient M_E while the diffusion coefficient D_E becomes energy-dependent:

$$M_E = \frac{\langle X\rangle}{2}s^2 - \epsilon, \qquad D_E = \left(\frac{\langle X\rangle}{2}s^2 - \epsilon\right)^2 + \frac{\langle X\rangle^2 s^2}{2}E \sim E.$$

3.3.6 Fokker-Planck equation

As the Fokker-Planck equation is a continuous-time approximation to the master equation describing the generalized random-walk Eq. 3.22 (cf. Sec. 3.3.1), the number of collisions n passes over to a continuous time t. With the drift coefficient $M =: \mu/v$ and the diffusion coefficient D as derived in the last section the Fokker-Planck equation for the distribution function, i.e. the relative number density, of non-clustered systems, $n(v,t)$, which corresponds to the energy distribution $\rho_{\langle E\rangle}(E)$, reads:

$$\begin{aligned}\partial_t n(v,t) &= -\partial_v\left(\frac{\mu}{v}n(v,t)\right) + \frac{D}{2}\partial_v^2 n(v,t)\\ &= -\frac{\mu}{v}\partial_v n(v,t) + \frac{D}{2}\partial_v^2 n(v,t) + \frac{\mu}{v^2}n(v,t).\end{aligned} \tag{3.24}$$

Due to clustering, $n(v,t)$ is "normalized" to the relative number of systems remaining unclustered, $N(t)/N(1)$. For the elastic case (bridge rupture energy $\epsilon = 0$), no clustering occurs so that $N(t) = N(1)$ while for the thin-film billiard clustering can only decrease the particle number:

$$\frac{N(t)}{N(1)} = \int_0^\infty n(t,v)\,\mathrm{d}v \leq 1 \quad \text{with} \quad \partial_t N(t)\begin{cases}=0 & \epsilon = 0\\ <0 & \text{else}\end{cases}, \qquad \lim_{v\to\infty} n(v,t) = 0, \tag{3.25}$$

As the transport coefficients were derived assuming $v \gg s$ and even diverge for $v \to 0$ also the above partial differential equation only provides a proper description in this regime. In particular, it is unclear whether it properly accounts for the absorbing boundary at zero or close to zero, for the elastic or thin-film billiard, respectively. This problem is avoided by a *scaling ansatz* that conveniently reduces the partial differential equation Eq. 3.24 to an ordinary differential equation, which implicitly accounts for the absorbing boundary condition. Figures 3.10 and 3.11 suggest $x := E/\langle E\rangle = v^2/(2kDt)$ as scaling variable where the second equality is due to Eq. 3.12. To account for the absorbing boundary, i.e. clustering, assuming $N(t)/N(1) \propto t^{-\gamma}$ seems asymptotically appropriate in the light of Fig. 3.8. Note that this factor is hidden in Figs. 3.10 and 3.11 due to the enforced normalization. With $\alpha = -(1/2+\gamma)$ to ensure "normalization" according to Eq. 3.25 the ansatz

$$n(v,t) = t^\alpha f\left(\frac{v^2}{2kDt}\right) \qquad \text{with} \quad \alpha\begin{cases}=-\frac{1}{2} & \epsilon = 0\\ <-\frac{1}{2} & \text{else}\end{cases} \tag{3.26}$$

reduces Eq. 3.24 to an ordinary differential equation in $f(x)$:

$$0 = \partial_x^2 f + \left(k + \frac{1-2G}{2x}\right)\partial_x f - \left(\frac{G}{2x^2} + \frac{k\alpha}{x}\right) f, \qquad G := \frac{\mu}{D}. \tag{3.27}$$

With this and Eq. 3.23 f only depends on

$$G = \frac{\mu}{D} = \frac{1}{\langle X\rangle} - \frac{2\epsilon}{\langle X\rangle^2 s^2} - \frac{1}{2},$$

which is via $\langle X\rangle$ (Eq. 3.21) connected to the billiard geometry. For the elastic billiard with $\epsilon = 0$ the ordinary differential equation does only depend on the billiard geometry

and is independent of the shear speed s. For this case s enters the solution only via normalization. The scaling solution f inherits its normalization from n, i.e. (Eq. 3.25):

$$t^{-\gamma} = \frac{N(t)}{N(1)} = \int_0^\infty n(v,t)\,\mathrm{d}v = t^{-\gamma}\sqrt{\frac{kD}{2}}\int_0^\infty \frac{f(x)}{\sqrt{x}}\,\mathrm{d}x \quad \Rightarrow \quad 1 = \sqrt{\frac{kD}{2}}\int_0^\infty \frac{f(x)}{\sqrt{x}}\,\mathrm{d}x. \tag{3.28}$$

The constant k that connects the coefficient of diffusion to the average energy is determined by

$$2Dkt = 2\langle E\rangle = \langle v^2\rangle = \int_0^\infty v^2\tilde{n}(v,t)\,\mathrm{d}v \Longrightarrow 1 = \sqrt{\frac{kD}{2}}\int \sqrt{x}\tilde{f}(x)\,\mathrm{d}x \tag{3.29}$$

where $\tilde{n}(v) = n(v)\cdot N(1)/N(t)$ and accordingly (cf. Eq. 3.28) $\tilde{f}(x) = t^\gamma f(x)$ have been introduced to obtain probability densities for the averages.

As the dependence of the survival/clustering exponent γ on the parameters is unknown we only discuss the solution of Eq. 3.27 and Eq. 3.24, respectively, for the elastic case. In the next section an expression for γ will be derived. This expression depends on the energy distribution $\rho_{\langle E\rangle} = \tilde{n}$, however, so that it would be of little practical use in the present context. For the elastic billiard, i.e. $\epsilon = 0$ and $\alpha = -1/2$, we find with the help of MATHEMATICA that the integrable part of the general solution to Eq. 3.27 is given by

$$f(x) = \sqrt{\frac{2}{D}}\cdot\frac{k^G}{\Gamma\left(G+\frac{1}{2}\right)}\cdot x^G\cdot \mathrm{e}^{-kx} \tag{3.30}$$

We use Eq. 3.29 for a billiard geometry of $R = 1$ and $L = 3$ to compare this solution to the simulations from Sec. 3.3.4. Keeping in mind $\epsilon = 0$ for the elastic case, values $G \approx 0.78$ and $k = 1.28$ result. Thus, the energy is expected to grow as

$$\frac{\langle E\rangle}{t} = Dk = \frac{1}{2}\langle x\rangle^2\cdot k\cdot s^2 \approx 0.39\cdot s^2,$$

which perfectly corresponds to Fig. 3.17. To compare the shape of Eq. 3.30 to the simulations (cf. Fig. 3.15, types 1 or 2, respectively) it is necessary to keep in mind that the data has been normalized. Thus the corresponding probability density is

$$\rho_{\langle E\rangle}(x) = \sqrt{\frac{kD}{2}}\frac{f(x)}{\sqrt{x}} \qquad \text{with} \qquad \int_0^\infty \rho(x)\,\mathrm{d}x = 1,$$

which does not depend on $D \propto s^2$ due to Eq. 3.28. The cumulative distribution function $R(x)$ displayed in Fig. 3.15 is for $G \approx 0.78$ and $k = 1.28$ expected to be

$$R(y) = \int_0^y \rho(x)_{\langle E\rangle}\,\mathrm{d}x = \tilde{\Gamma}(1.28, 1.28y), \tag{3.31}$$

where $\tilde{\Gamma}(a,x) = \frac{1}{\Gamma(a)}\int_0^x t^{a-1}e^{-t}\,\mathrm{d}t$ is the normalized lower incomplete Γ-function. Figure 3.18 shows that the shape of the energy distribution is well described. Also, the (normalized) simulation results are indeed independent of the shear speed s. We stress that this is a feature specific to the elastic case: For $\epsilon > 0$ Eq. 3.27 does depend on s and

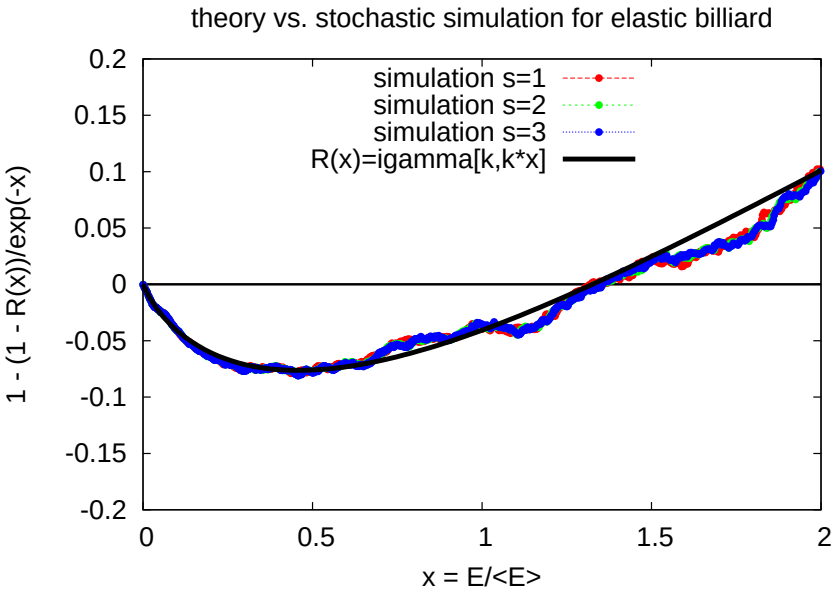

Figure 3.18: **Simulation vs. Fokker-Planck equation for the stochastic model of the elastic sheared billiard.** For the elastic case the Fokker-Planck equation describing the stochastic model of the billiard dynamics results in the scaled energy distribution Eq. 3.30. The plot compares the normalized cumulative distribution $R(x)$ of this solution (Eq. 3.31) to simulation results obtained from the type-2 stochastic process as in Fig. 3.15. Analytic solution and simulation results fit very well. The normalized $R(x)$ is independent of s as expected(see main text).

ϵ. Consequently, also the shape of the energy distribution is expected to vary with this parameters as observed in Fig. 3.16.

The Fokker-Planck equation 3.24 discussed so far describes the elastic and the thin-film sheared billiard. It can, however, easily be adapted to the thick-film interaction. The main difference between the thin- and thick-film thin-thread model relevant for the energy distribution lie in the clustering behavior (Eq. 2.12): While for the thin-film billiard clustering is restricted to a boundary region the thick-film billiard features bulk-absorption. This can be accounted for by an explicit absorption term $A(v)$, which is added to Eq. 3.24. The absorption A is given by the clustering probability Eq. 3.32. Expanding for large speeds yields:

$$A(v) = 1 - \sqrt{1 - \frac{2}{v^2}} \overset{v^2 \gg 1}{\approx} \frac{1}{v^2}$$

Thus, Eq. 3.24 changes only slightly to become

$$\partial_t n(v,t) = -\frac{\mu}{v}\partial_v n(v,t) + \frac{D}{2}\partial_v^2 n(v,t) + \frac{\mu - 1}{v^2} n(v,t),$$

which does not harm the scaling ansatz.

In conclusion, we recall that the analytic treatment of the energy dynamics found in the sheared billiards discussed so far holds in the asymptotic regime $v \gg 1$. To describe the boundary region, $v \sim 1$, the transport coefficients (cf. Sec. 3.3.5) and thus the Fokker-Planck equation need to be approximated in this limit case. In the boundary regime,

scaling behavior is not a priori expected, which would complicate the solution to the Fokker-Planck equation. In any case, such an approach will only give qualitative results due to the very rough clustering condition underlying the stochastic process in Sec. 3.3.4.

3.4 Clustering and power-law lifetime distribution

Figure 3.7 (bottom) demonstrates that clustering occurs despite of high average energies caused by the Fermi acceleration. At first sight this is surprizing. However, assuming ergodicity it is reasonable for a broad energy distribution like the exponential-type distributions that have been found in Figs. 3.10 and 3.11 and were explained in the previous sections: For an exponential distribution the standard deviation σ_E increases like the average (Fig. 3.7, top),

$$\langle E\rangle = \sigma_E \propto n$$

Unexpectedly for a strongly chaotic system the lifetime distribution of non-clustered systems is found to decay with a power-law tail (Fig. 3.8) and not exponentially as in the standard setting (Sec. 2.1.3). Also the exponential was in principle observed for the freely-cooling case (Sec. 2.4). When on the other hand adjusting the argument in Sec. 2.1.3 to the situation of an unbound phase space as present in the sheared billiard,the power-law decay occurs naturally: As the effectively occupied phase space is growing as $\langle E\rangle \propto n$ the relative size of the fixed clustering region is decreasing. The measure of this leak, i.e. the decay rate κ is obtained by applying the phase-space distribution (Sec. 3.2.2),

$$\rho\left(\theta, b, \Delta, E\right) \mathrm{d}\theta\, \mathrm{d}b\, \mathrm{d}\Delta\, \mathrm{d}E = \frac{\mathrm{d}\theta}{2\pi}\frac{\mathrm{d}b}{2}\frac{\mathrm{d}\Delta}{L}\rho_{\langle E\rangle}\left(E\right)\mathrm{d}E,$$

to the clustering region (Sec. 2.3),

$$\begin{aligned}[0,2\pi]\times([-1,-b_\mathrm{c}(E)]\cup[b_\mathrm{c}(E),1])\times[0,L]\times[0,E_\mathrm{c}],\\ b_\mathrm{c}(E)=\begin{cases}0 & E<1\\ (1+s_c)\sqrt{1-\frac{1}{E}} & 1<E<E_\mathrm{c}\end{cases},\end{aligned} \tag{3.32}$$

and reads:

$$\kappa\left(n\right) = \int_0^{E_\mathrm{c}}\left(2\int_{b_\mathrm{c}(E)}^1\frac{\mathrm{d}b}{2}\right)\rho_{\langle E\rangle}(E)\,\mathrm{d}E = \int_0^{E_c}\left[1-b_c\left(E\right)\right]\rho_{\langle E\rangle}(E)\,\mathrm{d}E.$$

At this point a problem arises: In the above calculation the energy distribution for low energies is needed. The considerations in the previous chapter were approximations for high energies, however, and the numerical results do not have high enough accuracy in the low-energy regime either. It is not even clear whether the scaling behavior strictly applies in the boundary region of low energy.

Therefore, a uniform energy distribution $\rho_{\langle E\rangle}(E) = 1/\langle E\rangle = 1/(Dn)$ is assumed to demonstrate the principle: It leaves the integral to be some $\langle E\rangle$-independent constant c and gives the decreasing decay rate,

$$\kappa_0\left(n\right) = \frac{c}{Dn} = \frac{\gamma}{n}, \qquad \frac{1}{\gamma}\propto D\propto s^2, \tag{3.33}$$

which results in a power-law decay of the number of non-clustered systems N:

$$\dot{N}(n) = -\kappa_0(n)\,N(n) \qquad \Rightarrow \qquad \frac{N(n)}{N_0} = \exp\left(-\int_1^n \kappa_0(n')\,\mathrm{d}n'\right) = n^{-\gamma}.$$

The picture remains qualitatively unchanged when using the low-energy approximation of the scaling exponential energy distribution (Eq. 3.4) with $\langle E\rangle = Dt$ (Eq. 3.14),

$$\rho_{\langle E\rangle}(E) = \frac{1}{Dn}\exp\left(-\frac{E}{Dn}\right) \approx 1 - \frac{E}{Dn},$$

which results in:

$$\kappa_1(n) = \frac{c_1}{Dn} + \frac{c_2}{D^2n^2} \overset{n\gg\frac{c_2}{c_1D}}{\approx} \frac{c_1}{Dn}, \qquad \frac{1}{\gamma} \propto D \propto s^2. \tag{3.34}$$

From these considerations (cf. Eqs. 3.33 and 3.34) the survival exponent γ is expected to respect the condition: $\gamma \cdot s^2 = \text{const}$. Figure 3.9 (bottom, red symbols) shows that this is indeed the case for low shear speeds but does not hold for high s. A possible explanation for this finding is based on the size of the clustering region relative to the boundary region in which the energy distribution is unknown: For very small s, i.e. slow acceleration, the clustering region is still large enough to be properly modeled by the asymptotic energy distribution while for large s it is so small that neglecting the special situation at the boundary just fails. A second possibility to explain Fig. 3.9 is that it simply does not show the true survival exponent because the very small clustering region is insufficiently sampled for high s. Both considerations might be backed by noting that the high and low energy regime are separated by the initial critical value s_c^0 (Eq. 3.15), which discriminates cases where the drift is pushing towards or away from the boundary. Furthermore it is interesting to note that the survival exponent of the thick-film model shows a uniform behavior (Fig. 3.9, bottom, green symbols). In the context of the present discussion this is reasonable since clustering is not restricted to a confined boundary region here (Eq. 2.12).

Chapter 4

Summary and outlook

The freely-cooling wet billiard is a very unusual dissipative dynamical system:

- The piecewise-Hamiltonian dynamics results in a switching of energy shells that corresponds to a homogenous rescaling of phase space.
- The wet interaction according to thin-film models is non-injective.
- This non-injectivity causes a double-folding of the phase space, which results in a fractal natural distribution.

It seems not appropriate to place the double-folding in the usual line of dissipative dynamics where dissipation contracts phase space and thus represents irreversibility. These expectations are already satisfied by the homogenous rescaling. The non-injectivity caused by the hysteresis of the thin-thread model constitutes a new element that is not a pathology of the model but inherent to the physics of wet granular matter. Nevertheless, conservation of angular momentum I presumably requires such hysteretic interactions to be dissipative: Next to spatial splitting of the interaction event into collision and bridge rupture, the non-injectivity requires an increase of the impact parameter b, which has to be compensated by a decrease in speed v:

$$I = v \cdot b \mapsto I' = v' \cdot b', \quad \partial_t I = 0 \text{ and } b' > b \Rightarrow v' < v$$

The standard theory of dynamical systems is mainly developed for injective maps and is thus not a priori applicable to the wet billiard. For example, the sum of the Lyapunov exponents as a measure of phase space compression (e.g. [Eck85, Sec. III.D.1]) will in the case of the wet billiard only account for the general rescaling of phase space but not for the double-folding. The apparent symplecticity of the wet interaction [HF07, Sec. 4.6] probably emerges for similar reasons. Consequently, when working with dynamical systems that include wet interactions, standard tools should not be trusted without additional care.

Furthermore, the freely-cooling wet billiard indicates that the challenges in formulating the statistical mechanics of wet granulates do not primarily emerge on the microscopic level of the phase space distribution:

- The wet Sinai billiard is strongly chaotic.

- In spite of phase space structure the natural distribution is supported on the whole energy surface.
- Projections of the natural distribution are uniform.
- For the purpose of calculating averages of smoothly varying observables, a uniform distribution on the energy surface is a good assumption as illustrated for the clustering probability.

Being strongly chaotic on the complete surface determined by its current energy, the wet billiard fulfills the basic assumptions of statistical physics. After having confirmed these basic properties, a possible next step could be to set up a Boltzmann equation for the wet granular gas that takes the hysteresis into account. In a previous approach [Röl10, Appendix A] to the Boltzmann equation of wet granular matter the hysteresis has been neglected so that the wet interaction reduces to an energy-dependent coefficient of restitution. The results presented in this thesis should form a good basis to approach the hysteresis. In the context of the Boltzmann equation it should be mentioned that in view of Appendix B.1 the same corrections due to post-collision correlations as found for the dry granular gas [PBS03] are to be expected for the wet granular gas.

The sheared wet billiard combines two effects that are of considerable interest in dynamical-systems research:

- The application of Lees-Edwards boundary conditions to the Sinai billiard results in Fermi acceleration. The diffusion coefficient of the energy dynamics is connected to the well-studied diffusion coefficient of spatial motion. Correlations caused by the billiard geometry increase the diffusion coefficient in comparison to the correlation-free case.
- The sheared wet billiard is an interesting new example of a transiently chaotic system in which Fermi acceleration results in an algebraic lifetime distribution.

Finding Fermi acceleration in the sheared Sinai billiard is well in line with [LRA99] where the authors study Fermi acceleration in the periodic Lorentz gas with infinite horizon (Sec. 1.2.2) and radially expanding and contracting ("breathing") scatters. For periodically perturbed boundaries, in particular, correlations are observed. The origin of these correlations, however, is different from the correlations in the sheared system. In this context it seems interesting to explore what causes the correlations that have recently been found by Vollmer and Oliveira in a Lorentz gas with periodically vibrating scatters (see Appendix B.5).

Opening up other systems experiencing Fermi acceleration such that they become transiently chaotic would be interesting to check generality of the algebraic lifetime distribution. In particular, the structure of the chaotic saddle deserves further investigation. It should be rather atypical as the exits do not, at least not in a typical way, emerge from a boundary crisis. In this respect, higher-dimensional systems should also be taken into consideration as for a random walk in $d > 2$ dimensions the return probability to the origin, i.e. the low-energy clustered state, is no longer unity.

In conclusion, the sheared wet billiard in itself is an interesting problem in dynamical-systems research. Extending the results obtained for the two-disk system to realistic many-particle wet granulates, however, poses a number of questions and restrictions that will have to be clarified in follow-up studies:

- **Fermi acceleration.** Due to Fermi acceleration particle speeds are expected to quickly reach regions where the velocity-independent dissipation caused by the wet interaction can be neglected in comparison to the high kinetic energies so that only assuming elastic collisions would be sufficient. When modelling wet granular matter such that the model compares to experiments, however, the effects of inelasticity of collisions cannot be neglected for high impact speeds (Sec. 1.1.2, [Röl10, Sec. 3.3]). Thus the inelasticity of collisions is expected to soon dominate dissipation, prevent Fermi acceleration and ensure a steady-state according to Sec. 3.3.3.

- **Steady-state condition.** The sheared wet billiard has a trivial collision frequency. Thus an important adjustable value is missing in the energy balance as compared to many-particle systems. Consequently, the arguments given to explain the absence of a steady-state in the billiard are not directly extendable. We note that this restriction of the billiard system cannot be solved by considering real time instead of the number of collision: Considering real time corresponds to weighting individual trajectories according to their free-flight time and thus basically reflects the billiard geometry; the absence of a meaningful collision frequency is rather a restriction of the few degrees of freedom in the billiard system. The minimal model that allows for a dynamical collision frequency requires at least three disks. In this setting correlations of the collision dynamics and in particular clustering affect the mean free-path such that it is changing in the course of time.

- **Clustering.** The freely-cooling wet billiard allows to study the probability of two wet particles to cluster in a collision with a certain kinetic energy (cf. Sec. 2.4). In [UAR+09, UAZ+09] this quantity is used when determining the temperature evolution in a simulated wet many-particle system (cf. Sec. 1.1.4). For the sheared wet billiard, on the other hand, the observation that clustering follows a power-law distribution cannot immediately be applied for many-particle systems: Future work will have to clarify whether the power-law is a peculiarity of the two-disk system or has consequences also when a two-particle cluster might break up in collisions with a third particle.

The restriction of not taking into account three-particle interactions can be relaxed by considering a high-density sheared Lorentz gas. If the ratio of radius R, box size L and bridge rupture distance s_c is chosen such that $R < L/2 < R+s_c$, Lees-Edwards boundaries are still applicable as neighboring rows can pass each other but the point particle may form bridges with two different neighbors at a time, which allows to cross boundaries and regain energy although in the clustered state. So far it is unclear, however, what happens to the ratio of boundary crossings and bridge ruptures in this setting and if strong correlations between these events and the position of the scatterers occur.

In summary, the presented study of the freely-cooling wet billiard lays a solid foundation for kinetic theories of wet granular matter. The sheared wet billiard exhibits fascinating effects whose generalization to many-particle systems requires to extend the analysis of this thesis from two to three disks.

Appendix A

Simulation details

Software. All numerical simulations were realized using the C programming language and may be obtained from the author. For all graphical displays the GNUPLOT Software was used.

Parameter values. The following default parameters have been used for the simulations if not mentioned otherwise:

scatterer radius	$R =$	1	(cf. Fig. 1.6)
billiard box size	$L =$	3	(cf. Fig. 1.6)
bridge rupture distance	$s_c =$	0.1	(cf. Fig. 1.1)
bridge rupture energy	$\epsilon =$	1	(cf. Fig. 1.1)
coefficient of restitution	$\alpha =$	0.5	(cf. Eq. 2.8)
initial position of Lees-Edwards boxes	$\Delta =$	$L/2$	(cf. Fig. 3.1)

Verification. In addition to automatized functionality tests of all subroutines and manual verification of individual trajectories by visualizing, phase-space distributions were also verified with regards to symmetries and the reproduction of known results: The natural distribution of the freely-cooling billiard is symmetric with respect to $\pi/2$-rotations as well as inversion symmetric, while the sheared billiard is only symmetric with respect to rotations through π. For the freely-cooling billiard the expected uniform distribution was obtained for $\epsilon = 0$ and the freely-cooling case is retained for $s = 0$ in the sheared system.

Appendix B

Graphical material

B.1 Phase space of freely-cooling billiards

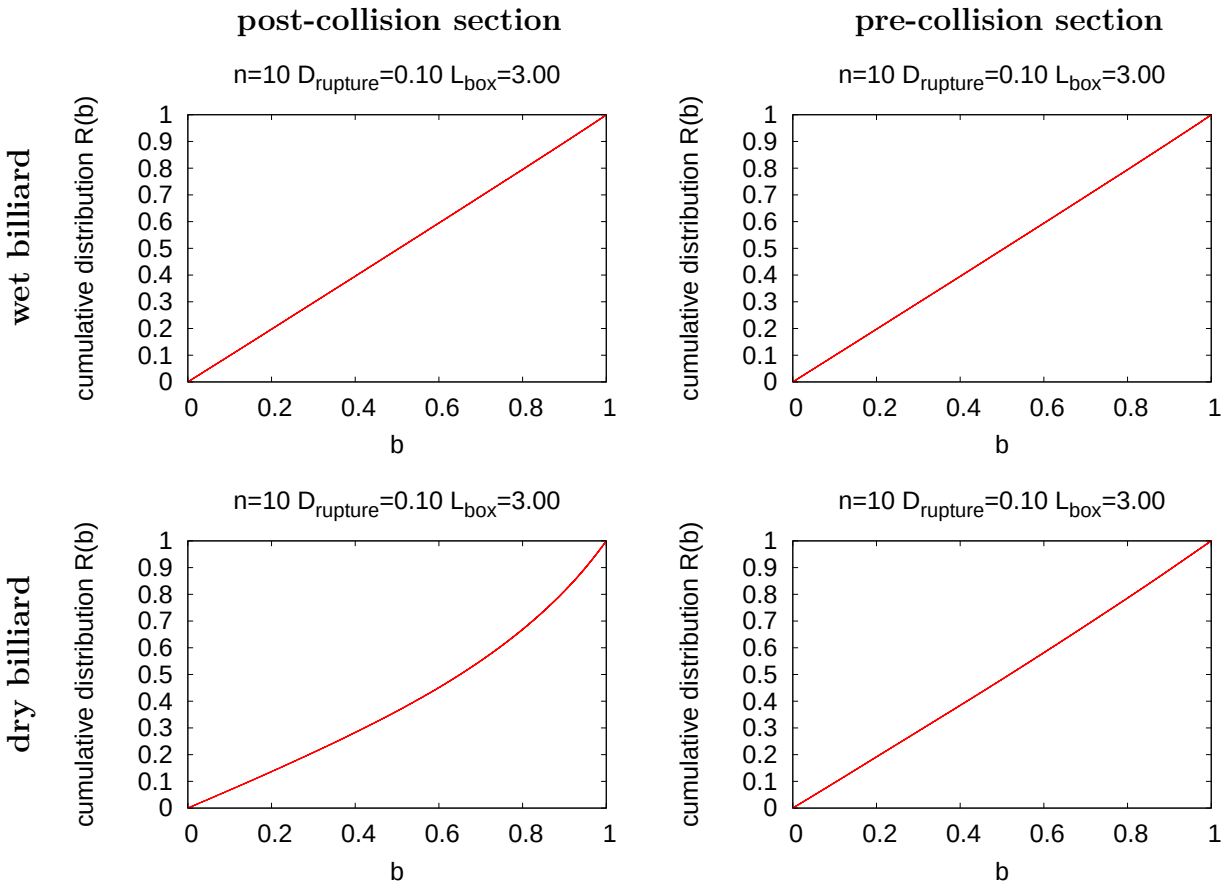

Figure B.1: **Projections of the natural distribution onto the b-axis for the (thin-film) wet and dry freely-cooling billiard.** For the dry billiard an overpopulation of large impact parameters b is observed in the post-collision Poincaré section (bottom left). This finding corresponds to [PBS03] and occurs because b always decreases in a collision (Eq. 2.8). In the pre-collision section (bottom right) the correlation is absent due to the chaotic dynamics in between collisions. For the wet billiard Eq. 2.7 indicates that an overpopulation of high impact parameters should be observed. This would, however, only be the case in a "post-bridge" section. The pre- as well as the post-collision sections (top) are both "pre-bridge" sections so that the chaotic dynamics has blurred the correlations resulting from the last bridge. **Simulation details.** Note that the symmetry reduced phase space distribution is used (cf. Sec. 2.2). Apart from mentioned, default parameters were used (cf. Appendix A).

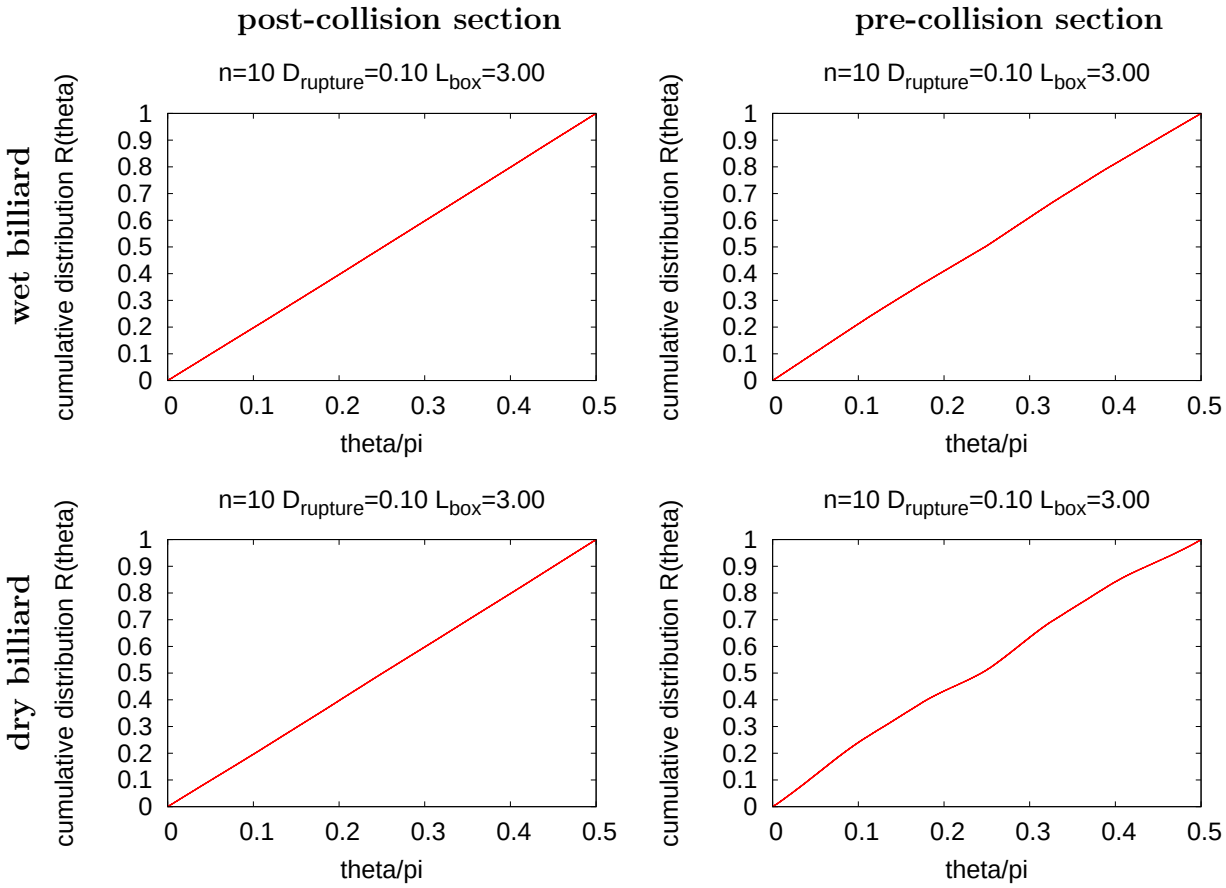

Figure B.2: **Projections of the natural distribution onto the θ-axis for the (thin-film) wet and dry freely-cooling billiard.** In the post-collision Poincaré section the wet as well as the dry billiard show uniform projections. In the pre-collision section, however, the dry billiard shows overpopulation at $\theta \approx 0, \pi/4, \pi/2$. This is probably due to the billiard geometry as illustrated in Fig. 2.11. For the wet billiard this structure might be guessed but is hardly visible. **Simulation details.** Note that the symmetry reduced phase space distribution is used (cf. Sec. 2.2). Apart from mentioned, default parameters were used (cf. Appendix A).

B.2 Phase space of sheared billiards

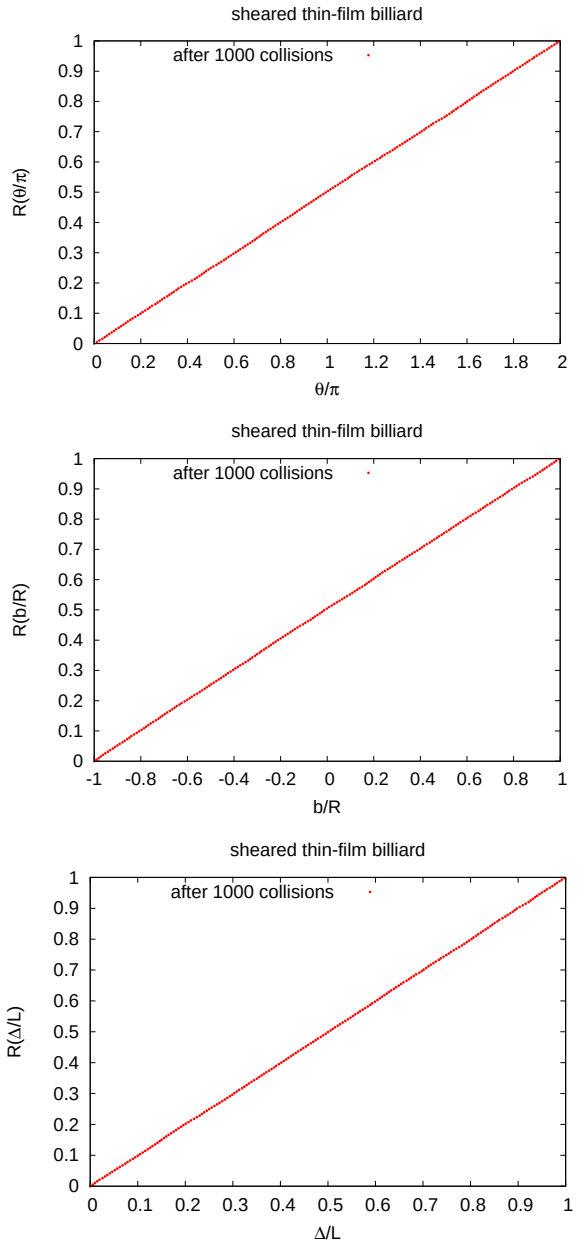

Figure B.3: **Cumulative distribution functions R of phase space projections on b-, θ- and Δ-coordinate for the sheared thin-film billiard.** While the phase space projection on the energy coordinate relaxes towards an almost exponential distribution (Fig. 3.10) the projections onto the θ- (top), b- (middle) and Δ-coordinate (bottom) result in uniform distributions. **Simulation details.** Only the remaining non-clustered system out of $2 \cdot 10^4$ initial conditions with an initial energy E_{ini} distributed as $\exp(-E/10^4)$ are considered. The distribution function is normalized to the number of remaining non-clustered systems. Apart from mentioned, default parameters were used (cf. Appendix A).

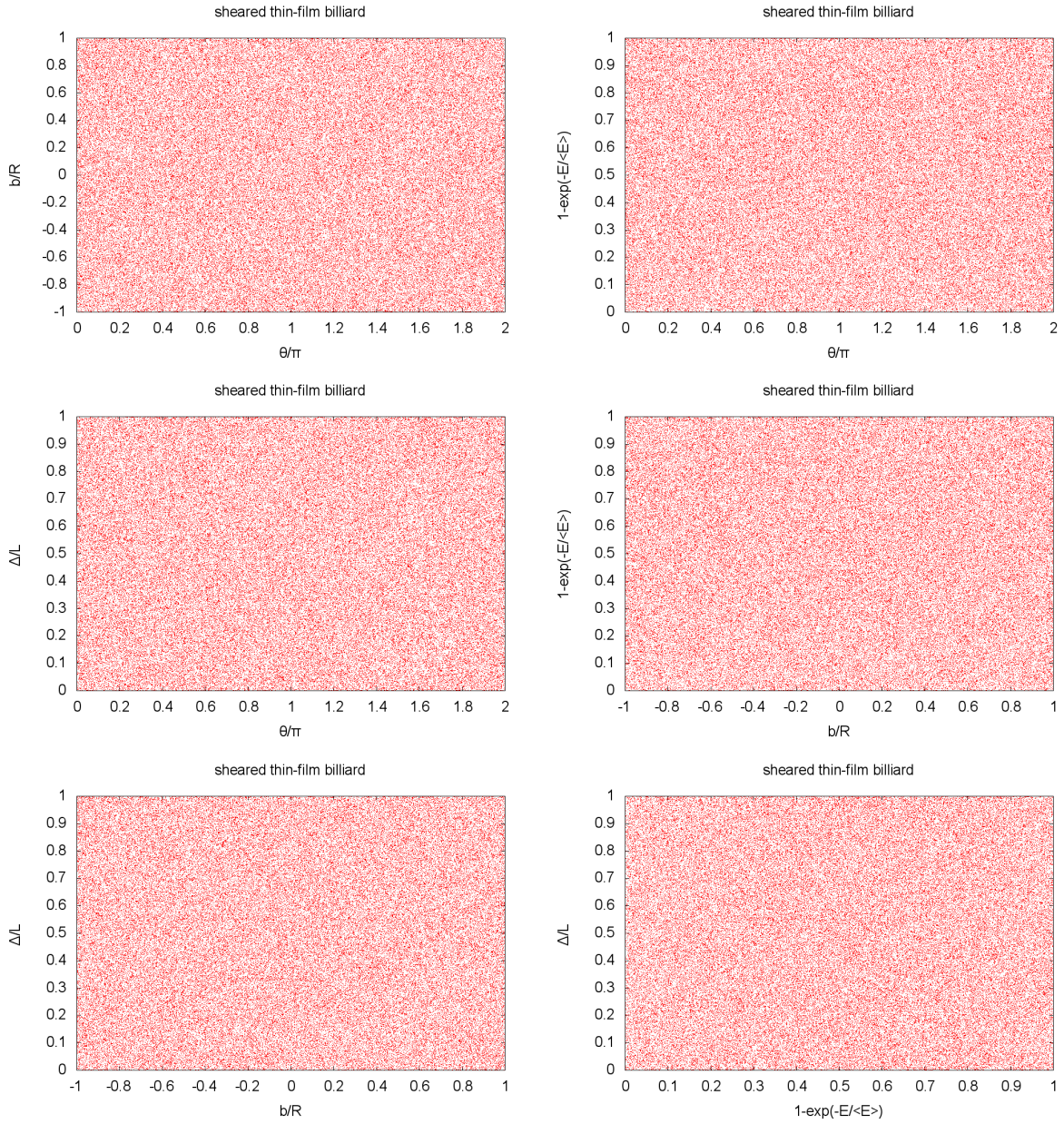

Figure B.4: **2-dimensional phase space projections for the sheared thin-film billiard.** Shown are the six 2-dimensional projections of the 4-dimensional phase space in the asymptotic scaling regime $n \gg 1$, $E \gg 1$. Assuming $E \sim \exp(-E/\langle E \rangle)$ (see Fig. 3.10) the energy values have been transformed to yield a uniform distribution. The 2-dimensional projections show no structure. **Simulation details.** Only the remaining non-clustered system out of $2 \cdot 10^5$ initial conditions with an initial energy E_{ini} distributed as $\exp(-E/10^4)$ are plotted after $n = 1e5$ collisions. Apart from mentioned, default parameters were used (cf. Appendix A).

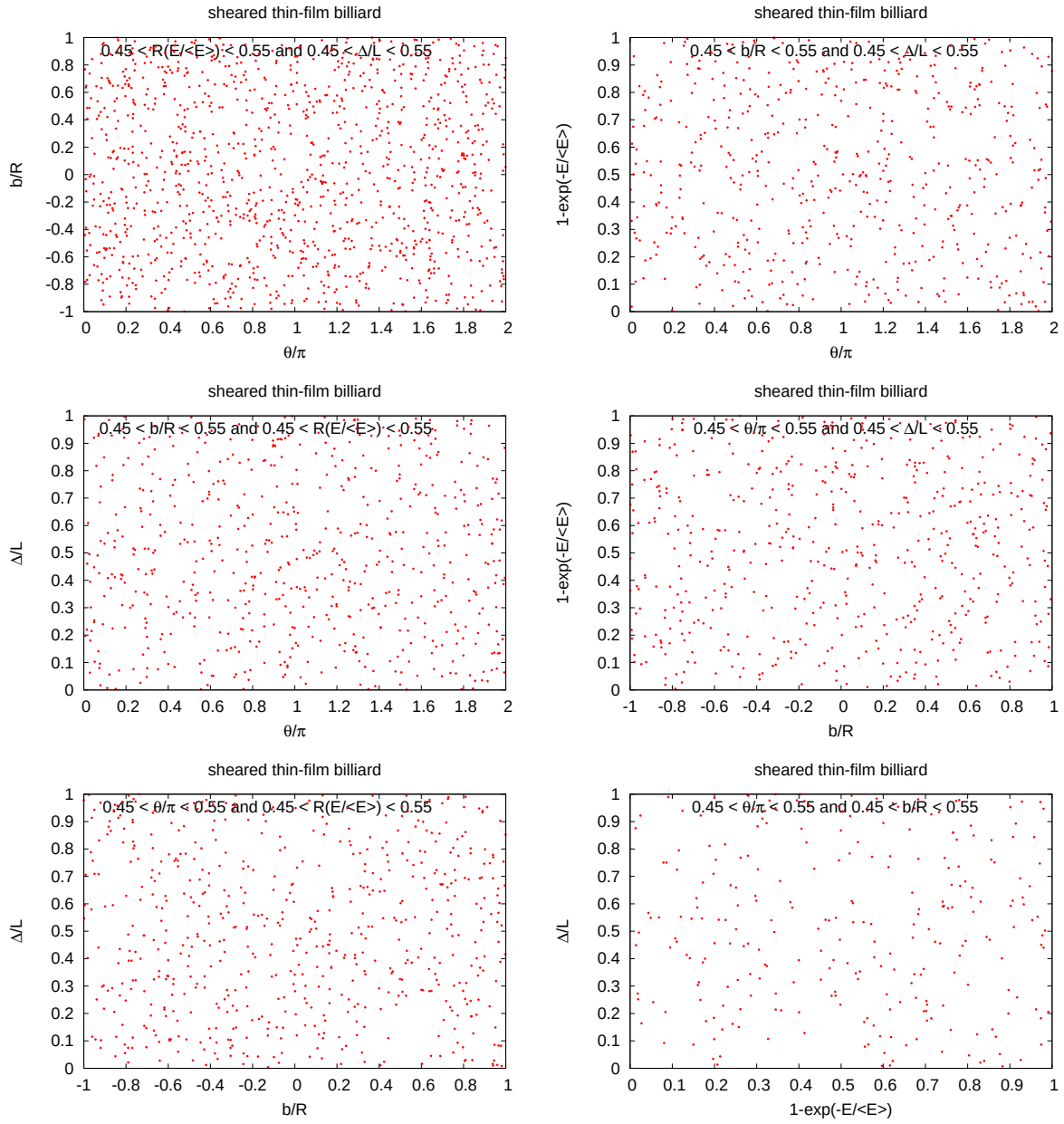

Figure B.5: **2-dimensional phase space sections for sheared thin-film billiard.** To prevent averaging out of possible phase space structure by projection some phase space sections are shown. Together with the uniformity of the 1-dimensional and 2-dimensional projections (Figs. B.3 and B.4) they propose that the phase space of the sheared thin-film billiard is not significantly structured in the asymptotic scaling regime $n \gg 1$, $E \gg 1$. If found in the indicated phase space region the state of non-clustered systems is plotted after $n = 10^5$ collisions. The number of dots may vary as the regions have different measures. $2 \cdot 10^5$ initial conditions with initial energy E_{ini} distributed as $\exp(-E/1e4)$. Apart from mentioned, default parameters were used (cf. Appendix A).

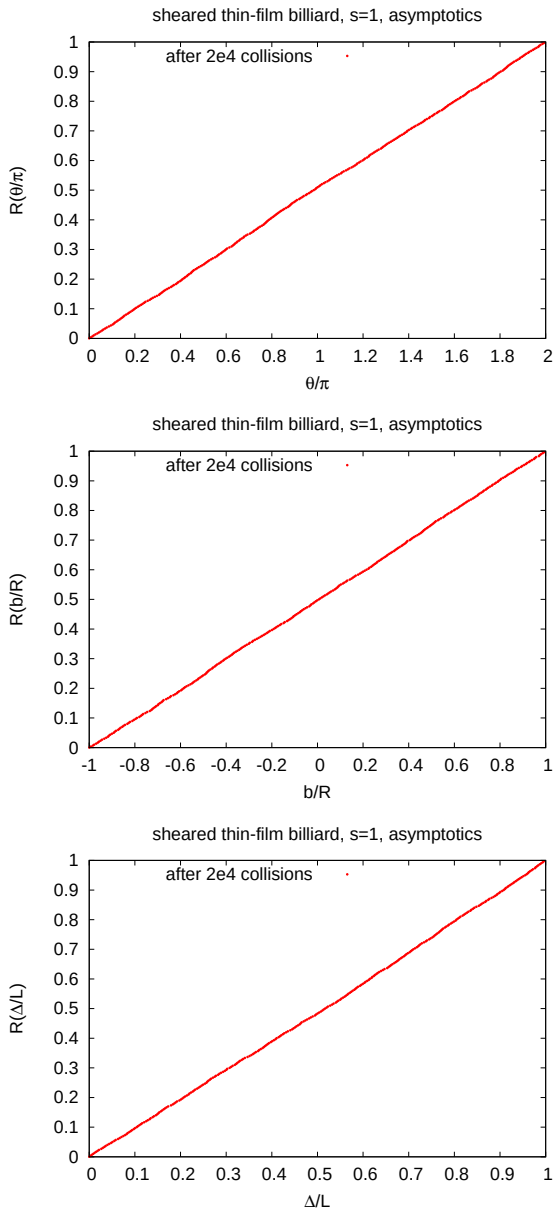

Figure B.6: **Cumulative distribution functions R of phase space projections on b-, θ- and Δ-coordinate for the sheared thin-film billiard with subcritical shear speed.** Asymptotically, an energy increase is observed for low shear speeds $s < s_c^0$ (Fig. 3.3) that could be caused by selection of special trajectories. The phase space data shown here and in Figs. B.7 and B.8 do, however, not support that scenario: Like the asymptotic energy distribution (Fig. 3.10), which is qualitatively the same for low and high shear speeds, the other 1-dimensional phase space projections do not differ: The projections onto the θ- (top), b- (middle) and Δ-coordinate (bottom) obtained from shearing with $s = 1$ result in uniform distributions like the one for $s = 2$ (Fig. B.3). **Simulation details.** Only the remaining non-clustered system out of $4 \cdot 10^4$ initial conditions with an initial energy E_{ini} distributed uniformly in $[7000, 1000]$ are considered. The distribution function is normalized to the number of remaining non-clustered systems. Apart from mentioned, default parameters were used (cf. Appendix A).

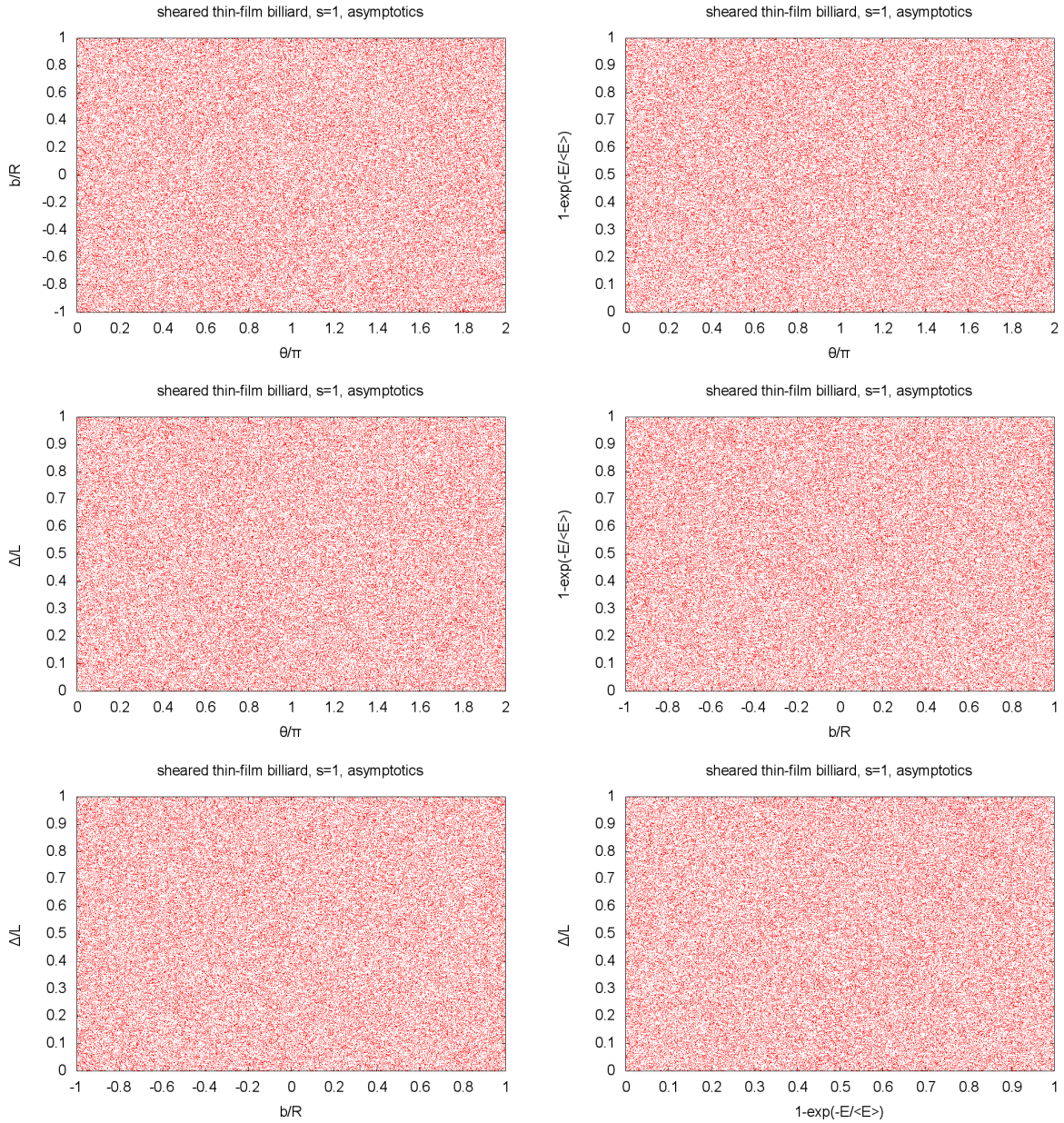

Figure B.7: **2-dimensional phase space projections for the sheared thin-film billiard with subcritical shear speed.** Shown are the six 2-dimensional projections of the 4-dimensional phase space in the scaling regime $n \gg 1$, $E \gg 1$. Assuming $E \sim \exp(-E/\langle E \rangle)$ (Fig. 3.10) the energy values have been transformed to yield a uniform distribution. As for $s = 2$ (Fig. B.4) the 2-dimensional projections show no structure. **Simulation details.** Only the remaining non-clustered system out of $4 \cdot 10^5$ initial conditions with an initial energies E_{ini} uniformly distributed in $[7000, 11000]$ are plotted after $n = 2 \cdot 10^4$ collisions. Apart from mentioned, default parameters were used (cf. Appendix A).

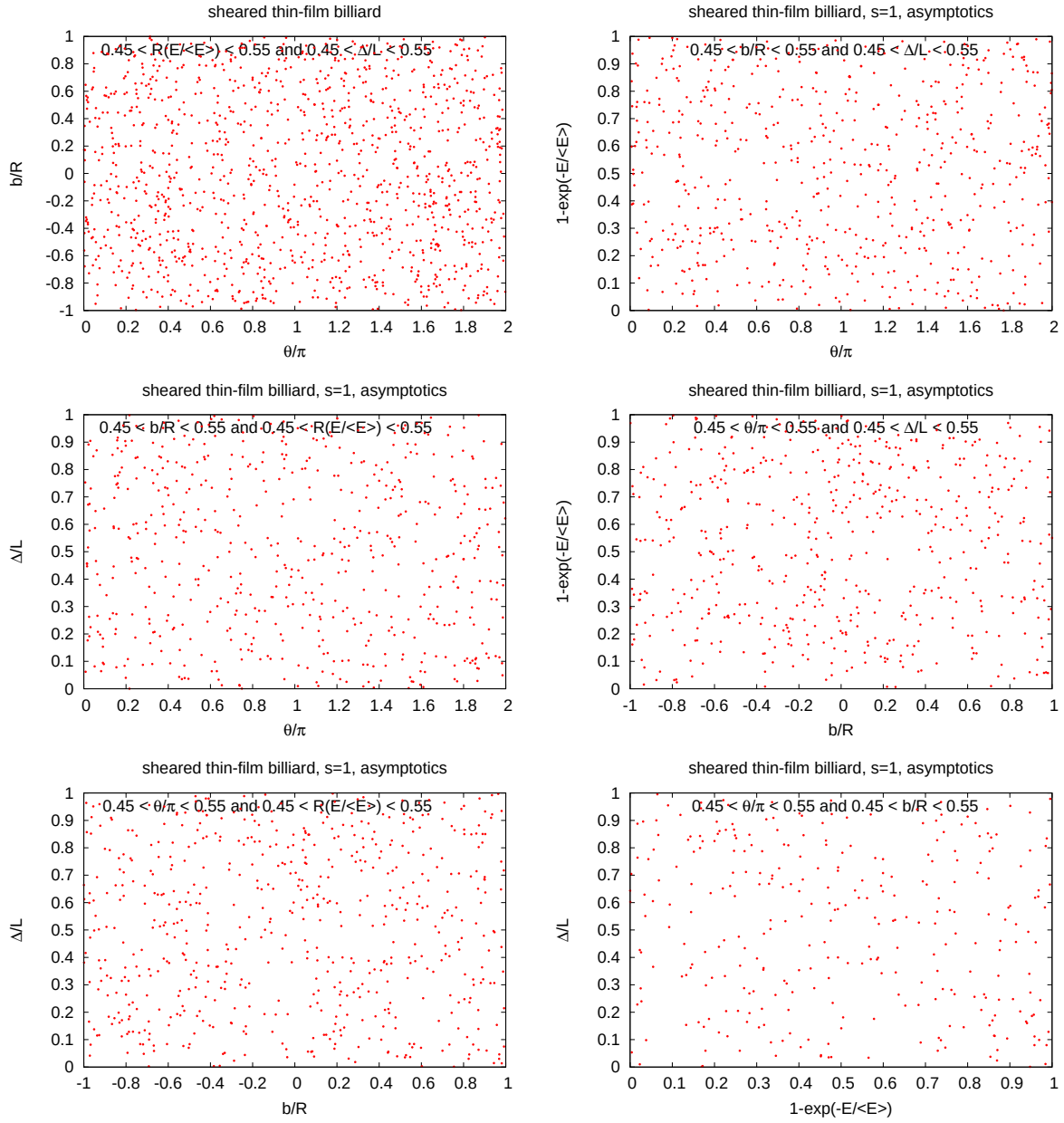

Figure B.8: 2**-dimensional phase space sections for the sheared thin-film billiard with subcritical shear speed.** To prevent averaging out of possible phase space structure by projection some phase space sections are shown. Together with the uniformity of the 1- and 2-dimensional projections (Fig. B.6 and B.7) they propose that the phase space of the sheared thin-film billiard remains not significantly structured also for subcritical shear speeds in the regime $n \gg 1$, $E \gg 1$. The somewhat unexpected increase of the average energy in this regime (Fig. 3.3) does therefore probably not stem from some remaining atypical systems. **Simulation details.** If found in the indicated phase space region the state of non-clustered systems is plotted after $n = 2 \cdot 10^4$ collisions. The number of dots may vary as the regions have different measures. $4 \cdot 10^5$ initial conditions with initial energy E_{ini} distributed uniformly in $[7000, 11000]$. Apart from mentioned, default parameters were used (cf. Appendix A).

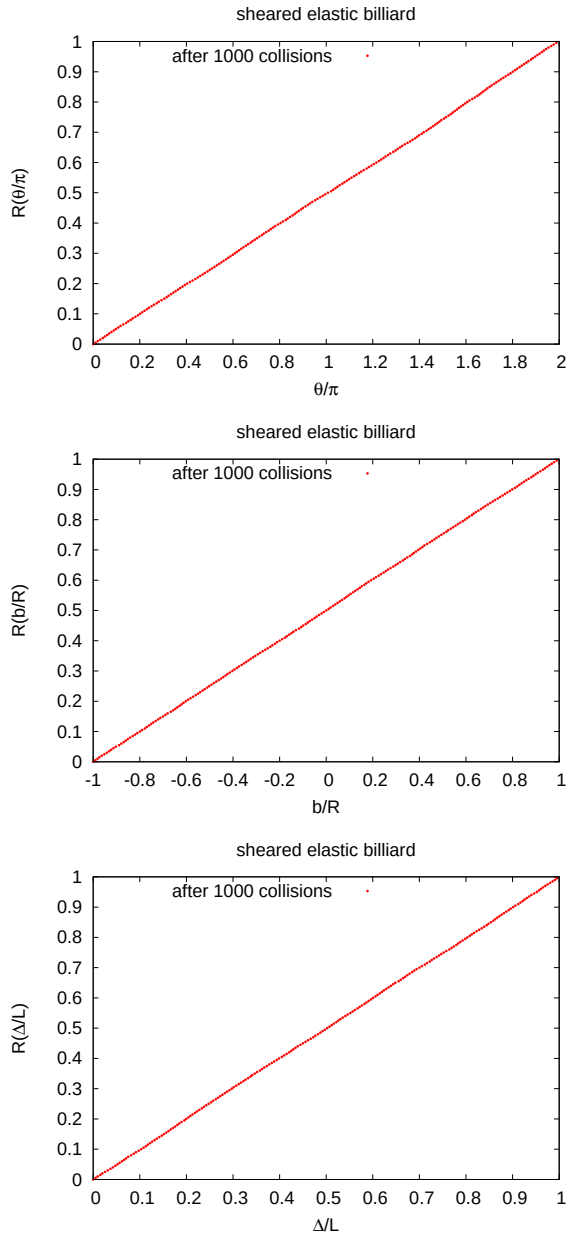

Figure B.9: **Cumulative distribution functions R of phase space projections on b-, θ- and Δ-coordinate for the elastic billiard.** While the phase space projection on the energy coordinate relaxes towards a roughly exponential distribution (Fig. 3.11) the projection onto the θ- (top left), b- (top right) and Δ-coordinate (bottom) result in uniform distributions. **Simulation details.** The cumulative distributions are normalized to the number of $2 \cdot 10^4$ initial conditions with initial energy E_{ini} distributed following $\exp(-E/10^4)$. Apart from mentioned, default parameters were used (cf. Appendix A).

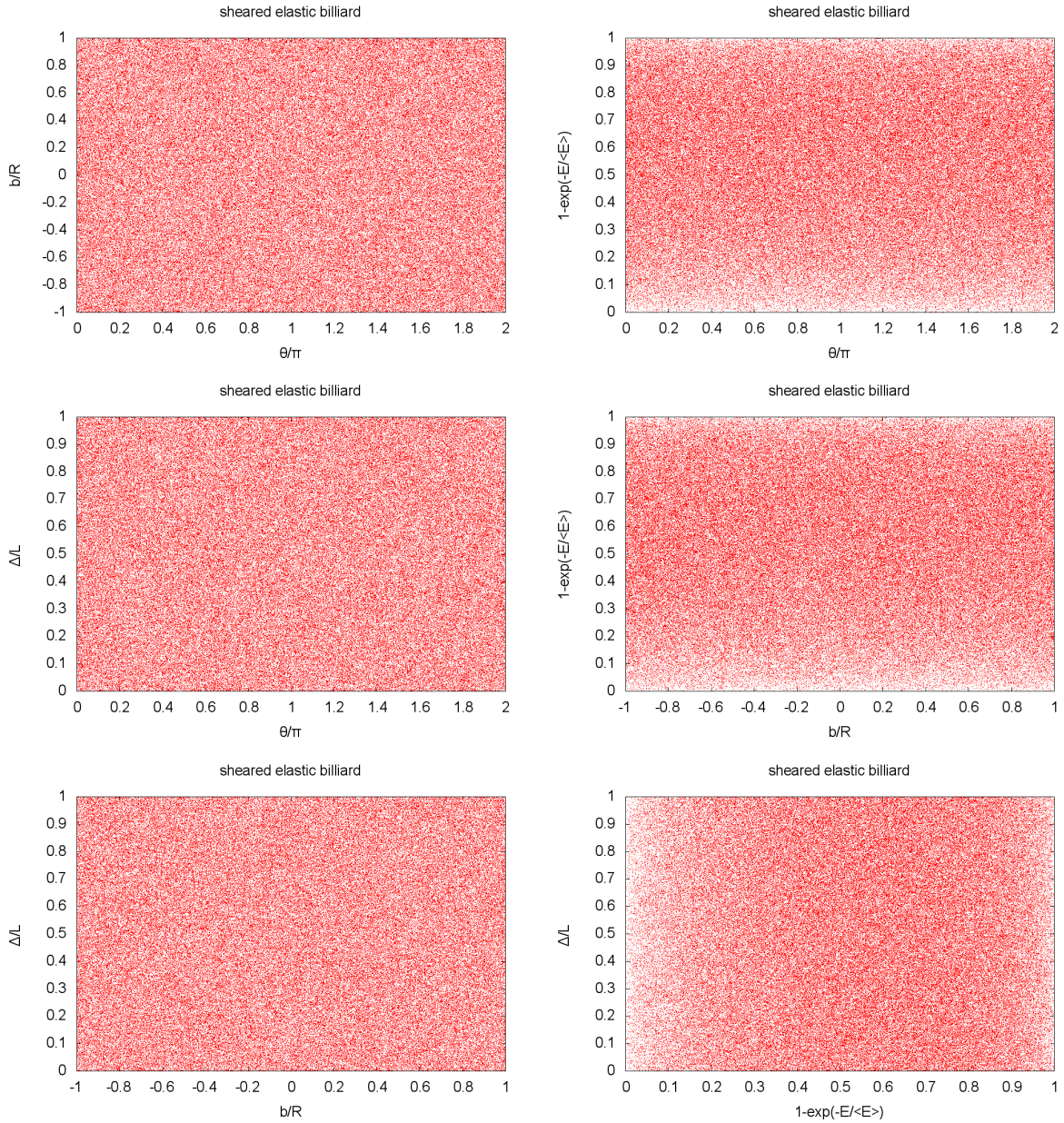

Figure B.10: **2-dimensional phase space projections for the elastic billiard.** Shown are the six 2-dimensional projections of the 4-dimensional phase space in the asymptotic scaling regime $n \gg 1$, $E \gg 1$. The energy values have been transformed like in the wet case. Due to the deviations from the exponential distribution (Figs. 3.11 and 3.12) there are deviations from uniformity. Apart from this the 2-dimensional projections show no structure. **Simulation details.** $n = 10^5$ collisions. $2 \cdot 10^5$ initial conditions with initial energy E_{ini} distributed as $\exp\left(-E/10^4\right)$. Apart from mentioned, default parameters were used (cf. Appendix A).

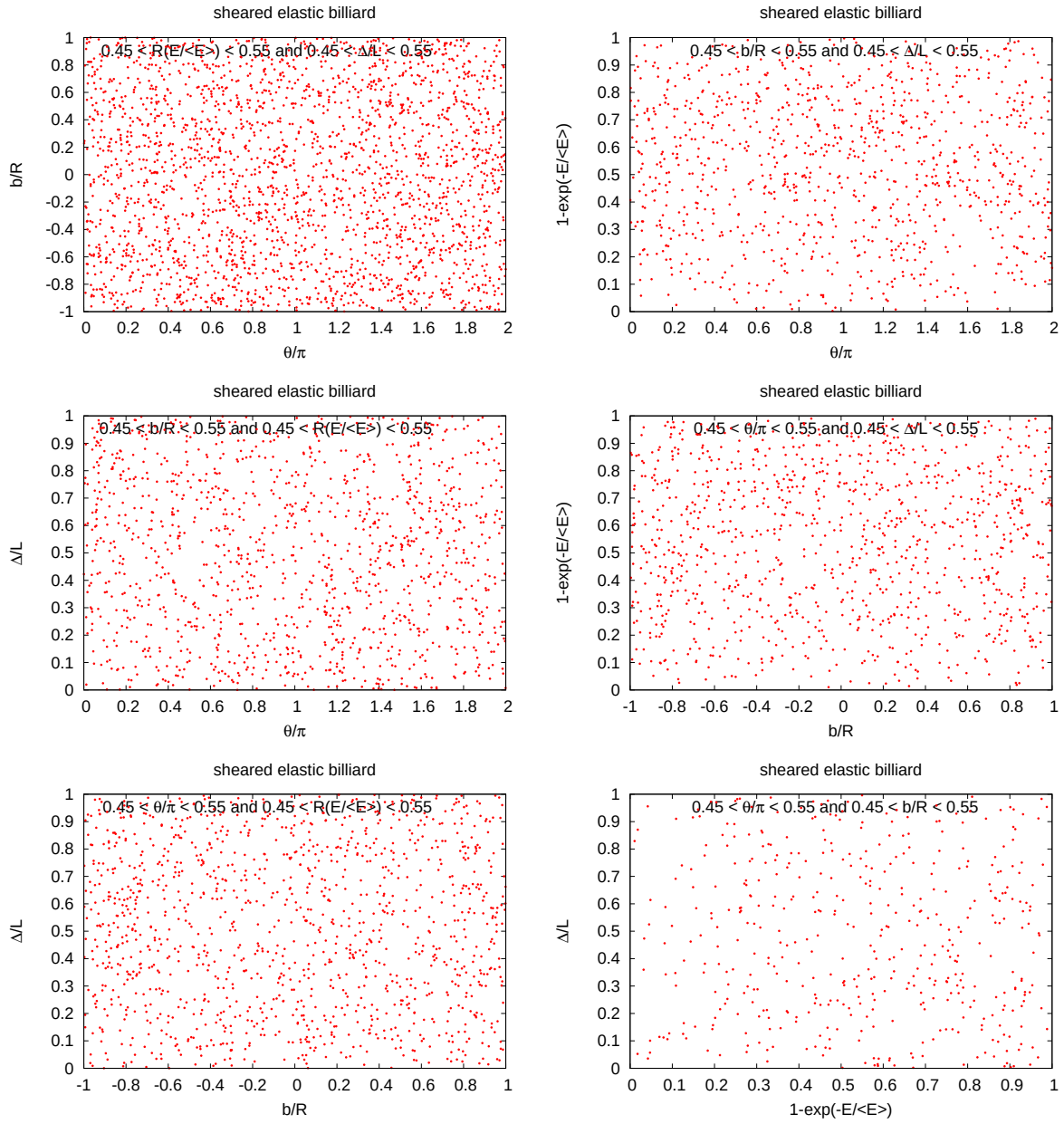

Figure B.11: **2-dimensional phase space sections for the elastic billiard.** To prevent averaging out of possible phase space structure by projection some phase space sections are shown. Together with the uniformity of 1- and 2-dimensional projections (Figs. B.9 and B.10) they propose that the phase space of the sheared elastic billiard system is not significantly structured in the asymptotic scaling regime $n \gg 1$, $E \gg 1$. **Simulation details.** If found in the indicated phase space region after $n = 10^5$ collisions the state of a system is plotted. The number of dots may vary as the regions have different measures. $2 \cdot 10^5$ initial conditions with initial energy E_{ini} distributed as $\exp(-E/10^4)$. Apart from mentioned, default parameters were used (cf. Appendix A).

B.3 Correlations

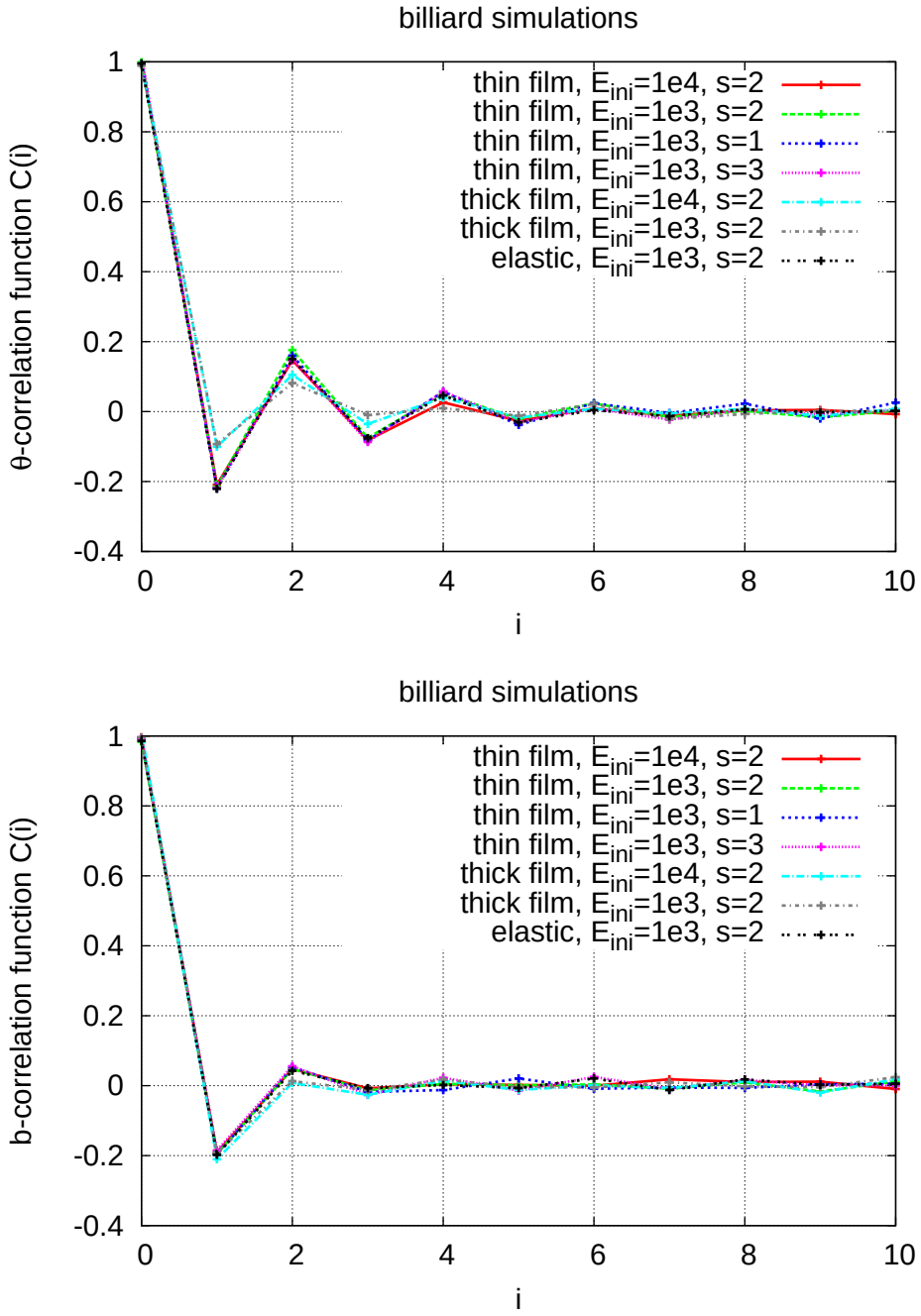

Figure B.12: For caption and continuation of the figure see next page.

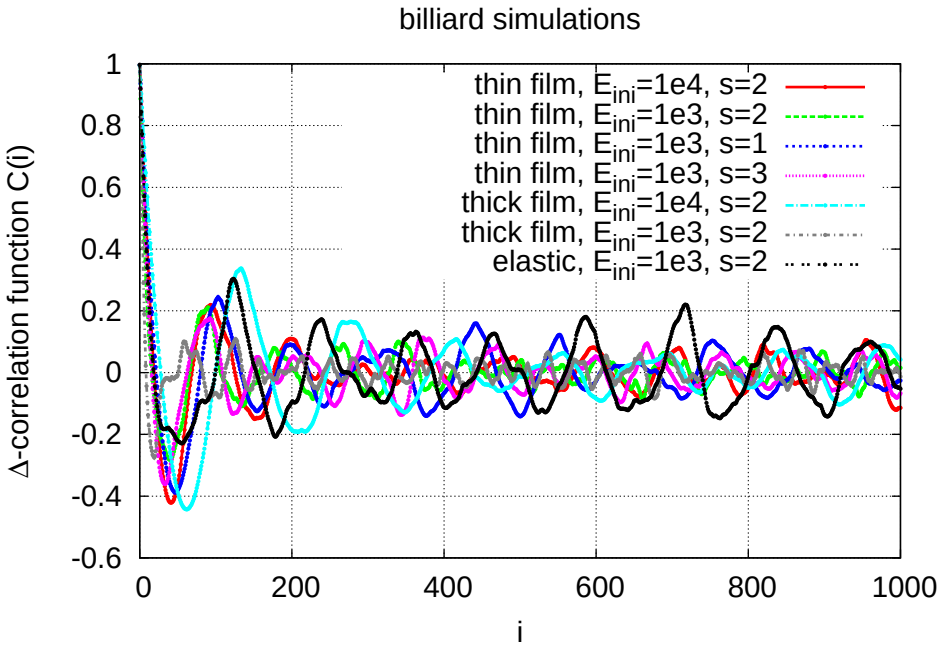

Figure B.13: **Correlation functions C for sheared billiard simulations.** The figures show the correlation function $C(i) = \frac{1}{(n-i)\sigma^2}\sum_{k=1}^{n-1}(X_k - < X >)(X_{k+i} - < X >)$ where σ^2 is the variance for $X = \theta, b, \Delta$. The correlation function is qualitatively the same for the wet billiards and the elastic billiard. The spatial coordinates θ and b decorrelate rapidly as is to be expected from the chaoticity of the billiard dynamics. Note that the slight anti-correlation is reasonable as a collision following a Lees-Edwards boundary crossing is likely to "mirror". The phase Δ shows periodic correlations that are due to the periodicity of the sheared lattice. The correlation period $\Delta n_c \approx 100$ gives an estimate of the mean free path f: The phase Δ returns with a temporal period $\Delta T = L/s$ where L is the box size and s the shear speed. Within ΔT a particle with speed v travels a distance $\Delta x = v\Delta T$. The mean free path f connects Δx to the correlation period: $\Delta n_c = \frac{\Delta x}{f} = \frac{vL}{sf}$. With $L = 3$ and $s = 2$ this yields $f = 1.5$. As the minimum distance between two scatterers is 1 for $L = 3$ this result seems plausible. **Simulation details.** $\{X_i\}$ was obtained by following a random initial condition for $n_{\max} = 10^4$ collisions. Apart from mentioned, default parameters were used (cf. Appendix A).

B.4 Collisions vs. Lees-Edwards boundary crossings

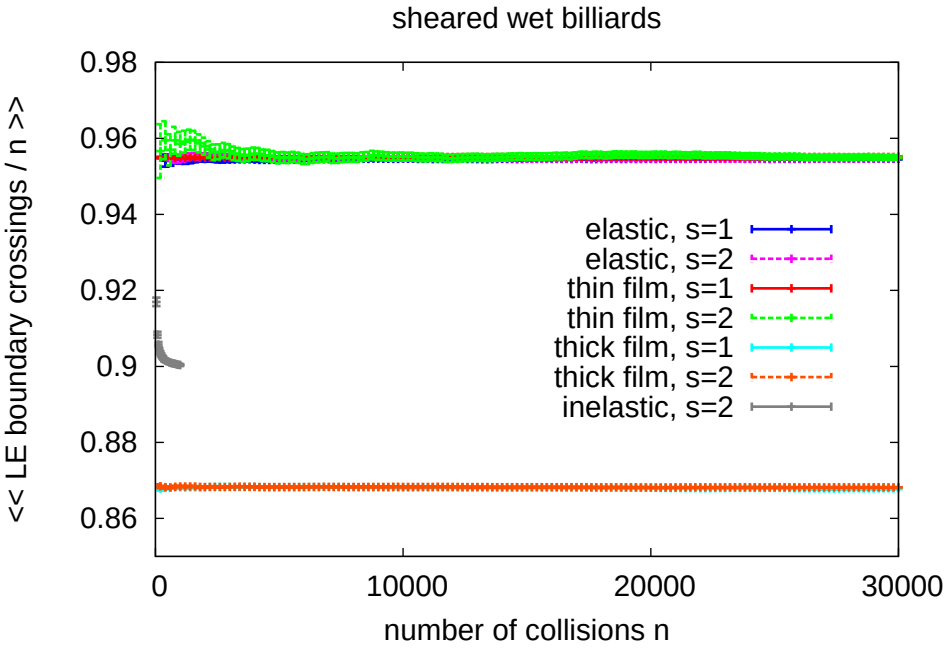

Figure B.14: **Number of Lees-Edwards boundary crossings per collision in the billiard simulations.** On average, crossing a Lees-Edwards boundary increases the system energy (Eq. 1.6) while a collision decreases it (Eq. 2.6, except for the elastic case). To estimate the energy change on the level of averages it is therefore interesting to know the number of Lees-Edwards boundary crossing per collision, ν. The figure shows the ensemble and time averaged value $\langle\langle\nu\rangle\rangle$ for the two wet, the elastic and the inelastic sheared billiard. The values of the thin-film and the elastic billiard coincide while the thick-film billiard experiences more collisions relative to the number of boundary crossings. This is to be expected as for the thick-film billiard "number of collisions" in fact refers to number of boundary crossings, which will be larger than the actual number of collisions (Sec. 2.5). For the sheared billiard with inelastic collisions and no bridge a value in between is observed. Furthermore, ν seems to be independent of the shear speed s. The fact that no change in ν is observed between the initial and the asymptotic regime for $s = 1$ is another indicator (see also Figs. B.7 to B.8) that the asymptotic increase of energy is not caused by atypical trajectories. The ratio ν will depend, however, on the billiard geometry, i.e. the length of the periodic box L relative to the scatterer radius R, which also determines the density. Throughout Chapter 3 the geometric parameters $R = 1$ and $L = 3$ have not been varied. As shear speeds show the same ν within the error bars the different slopes in Fig. 3.3 do not stem from differing ν. **Simulation details.** Considered are remaining non-clustered systems. The error bars are $\pm 1/\sqrt{n \cdot N(n)}$ where $N(n)$ is the number of remaining systems. The thin-film and elastic billiard were initialized with E_{ini} uniformly distributed in $[7000, 11000]$, the thick-film billiard was isoenergetically initialized with $E_{\text{ini}} = 10^4$. For the inelastic billiard only data with $n_{\max} = 1000$ was available. As ν does not depend on s and as ν does not change with $n \propto E$ the initial energy should be unimportant. Apart from mentioned, default parameters were used (cf. Appendix A).

B.5 Vibrated elastic Sinai billiard

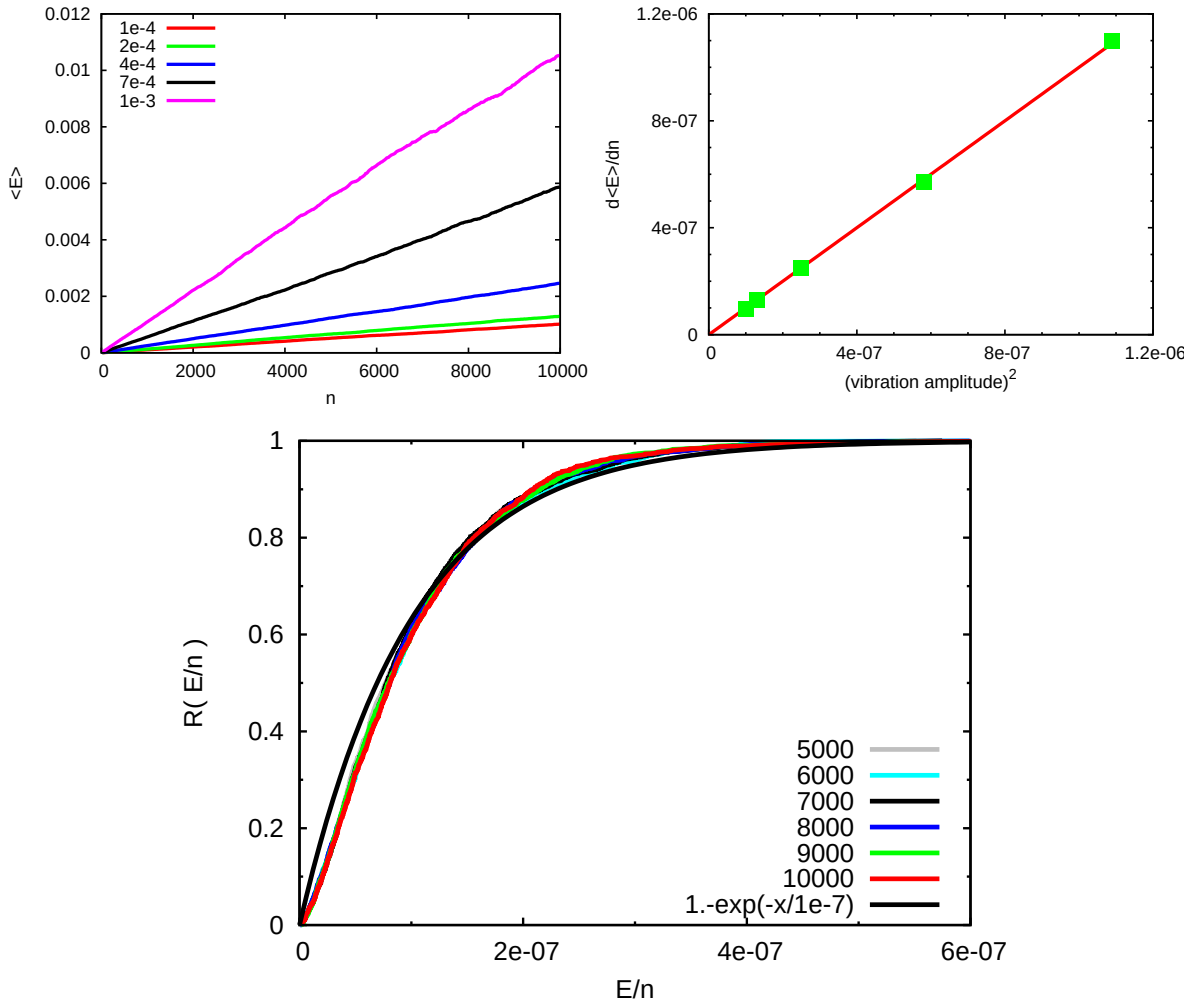

Figure B.15: **Energy dynamics in the vibrated Sinai billiard with elastic collision.** A Sinai billiard or Lorentz gas with scatterers that are vibrating, i.e. periodically moving about their resting position, shows an energy dynamics that closely resembles that of the sheared (elastic) billiard discussed in Sec. 3.2. The top-row plots compare to Fig. 3.5 where the shear speed s is replaced by the vibration amplitude. The bottom plot resembles Fig. 3.11 (bottom). Note the linear axes as well as the slightly different scaling variable $E/n \propto E/\langle E \rangle$.
The plots are used by courtesy of Jürgen Vollmer and Diego F. M. Oliveira. They have been presented as part of a poster contribution (Franziska Glaßmeier, Jürgen Vollmer, Diego F. M. Oliveira: "A billiard model for wet granular matter: Acceleration, lifetimes, and transients") to the workshop "Exploring complex dynamics in high-dimensional chaotic systems: From weather forecasting to oceanic flows", which was held at the Max-Planck-Institute for the Physics of Complex Systems, Dresden, in January 2010.

Bibliography

[AT87] M. P. Allen and D. J. Tildesley, *Computer simulations of liquids*, Oxford, 1987.

[AT09] Eduardo G. Altmann and Tamás Tél, *Poincaré recurrences and transient chaos in systems with leaks*, Phys. Rev. E **79** (2009), no. 016204.

[Bri09] Martin Brinkmann, *Notes on wet disks sheared with Lees edwards boundary conditions*, Internal report Max-Planck-Institute for Dynamics and Self-Organization, Dept. of Complex Fluids, May 2009.

[Bun00] L. A. Bunimovich, *Existence of transport coefficients*, Hard Ball Systems and the Lorentz Gas (D. Szász, ed.), Springer, 2000.

[Bun07] L. Bunimovich, *Dynamical billiards*, Scholarpedia **2** (2007), no. 8, 1813.

[CPY90] G. F. Carnevale, Y. Pomeau, and W. R. Young, *Statistics of ballistic agglomeration*, Phys. Rev. Lett. (1990).

[CTH93] Arati Chokshi, A. G. G. M. Tielens, and D. Hollenbach, *Dust coagulation*, Astrophys. J. **407** (1993), 806–819.

[Dor99] J. R. Dorfman, *An introduction to chaos in nonequilibrium statistical mechanics*, Cambridge, 1999.

[DT97] C. Dominik and A. G. G. M. Tielens, *The physics of dust coagulation and the structure of dust aggregates in space*, Astrophys. J. **480** (1997), 647–673.

[Eck85] J.-P. Eckmann, *Ergodic theory of chaos and strange attractors*, Rev. Mod. Phys. (1985).

[Ein05] A. Einstein, *Über die von der molekularkinetischen Theorie der Wärme geforderte Bewegung von in ruhenden Flüssigkeiten suspendierten Teilchen*, Einsteins Annus mirabilis - Fünf Schriften, die die Welt der Physik revolutionierten (John Stachel, ed.), Rowohlt Taschenbuch Verlag, 2nd ed., 2005.

[FHZ07] A. Fingerle, S. Herminghaus, and V. Yu. Zaburdaev, *Chaoticity of the wet granular gas*, Phys. Rev. E (2007).

[FRHH08] A. Fingerle, K. Roeller, K. Huang, and S. Herminghaus, *Phase transitions far from equilibrium in wet granular matter*, New J. Phys. **10** (2008), no. 053020.

[Gar85] C. W. Gardiner, *Handbook of stochastic methods for physics, chemistry and the natural sciences*, 2nd ed., Springer, 1985.

[Her05] S. Herminghaus, *Dynamics of wet granular matter*, Adv. Phys. **54** (2005), no. 221.

[HF07] Axel Hager-Fingerle, *Entropy production and phase transitions far from equilibrium with emphasis on wet granular matter*, Doktorarbeit, Georg-August-Universität zu Göttingen, 2007.

[Iij87] S. Iijima, *Fine particles of silicon. I. Crystal growth of spherical particles of Si*, Jpn. J. Appl. Phys. **26** (1987).

[KD00] R. Klages and Christoph Dellago, *Density-dependent diffusion in the periodic Lorentz gas*, J. Stat. Phys. **101** (2000), no. 1/2.

[Liv00] C. Liverani, *Interacting particles*, Hard Ball Systems and the Lorentz Gas (D. Szász, ed.), Springer, 2000.

[Los07] A. Loskutov, *Dynamical chaos: systems of classical mechanics*, Physics - Uspekhi **50** (2007), no. 9, 939–964.

[LP73] Joel L. Lebowitz and Oliver Penrose, *Modern ergodic theory*, Physics Today (1973).

[LRA99] A. Yu. Loskutov, A. B. Ryabov, and L. G. Akinshin, *Mechanism of Fermi acceleration in dispersing billiards with time-dependent boundaries*, J. Exp. Theo. Phys. **89** (1999), no. 5.

[LRBvdM04] Detlef Lohse, Remco Rauhé, Raymond Bergmann, and Devaraj van der Meer, *Creating a dry variety of quicksand*, Nature **432** (2004).

[Mac03] Michael C. Mackey, *Time's arrow – the origins of thermodynamic behavior*, Dover, 2003.

[MIMA08] C. C. Maaß, N. Isert, G. Maret, and C. M. Aegerter, *Experimental investigation of the freely cooling granular gas*, Phys. Rev. Lett. **100** (2008), no. 248001.

[MTV04] László Mátyás, Tamás Tél, and Jürgen Vollmer, *Coarse-grained entropy and information dimension of dynamical systems: The driven Lorentz gas*, Phys. Rev. E (2004).

[OA05] National Oceanic and Atmospheric Administration, `http://en.wikipedia.org/wiki/File:Granizo.jpg` (last checked: Jul 10, 2010), 2005.

[Ott02] Edward Ott, *Chaos in dynamical systems*, 2nd ed., Cambridge, 2002.

[PB04] Thorsten Pöschel and Nikolai V. Brilliantov, *Kinetic theory of granular gases*, Oxford, 2004.

[PBS03] Thorsten Pöschel, Nikolai V. Brilliantov, and Thomas Schwager, *Violation of molecular chaos in dissipative gases*, Int. J. Mod. Phys. C (2003).

[PIM94] Janka Petravic, Dennis J. Isbister, and Gary P. Morris, *Correlation dimension of the sheared hard-disk Lorentz gas*, J. Stat. Phys. **76** (1994).

[PK97] Hans R. Pruppacher and James D. Klett, *Microphysics of clouds and precipitation*, 2nd ed., Kluwer Academic Publishers, 1997.

[Rah09] S. H. Ebrahimnazhad Rahbari, *Lees-edwards boundary conditions*, Internal report Max-Planck-Institute for Dynamics and Self-Organization, Dept. of Complex Fluids, Nov 2009.

[Rei98] L. Reichl, *A modern course in statistical physics*, John Wiley, 1998.

[Ris89] H. Risken, *The fokker-planck equation*, Springer, 1989.

[Röl10] Klaus Walter Röller, *Numerical simulations of wet granular matter*, Doktorarbeit, Universität Göttingen, 2010.

[RVH09] Klaus Roeller, Jürgen Vollmer, and Stephan Herminghaus, *Unstable Kolmogorov flow in granular matter*, Chaos **19** (2009), no. 4, 041106.

[Sch06] Franz Schwabl, *Statistische Mechanik*, 3rd ed., Springer, 2006.

[Sch09] Mario Scheel, *Experimental investigations of the mechanical properties of wet granular matter*, Doktorarbeit, Universität Göttingen, 2009.

[Set07] James P. Sethna, *Entropy, order parameters, and complexity*, Oxford, 2007.

[Sim10] Nandor Simányi, *The Boltzmann-Sinai ergodic hypothesis in full generality*, `arxiv:1007.1206` [math.DS], Jul 2010.

[SUK+06] Matthias Schröter, Stephan Ulrich, Jennifer Kreft, Jack B. Swift, and Harry L. Swinney, *Mechanisms in the size segregation of a binary granular mixture*, Phys. Rev. E **74** (2006), no. 011307.

[Szá00] D. Szász (ed.), *Hard ball systems and the Lorentz gas*, Springer, 2000.

[Tab05] Serge Tabachnikov, *Geometry and billiards*, AMS, 2005.

[Tay96] Michael E. Taylor, *Partial Differential Equations I: Basic Theory*, Springer, 1996.

[TG06] Tamás Tél and Márton Gruiz, *Chaotic dynamics - an introduction based on classical mechanics*, Cambridge, 2006.

[TL08] Tamás Tél and Ying-Cheng Lai, *Chaotic transients in spatially extended systems*, Physics Reports **460** (2008), 245–275.

[UAR+09] Stephan Ulrich, Timo Aspelmeier, Klaus Roeller, Axel Fingerle, Stephan Herminghaus, and Annette Zippelius, *Cooling and aggregation in wet granulates*, Phys. Rev. Lett. (2009).

[UAZ+09] Stephan Ulrich, Timo Aspelmeier, Annette Zippelius, Klaus Roeller, Axel Fingerle, and Stephan Herminghaus, *Dilute wet granular particles: Nonequilibrium dynamics and structure formation*, Phys. Rev. E **80** (2009), no. 031306.

[UKAZ09] H. Uecker, W. T. Kranz, T. Aspelmeier, and A. Zippelius, *Partitioning of energy in highly polydisperse granular gases*, Phys. Rev. E **80** (2009), no. 4, 041303.

[US07] Stephan Ulrich and Matthias Schröter, *Der Paranuss-Effekt*, Physik in unserer Zeit **38** (2007), no. 6.

[vK61] N. G. van Kampen, *Fundamental problems in statistical mechanics of irreversible processes*, Fundamental Problems in Statistical Physics (E. G. D. Cohen, ed.), NUFFIC International Summer Course in Sciences, 1961.

[Vol02] Jürgen Vollmer, *Chaos, spatial extension, tranport, and non-equilibrium thermodynamics*, Physics Reports **372** (2002), 131–267.

[WAJS00] Christopher D. Willett, Michael J. Adams, Simon A. Johnson, and Jonathan P. K. Seville, *Capillary bridges between two spherical bodies*, Langmuir **16** (2000), 9396–9405.